Influence of Solutes on the Planar Faults in Ni-based Superalloys: A First-principles Study

A Thesis
Submitted for the Degree of
Doctor of Philosophy

by
KAUSHLENDRA KUMAR

Theoretical Sciences Unit
Jawaharlal Nehru Centre for Advanced Scientific Research
Bangalore - 560 064

September 2018

Dedicated to

My family

DECLARATION

I hereby declare that the matter embodied in the thesis entitled **“Influence of Solutes on the Planar Faults in Ni-based Superalloys: A First-principles Study”** is the result of investigations carried out by me at the Theoretical Sciences Unit, Jawaharlal Nehru Centre for Advanced Scientific Research, Bangalore and Defence Metallurgical Research Laboratory, Hyderabad, India under the supervisions of Prof. Umesh V. Waghmare and Dr. R Sankarasubramanian and that it has not been submitted elsewhere for the award of any degree or diploma.

In keeping with the general practice in reporting scientific observations, due acknowledgement has been made whenever the work described is based on the findings of other investigators.

……………………………………………..

KAUSHLENDRA KUMAR

CERTIFICATION

I hereby certify that the matter embodied in this thesis **“Influence of Solutes on the Planar Faults in Ni-based Superalloys: A First-principles Study”** has been carried out by Kaushlendra Kumar at the Theoretical Sciences Unit, Jawaharlal Nehru Centre for Advanced Scientific Research, Bangalore, and Defence Metallurgical Research Laboratory, Hyderabad, India under our supervision and that it has not been submitted elsewhere for the award of any degree or diploma.

....	....
Dr. R Sankarasubramanian	Prof. Umesh V. Waghmare
(DMRL)	(JNCASR)

Acknowledgements

I take this opportunity to extend my sincere gratitude to my research supervisors Prof. U. V. Waghmare and Dr. R. Sankarasubramanian. They, apart from providing valuable guidance, gave me constant encouragement and reassurance because of which I could successfully complete this work.

I am highly indebted to the Prof. C.N.R. Rao, Linus Pauling research professor and honorary president JNCASR, and, DG DRDO for initiating a collaborative project between JNCASR and DRDO on *Advanced Materials Research* under *Grants-in-aid,* because of which I got the opportunity to work described in this thesis.

I express my gratitude to Dr. G Malakondiah and Dr. Amol Gokhale, Former Directors, DMRL, Dr. S. V. Kamat, Former Director, DMRL and presently DG DRDO (NSM) and Dr. Vikas Kumar, Director, DMRL for selecting and permitting me to enrol for this work at JNCASR.

I am grateful to Prof. Shobhana Narasimhan, Prof. Alok Nath, Prof. Ranjan Datta and Prof. S. Balasubramanian who offered excellent courses at JNCASR which helped me to lay a solid foundation to carry out my research activity.

I am also grateful to the colleagues at the Prof. Waghmare’s group at JNCASR for their assistance in understanding the DFT codes as well as its execution. I greatly acknowledge the support from my colleagues Kumar Saurabh and R. Ramakrishnan from DMRL for numerous technical discussions and their help in proof reading the thesis.

I acknowledge Shri Anupam Mandal and Shri Mahesh, Scientists at ANURAG and Director, ANURAG for providing the computational facility without which it would have been practically impossible to complete the work.

My final, and most heartfelt, acknowledgement for the unconditional love, support and blessings of my parents, my sisters and my kids for their constant inspiration to work towards achieving this degree.

Synopsis

The primary cause for excellent high-temperature mechanical properties exhibited by Ni-based superalloys is essentially the high volume fraction of ordered and coherent Ni_3Al-based precipitates in the Ni-rich solid solution matrix. While the lattice parameters of the precipitate and of the matrix structures influence the coherency strains and hence the extent of precipitation hardening, the stacking fault energies (SFE) influence the dislocation motion and hence the strength. Plastic deformation of crystalline materials depends greatly on mobility of dislocations. The glide of dislocations requires relatively little atomic motion compared to full shifting of the entire atomic planes in perfect (i.e. defect free) crystals. The generalized stacking fault (GSF) energy surface was proposed to describe the cost energy associated with fractional shifting of glide planes, and can be accurately computed from first-principles based Density Functional Theory (DFT) calculations. This thesis is aimed at estimating the energies of various stacking faults that exist in Ni and Ni_3Al, and the changes associated in their energies on alloying with solutes from the 3d, 4d and 5d series transition metals (TM). An attempt is made to understand the dislocation movement in terms of Peierls stress by estimating the unstable stacking fault energy within the framework of first-principles.

The thesis is divided into seven chapters. The first chapter provides a brief introduction to Ni-based superalloys, along with a brief overview of various atomistic simulation techniques highlighting their advantages and limitations. The second chapter describes basic theoretical aspects of first-principles calculations based on DFT, used throughout the present work.

Chapter 3 is aimed to elucidate the effect of changes in atomic volume of Ni i.e. the lattice parameter (a_o), associated with substitution of solutes for Ni. For each of the TM series, we find that the atomic volume of Ni exhibits a minimum for substitutional elements with half-filled d-orbitals (5 d orbital valence electrons). The change in a_o with solute substitution in Ni is observed to follow the Vegard's law (an approximate empirical rule for the lattice parameter of an alloy as a function of its constituent elements), and our estimates of Vegard's coefficients are in reasonable agreement with the other reported values. Another important aspect that influences the mechanical behavior of an alloy is the preferences of the solute atoms to segregate in clusters or tend to remain far apart as in solid solution. This behavior has been analyzed by calculating the binding energy (BE) as a function of distance between the substituted solute atoms. It is shown that the magnetic state of nickel, apart from individual solutes chemical activity, does influence the tendency of clustering. Cr, Co, Re and Ru exhibit the tendency towards clustering when Ni is considered magnetic. However, above the Curie temperature, (nickel treated as non-magnetic in our calculation), only Co favors clustering.

In chapter 4, we describe computational details of the scheme for estimating the intrinsic stacking fault energy (ISFE, γ_{is}) and unstable stacking fault energy (USFE, γ_{us}) of Ni and its solid solutions. The results have been analyzed in terms of variations in γ_{is} and γ_{us} as functions of number of d-valence electrons, considering both magnetic and non-magnetic states. All solute (except Pd) substitution reduce the γ_{is} irrespective of the magnetic state of nickel. However, 20 - 30 % higher estimates of γ_{is} are obtained when nickel is treated as a magnetic material. The results have also been obtained with variable spacing between two solute atoms, and its effects on the γ_{is} and γ_{us} are analyzed. It is observed that some of the solutes, such as Zr, Nb, Mo, Ru, W and Re, do result in changes in γ_{us} as function of the distance between solute atoms. A correlation between the changes in volume and in γ_{us} with substitutional alloying has been established.

The fifth chapter provides a detailed description of effects of solute substitution on the energies of anti-phase boundary (APB), superlattice intrinsic stacking fault (SISF) and unstable stacking fault (USF) of Ni_3Al. Since it is an ordered intermetallic compound, effects of solute substitution at Al or Ni or simultaneously at both Al and Ni sites have been considered separately. It has been shown that USF and APB energies are maximal for the systems wherein solutes having half-filled d-orbitals are substituted at the Al site. We establish a correlation between SISF and APB energies.

The sixth chapter is focused on the cleavage energy and its relevance to the fracture strength in terms of Griffith's work (G_c), related to mode I cleavage fracture of Ni system alloyed around 1 at.% of solutes. G_c is defined as the work needed to cleave a crystal across a particular crystallographic plane. Tendency of a micro void formation and its growth can also be assessed in terms of "cleavage energy". Here, we focus on the (111) plane of FCC Ni. Except Zr and Pd of 5d series, all the substitutional elements considered here are found to increase the G_c. Analysis of the solute effects on the intrinsic ductility has been done by evaluating a dimensionless ductility parameter (D) as $D=0.15G_c/\gamma_{us}$, where G_c is the Griffith work or energy needed to create two new surfaces ($G_c = 2\gamma_s$, where γ_s is the surface energy) and γ_{us} is USFE. The ductility parameter calculated for non-magnetic Ni with or without any solute is typically around 20 % higher compared to its magnetic counterpart. In general, the solute substitution is observed to weakly influence the ductility of Ni. This inferences have further been strengthened based on B/G ratio and using the Pugh criterion.

The last chapter summarizes the findings of the work in the thesis, and provides future perspectives. It is envisaged that the comprehensive data generated through this work would form useful input to multiscale modeling and simulations. For example, the fault energies can serve as proto-data for the construction of Γ-surfaces, which can be input into discrete dislocation dynamics and/or phase field dislocation dynamics simulations to establish structure-property correlations. Secondly, occupancy of the d-shell of substituents and its correlations with APBE & SISFE should facilitate identification of descriptors relevant to simple predictive models of fault energies. Such efforts would be critical not only to understand the deformation mechanisms in model alloys but also in rational design of Ni-based alloys with improved mechanical properties.

List of Publications

1. Kaushlendra Kumar, R. Sankarasubramanian, Umesh V. Waghmare, “The effect of γ-γ' interface on the tensile and shear strengths of nickel-based superalloys: A first-principles study”, *Comput. Mat. Sci. 97 (2015) 26–31*.
2. Kaushlendra Kumar, R. Sankarasubramanian, Umesh V. Waghmare, “Influence of dilute solute substitutions in Ni on its generalized stacking fault energies and ductility”, *Comput. Mat. Sci. 150 (2018) 424–431*.
3. Kaushlendra Kumar, R. Sankarasubramanian, Umesh V. Waghmare, “Tuning planar fault energies of Ni_3Al with substitutional alloying: First-principles description for guiding rational alloy design”, *Scripta Mater. 142 (2018) 74–78*.

List of Figures

List of Tables

List of Abbreviations / Notations

APB - Antiphase boundary

BE - Binding energy

CSF - Complex stacking fault

δ - Stress-free lattice misfit

DD - Dislocation Dynamics

DFT - Density functional theory

$E_{P\text{-}N}$ - Peierls and Nabarro energy

$E_{xc}[n]$ - Exchange-correlation functional

FEM - Finite Element Method

G_c - Griffith work of rupture or cleavage energy

GGA - Generalized Gradient Approximation

γ_{is} - Intrinsic stacking fault energy of Ni

GSF - Generalized stacking fault energy surface

γ_{us} - Unstable stacking fault energy

LDA - Local Density Approximation

MD - Molecular Dynamics

NBSX - Ni-based single crystal superalloys

N_f - Fermi energy

NN - Nearest neighbour

PDOS - Partial density of states

SISF - Superlattice intrinsic stacking fault

SISFE - Superlattice instrinsic stacking fault energy

SX - Single crystalline

TET - Turbine entry temperature

TM - Transition metals

USF - Unstable stacking faults

USFE - Unstable stacking fault energy

τ_{P-N} - Peierls and Nabarro stress

Table of Contents

Chapter 1

Introduction

Materials exhibit a wide variety of properties in broadly varying magnitudes, and hence different materials find different applications depending on their suitability. These properties can be categorized as mechanical, electrical, thermal, magnetic and physical. For example, mechanical properties of materials are of crucial importance in various applications where materials are subjected to forces and stresses. The ability to bear these forces and stresses without undergoing a permanent deformation decreases with increasing temperature for most of the alloys. This strength, known as the yield strength, however increases (or at least does not decrease) as a function of temperature for a certain class of materials. Ni-based superalloys belong to such a class of materials characterized with superior high-temperature mechanical strength, in addition to corrosion and creep resistance in harsh environments. Due to the combination of these properties, they are the preferred materials for the hot sections such as turbine blades and turbine discs of gas turbine engines used in the aerospace and power generation industries.

1.1 Ni-based superalloys

Metallic alloys that can be used in structural applications at temperatures in excess of 0.7 times of the absolute melting temperature are termed as superalloys. The behavior exhibited by this class of alloys is contrary to normal alloys in that the strength increases with increasing temperature reaching a peak and thereafter it decreases. Another characteristic of these alloys is their ability to resist mechanical degradation over extended period of time even at very high operating temperature. The term superalloy was used after the Second World War to describe a group of alloys that found applications in aircraft engines because of their excellent performance at elevated temperatures. The range of applications also includes land-based gas turbines, rocket engines etc. The three major classes of superalloys are nickel-, iron-, and cobalt- based alloys. In this thesis, we have focused on Ni-based superalloys, which are used for making turbine blades and vanes in modern aero-engines and also in land-based gas turbines.

Polycrystalline Ni-based superalloys are in use since 1950 and subsequently continuous efforts are being made to increase the capability of these materials to enable the aero-engines to operate at higher temperatures. The efficiency of these turbine engines depends on the turbine entry temperature (TET), which is limited by the high-temperature strength and behavior of these superalloys [1, 2]. With continuous efforts to increase the capability of the engine, around 1970 and 1980 conventional polycrystalline alloys gave way to columnar grained and single crystalline (SX) materials. Figure 1.1 illustrates the relative life (life normalized with respect to the conventional polycrystalline superalloys) of the creep strength, thermal fatigue resistance and corrosion resistance of the conventional polycrystalline, columnar grain and single crystal Ni-based superalloys. These properties of single crystals are much superior to those of other forms. For example, as the grain boundaries are weakest under tensile loading conditions, their elimination perpendicular to the loading direction in the columnar crystals and the single crystals improved the creep resistance of the alloys. Polycrystalline materials have many grains while single crystal is equivalent to one grain containing a few low-angle boundaries and many γ/γ' interfaces. Therefore, the advantage of SX over polycrystalline is the elimination of grain-boundaries and also the removal of B, C etc. as grain boundary strengthening solutes. Since these solutes have relatively low melting temperatures, their elimination leads to increase in the incipient melting temperature (localized melting due to chemical segregation), and hence the operating temperatures.

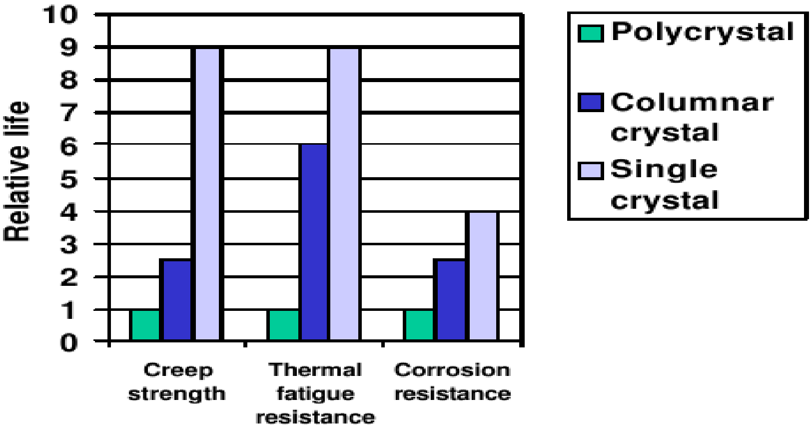

Figure 1.1: Critical parameters and their relation with relative life of various types of Ni-based superalloys [1].

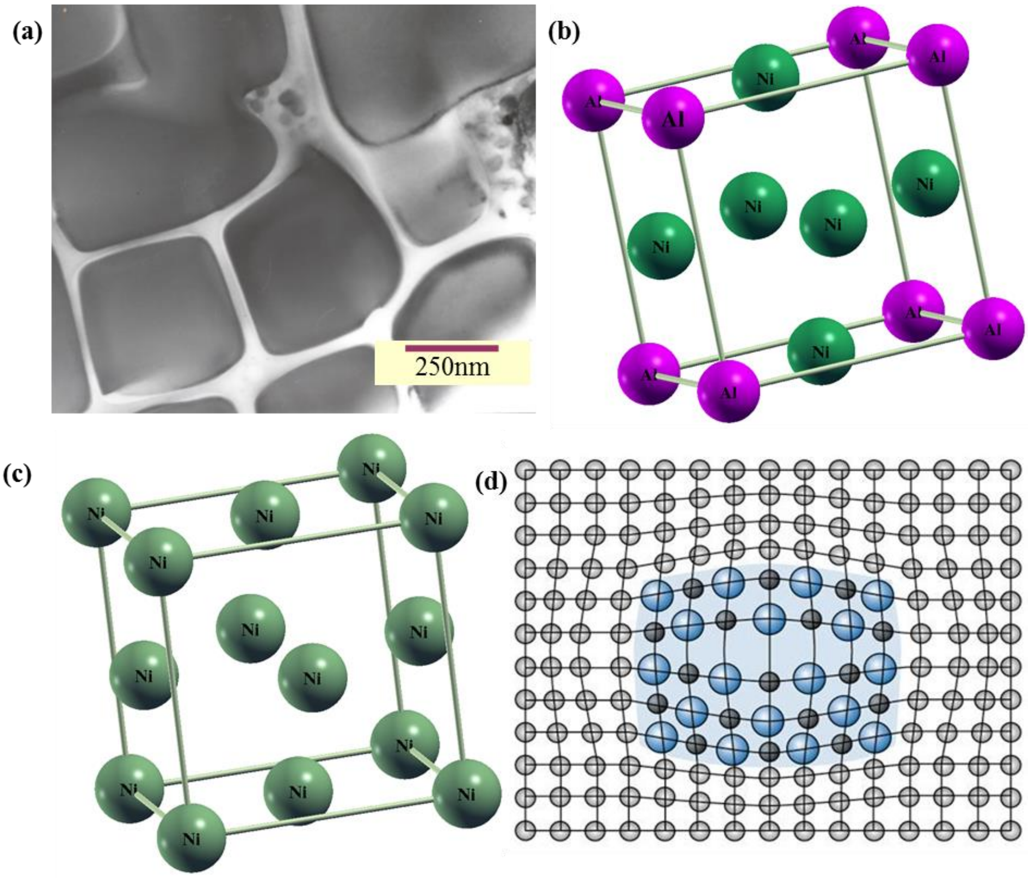

Figure 1.2: (a) Microstructure of γ-γ′ matrix [3] (b) γ′ phase with the Al atoms occupying corners of the cube and the Ni atoms located at the cube faces (c) γ phase with all the sites occupied by Ni atoms and (d) coherent interface between γ-γ′ [1].

The superior mechanical strength of Ni-based single crystal superalloys (NBSX) is attributed primarily to their microstructure that consists of cuboidal γ' precipitates which are in complete coherence with the γ matrix (Figure 1.2a) [1, 3, 4]. γ' is an ordered intermetallic based on Ni_3Al having $L1_2$ structure (Figure 1.2b) and γ is essentially Ni-rich solid solution (FCC structure) containing a number of substitutional alloying elements (Figure 1.2c). Even though γ' phase is the precipitate, present commercially available blade alloys have a volume fraction as high as 70% that are evenly distributed throughout the matrix [1]. The difference in lattice parameters of γ and γ' phases with several solute additions is kept low so as to maintain complete coherence between the precipitate and the matrix phase (Figure 1.2d) [1], and hence providing higher precipitation hardening. The microstructure is also designed to be stable along with the rate of coarsening at elevated temperatures to be low, which is achieved by having low interfacial energy between γ and γ'. Addition of refractory materials in the NBSX alloys significantly enhances mechanical properties of the system by decreasing the coarsening kinetics as well as providing solid solution strengthening to the system [1].

1.2 Strengthening mechanisms in Ni-based single crystal superalloys

Strengthening mechanisms are those which prevent deformation by impeding the movement of dislocations through the material. In Ni-based superalloy the two common strengthening mechanisms are precipitation hardening and solid solution strengthening which are influenced by the addition of various alloying elements. In addition, solid solution strengthening of the γ matrix reduces the mobility of dislocations between the γ' particles. However, Ni_3Al being ordered intermetallic, most potent strengthening mechanism that outweighs these at temperatures close to the melting temperature is the order strengthening.

1.2.1 Solid solution strengthening

Solid solution strengthening is being achieved with solutes that have large difference in their atomic size and moduli as compared to that of solvent atom along with reasonable solid solubility. Large size variation generates stress field around the solutes which influences the movement of the dislocations.

At elevated temperatures, the deformation mechanism involves dislocation cross-slip. Dislocation present in the lattice distorts the bond and hence increases its energy. The elastic energy of the dislocation per unit length is proportional to the square of the magnitude of the Burgers vector ($\vec{b}$). Hence minimization of the energy and reduction in the energy barrier for dislocation movement for FCC materials, such as Ni, is facilitated by the dissociation of perfect dislocations, $\vec{b}$, into Shockley partials, $\overrightarrow{b_1}$ and $\overrightarrow{b_2}$ as

$$\frac{1}{2}[\bar{1}10] \rightarrow \frac{1}{6}[\bar{1}2\bar{1}] + \frac{1}{6}[\bar{2}11] + SF,$$

where SF, the stacking faults, is the region encompassed by the partial dislocations. Further details are described in chapter 4. Cross-slip can be reduced by adding elements which lower the stacking fault energy of Ni and produce wider stacking faults. Also, solutes having higher melting point than the solvent provide creep resistance by reducing its diffusivity.

1.2.2 Precipitation strengthening

Most of the strength of single crystal superalloys results from the precipitation of the $L1_2$, ordered γ'. These precipitates are formed by carrying out long time ageing of the super-saturated solid solution. The similarity in the structure and the lattice parameter of γ and γ' allows homogeneous nucleation of a coherent and reasonably ductile γ' which has extraordinary high-temperature stability. In single crystal superalloys most of the strengthening is achieved by the γ' precipitate from slowing or obstructing the passage of dislocations either by forcing them to by-pass or shear through them.

1.2.3 Order strengthening

Dislocation movement in FCC material, such as γ, takes place along shortest lattice vector lying in the close packed plane i.e. dislocation glide along ${}^{1}/_{2}\langle 1\bar{1}0\rangle\{111\}$. Lattice vectors refers to the translation that keeps the crystal lattice unchanged. The shortest lattice vector for Ni_3Al, because of $L1_2$ crystal structure, is <100>. But this vector does not reside in the close-packed plane {111}. The shortest lattice vector on the {111} plane for Ni_3Al is $\langle 1\bar{1}0\rangle$ which is twice in magnitude in comparison to the FCC materials. Hence, dislocation movement in this ordered intermetallic is extremely complex. At low temperatures, dislocations glide along ${}^{1}/_{2}\langle 1\bar{1}0\rangle\{111\}$ resulting in the generation of antiphase boundary (APB), which requires substantial energy penalty arising from the formation of forbidden bonds [1]. Another dislocation movement is required to eliminate the APB generated by the earlier dislocation. The simultaneous movement of two dislocations is called *superdislocation*. Further energetics govern the dissociation of *superdislocation* into *superpartials* encompassing a region of stacking faults such as superlattice intrinsic stacking fault (SISF) and complex stacking fault (CSF) [5]. Detailed descriptions are reported in chapter 5. Hence a dislocation travelling in the matrix phase cannot enter the Ni_3Al (precipitate) phase without generating an APB which results in substantial order strengthening [1].

1.3 Factors to be considered for alloy design

The driving force behind the improvement of Ni-based superalloys is to improve the operating efficiency of the turbine engine. The primary factor that governs the efficiency is the operating temperature. Maximum improvement in the operating temperature has been achieved by tuning the microstructure that comprises essentially of the size, morphology and distribution of γ' precipitates in the γ matrix of the alloy. The planar defects such as APB in Ni_3Al and stacking faults in both the phases which are resultant of the dislocation dissociation reactions are associated with certain additional energies. The high-temperature properties of the alloys are significantly dependent on these fault energies. Also the coherency between the γ and γ' is ensured if the stress-free lattice misfit (δ) between γ and γ' is not large and the γ/γ' interfacial energy remains low. Solute substitution in Ni-based superalloys are also expected to affect the interfacial energy. Computationally it is estimated from the Griffith work of rupture (G_c) and is defined as the energy needed to cleave a crystal about a plane [6]. Since Ni-based superalloys, in general, contain more than ten alloying elements it is essential to understand the role of each alloying element on the fault energies and G_c in order to design alloys with specific targeted properties.

1.4 Role of modeling and simulation

Design of superalloys has advanced over many decades and has been mostly carried out using traditional route through trial-and-error based empirical procedures. This method is not only time consuming but expensive as well. With the advancement of the computing resources, it has become very efficient and effective to use modeling and simulation tools to overcome some of the challenges of the experimental techniques.

The description of mechanical properties of materials greatly depends on the relevant length-scales. Hence, numerous efforts are being made by scientists to understand the mechanical behavior at the different length-scales through computer simulations. For example, macroscopic description of deformation of materials is being carried out using continuum description, for which finite element method (FEM) is being widely used as the numerical technique. In the continuum description, constitutive equations relating stress and strain of the systems under deformation are considered. Relevant partial differential equations are solved considering representative volumes elements.

The overall mechanical properties of the crystal are governed by the movement of dislocations. At length-scales below the continuum description is the microstructure and dislocation modeling which are used at the mesoscopic range (1µm to 100µm). Dislocation Dynamics (DD) is a modeling approach that aims to simulate the motion and interaction of these dislocation to gain insights concerning the mechanical strength of the crystal. The stress induced by any arbitrary dislocation loop at an arbitrary field point is computed by the Peach-Koehler integral equation given in Hirth and Lothe (1982) [7].

However, the most critical among many parameters will be a thorough understanding of the physics behind the interactions of the alloying elements at the atomistic length scale. The knowledge and data generated can be used as an input to address properties at different length-scales required in the development of newer and more efficient superalloys.

1.4.1 Atomistic simulations

The atomistic simulation techniques can address the length-scales of the order of 100s of nm. Molecular Dynamics (MD) is one such technique wherein atoms ranging from several thousands to millions can be handled. MD uses classical equation of motion for the atoms to determine their trajectories where the forces and energies between interacting particles are calculated from the interatomic potential field. However, construction of the potential requires lot of parametric input (or physical properties) which are usually obtained from experiments as well as from first-principles calculations. This method is widely used in the investigation of the atomistic aspects of dislocations, such as the core structure, extended dislocations and individual defect-dislocation interaction. A recent application for the simulation of brittle cleavage of Ir [8] demonstrates the power of such large-scale simulations. Nevertheless, these methods rely on the model potential and consequently, still some more progress has to be made to realize their predictive power. It becomes particularly hard when different types of atoms constitute a material.

Modeling interactions without a priori knowledge of the bonding present requires the use of first-principles methodologies, in which one attempts to solve the Schrödinger equation governing the electronic dynamics. This method captures the physics of bond-breaking or forming process and can be considered to be highly accurate and predictive while describing the atomic interactions. One such method is the density functional theory (DFT) [9] which requires only position and atomic number of the involved species as input. However, the solution in full quantum mechanical framework is extremely computationally expensive. Even with suitable justified assumptions, only a few hundreds of atoms can be addressed in the first-principles DFT [9, 10]. The solution to the Schrödinger equation is carried out through the determination of a single electronic density function $n(\vec{r})$ and not the many body wave functions. Hence, once $n(\vec{r})$ is determined the properties of the system are uniquely defined. Another beauty of this technique is the advantage of being completely transferable (ability to describe atoms in different chemical environments), requiring only the atomic constituents of the system under consideration to be specified.

The DFT approaches have proved to be of general and predictive nature for various problems in materials science [11-14]. This technique calculates many important parameters that are required for a large-scale modeling, for example, results of brittle energy cleavage calculations might provide input for the cohesive zone models [15, 16], or the Γ-surface may be used to determine dislocation core structures and dislocation dissociation by means of the Peierls-Nabarro model of dislocation [17- 23]. Generalized stacking fault energy surface (GSF) or Γ-surface introduced by Vitek [20, 24], is defined as the energy cost or work done to form a plane fault by an in-plane relative shift $\vec{q}$ of one part of the crystal against the another. The GSF reflects the symmetry of the crystal with minima and maxima of the energy for a lattice translation corresponding to the stable and unstable stacking faults (USF) energies.

1.5 Overview of the thesis

In this thesis an attempt has been made to address some critical aspects of properties that can be modelled using DFT for Ni-based superalloy. An effort is made to acquire better understanding of the trends in effects of substitutional solutes element belonging to 3d, 4d and 5d series of transition metals (TM) on the two major phases γ and γ' present in Ni-based superalloy.

The computational details and brief overview about first-principles DFT is described in chapter 2.

In chapter 3, we examine the effects of substitution of solutes on the cell volume of Ni. In order to understand the effect of interaction between solutes on the volume of the Ni-based solid solution, we consider solute atoms in four configurations, viz 1st, 2nd, 3rd and 4th nearest neighbour (NN). With the volume changes associated with solute substitution, Vegard's coefficients for solutes in γ phase are calculated. The binding energies (BE) associated with these solutes are calculated to provide insights into their tendency in Ni solid solution towards clustering.

In Chapter 4, we determine effects of different solutes on the stacking fault energy of Ni. In addition, we obtain unstable stacking fault energies (USFE, γ_{us}) of pure as well as the alloyed system.

A systematic analysis of the influence of substitution of solute atoms from the 3d, 4d and 5d transition metals at the Ni or Al or simultaneously at Ni and Al atoms separated as first nearest neighbour in the (111) fault plane of Ni_3Al on the USFE, the SISFE and the APBE is presented in chapter 5.

Changes in the Griffith work of rupture (G_c) change associated with solutes from the 3d, 4d and 5d transition metals substituted in Ni are determined in chapter 6. We also calculate elastic constants of Ni-based solid solutions with solutes from 4d and 5d TMs, and compare the changes in the ductility parameter arising from solute substitution using Griffith's and Pugh criteria.

Chapter 2

Computational Methodology

Properties of materials are determined by the interactions between the nuclei and their electrons. Classical Newtonian mechanics cannot capture these interactions and hence is inadequate to explain many phenomena occurring at the atomic scale. Quantum mechanics emerged as a complementary discipline to classical mechanics, and has been very successful in explaining numerous complex materials related phenomena. The crux of this method is to solve the time-independent Schrödinger equation so as to obtain the materials properties. Since it is not possible to obtain closed-form analytical solution for this equation for many-body problems of interest to materials community, it is indispensable to use numerical/computational techniques. However, these quantum mechanical simulation techniques that involve only fundamental physical constants and atom co-ordinates as inputs are computationally intensive. Even with tremendous development in the computational resources these types of calculations, with reasonable approximations, are limited to a few hundreds of atoms.

2.1 The Schrödinger equation

The properties of a system may be obtained by solving the quantum mechanical wave equation governing the system dynamics. For non-relativistic systems, this is done by solving the Schrödinger equation of the form:

$$\hat{H}\Psi(\vec{r}) = E\Psi(\vec{r}), \qquad 2.1$$

where H is the Hamiltonian operator describing the kinetic energy and interaction between particle, and, Ψ and E represent the wavefunction and energy of the particular state of the system. The solution to this equation gives the allowed energy levels of quantum mechanical systems.

2.1.1 Total energy function

In condensed matter, interactions in a system comprise of those between the constituent atoms through Coulombic (electrostatic) forces which are specified in terms of their atomic numbers and the coordinates of nuclei and electrons. The total non-relativistic Hamiltonian of a system consisting of P number of atoms and Q electrons, can be written in a general form [25]:

$$\hat{H} = -\sum_{I=1}^{P} \frac{\hbar}{2M_I} \nabla_I^2 - \sum_{i=1}^{Q} \frac{\hbar}{2M_i} \nabla_i^2 - e^2 \sum_{I=1}^{P} \sum_{i=1}^{Q} \frac{Z_I}{|\vec{R}_I - \vec{r}_i|} + \frac{e^2}{2} \sum_{I=1}^{P} \sum_{J \neq I}^{P} \frac{Z_I Z_J}{|\vec{R}_I - \vec{R}_J|}$$

$$+ \frac{e^2}{2} \sum_{i=1}^{Q} \sum_{j \neq I}^{Q} \frac{1}{|\vec{r}_i - \vec{r}_j|}, \qquad 2.2$$

where $\vec{R} = \{\vec{R}_I\}, I = 1, \ldots, P$, is a set of P nuclear coordinates and $\vec{r} = \{\vec{r}_i\}, i = 1, \ldots, Q$, is a set of Q electronic coordinates. Z_I and M_I are the nuclear charges and masses, respectively, and e is the electronic charge. The first two terms represent the kinetic energy of the nuclei and the electrons respectively. The third term gives the attractive electrostatic interaction between the electrons and nuclei. The fourth and fifth terms are the repulsive Coulomb between nuclei and between electrons respectively.

The total Hamiltonian can be rewritten in a compact form as [25]:

$$\hat{H} = \hat{T}_N(\vec{R}) + \hat{T}_e(\vec{r}) + \hat{V}_{eN}(\vec{r}, \vec{R}) + \hat{V}_{NN}(\vec{R}) + \hat{V}_{ee}(\vec{r}), \qquad 2.3$$

where *T* and *V* refer to the kinetic and potential energy operators with the subscripts *N*, *e* referring to the nucleus and electrons, respectively.

The solution to the many-body Schrödinger equation can, in principle, be used to derive most of the mechanical properties. Unfortunately, solution to this equation in a full quantum-mechanical framework is practically impossible. Only in a few cases, limited to a small number of particles, exact solution is available. The reasons for the difficulty to find analytical solutions are

1. Systems are mostly multicomponent and hence are many-body.
2. Electrons being fermions have antisymmetric many-body wavefunctions.
3. Nuclei can be fermions, bosons or distinguishable particles, according to the particular problem under examination.
4. The electrostatic interaction between the nuclei and electrons prevents the separation of complete molecular wavefunctions into electronic and nuclear terms. This leads to dealing with wavefunctions of (3P + 3N) coupled degrees of freedom.

Hence, in practice, the complexity associated with the solution of this ‘many-body’ problem forces us to use some reasonable approximations and simplifications. The large majority of the calculations presented in the literature are based on two approximations namely: (i) Born-Oppenheimer approximation (adiabatic approximation) and (ii) classical treatment of motion of nuclei.

2.1.2 Born-Oppenheimer approximation

The Born-Oppenheimer approximation [25], (also called adiabatic approximation), is introduced to decouple the motions of the electrons and the nuclei. The Coulombic interaction between electrons-nuclei ($\hat{V}_{eN}$) prevents separation of the total Hamiltonian (equation 2.3) into electronic and nuclear part. It is thus assumed that the electronic wavefunctions depend only on the positions of the nuclei but not on their momentum. The basis for this assumption is based on the fact that the mass of a proton is 1836 times that of an electron and hence the velocity of electrons is typically much higher when compared to that of nuclei. Thus nuclei can be thought of as fixed with respect to electrons on the time-scale of remaining in the same instantaneous stationary state of the electronic Hamiltonian. With this assumption it is reasonable to take into consideration only the electronic degrees of freedom. Also, the kinetic energy operator of the nuclei $\hat{T}_N$ can be neglected since $\hat{T}_N$ is smaller than $\hat{T}_e$ by a factor of M_A/μ_e, where μ_e is the reduced mass of an electron. Thus, the total Hamiltonian for fixed nuclear configuration ($\hat{H}_{el}$) is written as [25]:

$$\hat{H}_{el} = \hat{T}_e(\vec{r}) + \hat{V}_{eN}(\vec{r},\vec{R}) + \hat{V}_{ee}(\vec{r}) + \hat{V}_{NN}(\vec{R}), \qquad 2.4$$

and hence can be considered as a sum of electronic Hamiltonian ($\hat{H}_e$) and Coulomb interaction between nuclei ($\hat{V}_{NN}$), where [25]:

$$\hat{H}_e = \hat{T}_e(\vec{r}) + \hat{V}_{eN}(\vec{r},\vec{R}) + \hat{V}_{ee}(\vec{r}). \qquad 2.5$$

It is important to note that when nuclear configuration in the total Hamiltonian (equation 2.4) is fixed, it is assumed that the nuclear coordinates are no longer contributing to the full wavefunctions. Hence, the nuclear repulsion (V_{NN}) contributes to the total energy by augmenting it with some value. This is possible only when the nuclei are treated as classical particles.

With these approximations, we are left with the problem of solving the many-body electronic Schrödinger equation for ground state for a set of fixed nuclear positions of the form

$$\hat{H}_e \Psi_G(\vec{r},\vec{R}) = \hat{H}_G \Psi_G(\vec{r},\vec{R}), \qquad 2.6$$

where (E_G) is the ground state energy of the system and the total energy of the system (E_{total}) is calculated as

$$E_{total} = E_G + V_{NN}. \qquad 2.7$$

E_{total} has all the material-specific information except for electronic excitations. For system containing one electron, the time independent non-relativistic Schrödinger equation (Equation 2.1) can be solved precisely. Complex electrostatic interactions between electrons lead to problems when another electron is introduced.

2.1.3 Quantum mechanics of electrons

Using the Born-Oppenheimer approximation, the problem is reduced to that of a gas of interacting electrons moving in a static external potential due to the nuclei. This simplified quantum many-body problem is still too complex to solve for large systems. Since the wavefunction of the many-body system depends on the coordinates of each particle, the wavefunction based treatment of any system larger than few electrons is not feasible. In order to deal with realistic materials, further approximations have to be made. Density functional theory (DFT), provides an enormous simplification of this many-body ground state problem.

2.2 Density functional theory: A first-principles approach

DFT, based on Hohenberg-Kohn theorems [9] and Kohn-Sham equations [10], allow the replacement of the many-electron wavefunctions with the electron density of the system. It is also shown that the system of interacting electrons can be mapped to a system of non-interacting particles. Hence, the many electron problem is mapped to an effective one electron problem thus reducing the complexity of the problem to a great extent.

2.2.1 Hohenberg-Kohn formalism

In 1964, the foundation for DFT was provided by two theorems, proved by Hohenberg and Kohn (H-K) [9], stated below [25]:

Theorem 1: *For any system of interacting particles in an external potential* $\hat{V}_{ext}(\vec{r})$*, the potential* $\hat{V}_{ext}(\vec{r})$ *is determined uniquely, except for a constant, by the ground state particle density* $n_o(\vec{r})$*.*

Theorem 2: *A universal functional for the energy $E[n(\vec{r})]$ in terms of the density $n(\vec{r})$ can be defined, valid for any external potential $\hat{V}_{ext}(\vec{r})$. For any particular $\hat{V}_{ext}(\vec{r})$, the ground state energy of the system is the global minimum value of this functional, and the density $n(\vec{r})$ that minimizes the functional is the exact ground state density $n_o(\vec{r})$.*

The first theorem suggests one-to-one correspondence between the $\hat{V}_{ext}(\vec{r})$ and the density $n(\vec{r})$. Hohenberg and Kohn could show that for any system of interacting particles in an external potential $\hat{V}_{ext}(\vec{r})$, this potential is uniquely determined by the ground state electronic density $n_o(\vec{r})$. $\hat{V}_{ext}(\vec{r})$ is the Coulomb potential arising from the nuclei ($\hat{V}_{eN}(\vec{r},\vec{R})$) in the electronic Hamiltonian H_e in equation 2.5. The electronic Hamiltonian can be rewritten as $\hat{H}_e = \hat{T}_e(\vec{r}) + \hat{V}_{ee}(\vec{r}) + \hat{V}_{ext}(\vec{r}) \left(\hat{V}_{eN}(\vec{r},\vec{R})\right)$ for all P-electron systems, so that the H_e, and hence the ground-state property are completely determined by P (total number of electrons) and $\hat{V}_{ext}(\vec{r})$.

According to the second H-K theorem a *universal functional* valid for any external potential $\hat{V}_{ext}(\vec{r})$ can be defined for the ground state energy $E[n(\vec{r})]$ in terms of density $n(\vec{r})$. For any particular $\hat{V}_{ext}(\vec{r})$, the exact ground state energy of the system is the global minimum value of the energy functional. The density that minimizes the functional is the exact ground state density $n_o(\vec{r})$. For a given potential the energy functional is given as [25]:

$$E[n(\vec{r})] = \int \hat{V}_{ext}(\vec{r}) n(\vec{r}) d\vec{r} + F_{HK}[n(\vec{r})], \qquad 2.8$$

where $F_{HK}[n(\vec{r})]$ is a universal Hohenberg-Kohn density-functional of the electron density for any many-electron system. The functional $F_{HK}[n(\vec{r})]$ is purely electronic part of the energy, consisting of the kinetic energy of the electrons and the electron-electron interaction. Thus, $F_{HK}[n(\vec{r})]$ can be written as,

$$F_{HK}[n(\vec{r})] = Min_{\Psi} \langle \Psi | T + V_{ee} | \Psi \rangle, \qquad 2.9$$

with a constraint that Ψ gives a density $n(\vec{r})$. $F_{HK}[n(\vec{r})]$ contains no information on the nuclei and the nuclear positions. Consequently, this functional is same for all many-electron systems.

The one-to-one correspondence between ground state electronic charge density and ground state energy established by the Hohenberg-Kohn theorems reduces the problem of finding the wavefunctions of 3N variables to that involving determining the ground state electronic density function of three variables. However, the two H-K theorems do not offer a way of determining $F_{HK}[n(\vec{r})]$ and thus no practical scheme for determining the ground-state density of a system. One year later in 1965 Kohn and Sham [10] came out with a derivation to solve this and thus paving a practical path for solution for this functional.

2.2.2 Kohn-Sham ansatz

In 1965 Kohn and Sham [10] proposed to rewrite the $F_{HK}[n(\vec{r})]$ to facilitate solution to equation 2.6. They could show that the solution is simplified if the exact Hamiltonian of an interacting many-body systems can be mapped onto fictitious non-interacting single particle Hamiltonian. With Kohn-Sham treatment $F_{HK}[n(\vec{r})]$ can be represented as [25]:

$$F_{HK}[n(\vec{r})] = T_0[n] + E_H[n] + E_{xc}[n], \qquad 2.10$$

where $T_o[n]$ is the kinetic energy functional for non-interacting electrons of the form

$$T_o(n) = -\frac{\hbar^2}{2m}\left[\sum_i \langle\psi_i|\nabla^2|\psi_i\rangle\right], \qquad 2.11$$

and $E_H[n]$ is the electrostatic interaction energy (called Hartree energy) of the electrons, arising from the mutual Coulomb repulsion of all electrons:

$$E_H[n] = \frac{1}{2}\iint \frac{n(\vec{r})n(\vec{r}')}{|\vec{r}-\vec{r}'|}d\vec{r}d\vec{r}' \qquad 2.12$$

The last term $E_{xc}[n]$ is the exchange-correlation functional, a correction term, which accounts for all many-body effects in $F_{HK}[n(\vec{r})]$ and is discussed in the section 2.2.3.

Thus the simplified total energy functional can be rewritten as Kohn-Sham Hamiltonian E_{ks} [25]:

$$E_{KS} = T_o[n] + E_H[n] + E_{xc}[n] + \int \hat{V}_{ext}(\vec{r})n(\vec{r})d\vec{r} \quad 2.13$$

Equation 2.13 can be interpreted as the energy functional of non-interacting particles in two potential $\hat{V}_{ext}(\vec{r})$ *and* $E_{xc}[n]$.

The exact ground-state density $n(\vec{r})$ *of an N-electron system is* [25]:

$$n(\vec{r}) = \sum_{i=1}^{N} \psi_i(\vec{r})\psi_i^*(\vec{r})\,, \qquad 2.14$$

where the single-particle wavefunctions $\psi_i(\vec{r})$ are the *N* lowest energy solutions of the Kohn-Sham equation

$$\hat{H}_{KS}\psi_i(\vec{r},\vec{R}) = \varepsilon_i\psi_i(\vec{r},\vec{R}), \qquad 2.15$$

where ε_i is the ground state energy and has all the material specific information, except for electronic excitation. Hence, Schrödinger like single-particle equations have to be solved to obtain the ground-state density of the many-body system.

It is important to note that the Kohn-Sham Hamiltonian depends on the electron density through the Hartree and the exchange-correlation terms, while the electron density depends on the ψ_i to be calculated. This leads to the solution of a non-linear self-consistency problem where the solution determines the original equation. Hence the solution can only be achieved by following an iterative process. Initially the Kohn-Sham Hamiltonian is constructed with an initial guess for the density and the solution results in a new set of ψ_i and a new electron density. This new electron density is used to construct a new H_{KS}, and the loop is continued until the succeeding densities are the same within a tolerance.

2.2.3 Exchange-correlation functional

In order to solve the Kohn-Sham equation, exchange-correlation functional $E_{xc}[n]$ has to be known. However, the functional form of the $E_{xc}[n]$ is unknown and hence reasonable approximation has to be made. Two most widely used approximations are the local density approximation (LDA) and the generalized gradient approximation (GGA).

The simplest approximation used is LDA which defines the $E_{xc}[n]$ as [10]:

$$E_{xc}^{LDA}[n] = \int n(\vec{r})\, \varepsilon_{xc}[n(\vec{r})] d\vec{r}\,, \qquad 2.16$$

where ε_{xc} stands for exchange-correlation energy per particle of a homogeneous electron gas with interacting electrons and is numerically known from Quantum Monte Carlo calculations. LDA is assumed to depend only on the density at the coordinate where it is evaluated and also the density distribution is assumed not to vary too rapidly. Under this approximation, for each point in space the exchange-correlation energy is approximated locally by the exchange-correlation energy of a homogeneous electron gas with the same electron density as present at that point.

For systems where charge densities vary rapidly i.e. non-uniform, the exchange-correlation energy can deviate significantly from the uniform result obtained using the LDA. A more sophisticated approximation involves GGA, which considers gradient of the total charge density. While LDA depends only on the local density $n(\vec{r})$, GGA incorporates the gradient in density as well:

$$E_{xc}^{GGA}[n] = \int n(\vec{r})\, \varepsilon_{xc}[n(\vec{r}), |\nabla n(\vec{r})|] d\vec{r}. \qquad 2.17$$

GGAs tend to improve total energies [26], atomization energies [26-28], energy barriers and structural energy differences as compared to LDA [29-32]. GGAs expand and soften bonds as well as favour density inhomogeneity more than LDA [32]. In our calculations we have used GGA based approximations to account for the exchange-correlation energy.

2.3 Basis sets

The effective one-electron Kohn-Sham equations (Eqn. 2.15) are non-linear partial differential equations involving eigenvalue problem that are iteratively solved by representing the electronic wavefunctions by a linear combination of a set of basis functions. The commonly used basis functions are plane waves, atomic orbitals or a combination of both (known as mixed basis). However, because of its simplicity, the most common basis functions are the plane waves.

2.3.1 Plane wave basis

The solution to the problem, even after these assumptions, is still computationally intensive and scales as N^3, where N is the number of atoms in our system [25]. With this formalism, solution for bulk systems is practically impossible unless the periodicity of the bulk crystal is exploited and reduce the problem to be addressed from infinite to finite size. However, while considering a finite size, false periodicity is being imposed by the construction of a supercell which is then replicated periodically throughout (Figure 2.1). The region confined within the green box is actually the supercell that is used for calculation and the region within the dotted box are its images. Hence for any translation of the red atom to new position marked in blue, its images (marked with dotted arrow) experiences the same. Sufficient care should be taken while constructing a supercell such that the structural features such as defects contained within each one, which in reality is isolated, do not interact significantly.

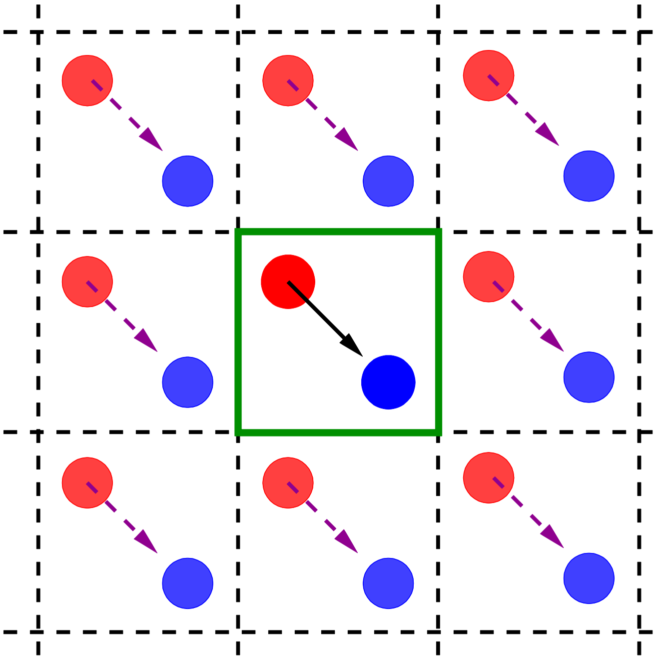

Figure 2.1: Periodic boundary conditions and construction of a supercell (region within the green boundary).

Atoms in crystalline system are arranged in a regular periodic array described by the Bravais lattice vector $\vec{R}$. The system, being infinite, is invariant under translation by any set of these lattice vectors, and in particular the potential is also periodic i.e.

$$V(\vec{R} + \vec{r}) = V(\vec{r}), \qquad 2.18$$

The theorem of Bloch shows that the electronic wavefunction in a periodic system can be written as the product of periodic part and wave-like part [25]:

$$\Psi_{n\vec{k}}(\vec{r}) = \exp(i\vec{k}.\vec{r})\mathrm{u}_{n\vec{k}}(\vec{r}), \qquad 2.19$$

where $\vec{k}$ is a vector in the first Brillouin zone, $\Psi_{n\vec{k}}(\vec{r})$ is the wavefunction, $\mathrm{u}_{n\vec{k}}(\vec{r})$ is periodic in the same way as the crystal lattice ($\mathrm{u}_{n\vec{k}}(\vec{r} + \vec{R}) = \mathrm{u}_{n\vec{k}}(\vec{r})$ for all $\vec{R}$ in the Bravais lattice). This periodic term is expanded as a linear sum of plane-waves with wave vectors that are reciprocal lattice vectors of the crystal and is represented as [25]:

$$\mathrm{u}_{n\vec{k}}(\vec{r}) = \sum_{G} C_{\vec{G}}^{n\vec{k}} exp\left(i\vec{G}.\vec{r}\right) \ , \qquad 2.20$$

where $\vec{G}$ sums over the reciprocal lattice vectors (at least in principle), and $C_{\vec{G}}$ are coefficients in the expansion. In actual calculations, we have to limit the plane wave expansion at some point to make it computationally feasible. The point at which we truncate the basis set is called the plane-wave cutoff. The highest included wave vectors $(\vec{k} + \vec{G})$ of plane waves in a basis set is determined by an energy cutoff E_{cut} using the following equation:

$$\frac{\hbar\left|\vec{k} + \vec{G}\right|^2}{2m_e} < E_{cut}. \qquad 2.21$$

An advantage of plane waves is that the sums needed to go back and forth between reciprocal space and real space can be performed efficiently using fast Fourier transforms (FFTs). They are called ‘plane waves’ because surfaces of constant phase are parallel planes perpendicular to the direction of propagation. By limiting the plane wave expansion to the discrete set of $\vec{G}$ vectors that are sums of integer multiples of the three primitive lattice vectors, we are selecting plane waves that have a periodicity compatible with the periodic boundary conditions of our direct lattice. In general, the properties of a periodic system are correctly described only if a sufficient number of k-vectors are sampled from the Brioullin zone. However, when a calculation is carried out for all electrons associated with the atoms, a large number of plane waves is required to expand the wavefunctions in the core region. The wavefunctions of core electrons because of strong nuclear Coulomb interaction are highly localised and oscillating, which are difficult to represent computationally (Figure 2.2). This problem is resolved by using *pseudopotential*s that eliminates the numerical problems associated with the electron-ion interaction.

2.4 Pseudopotentials

Most properties of the systems are determined by the valence electrons with little contributions from the core electrons (electrons that are bounded strongly to the nucleus). It is thus assumed that the core electrons contribution to the total binding energy does not change when isolated atoms are brought together to form a crystal. Therefore, the actual energy differences of interest are the changes in valence electron energies, and so if the binding energy of the core electrons can be subtracted out, the valence electron energy change will be a much larger fraction of the total binding energy, and hence much easier to calculate accurately.

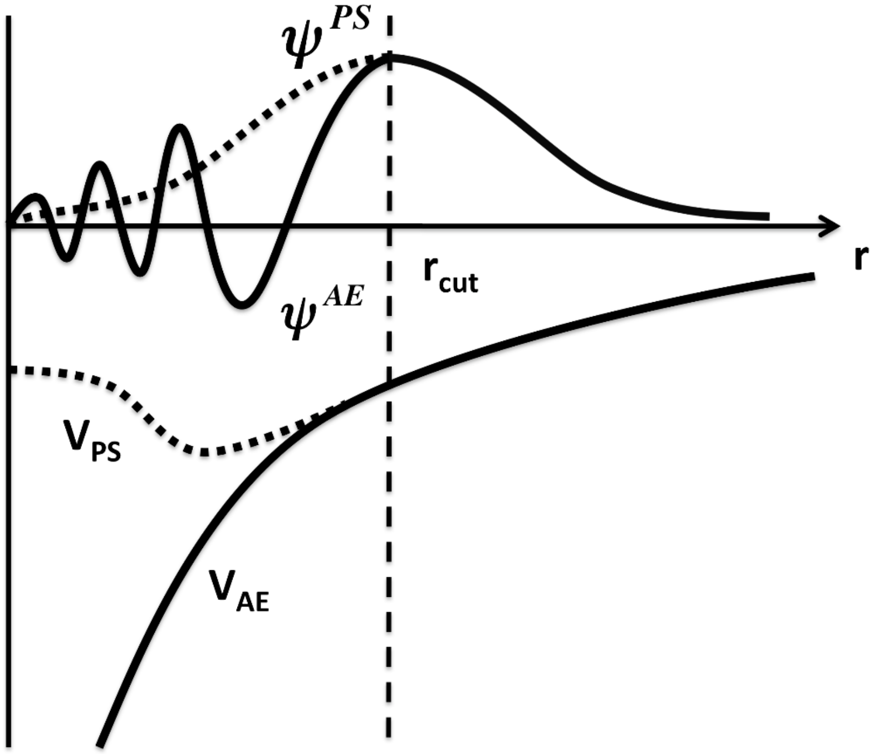

Figure 2.2: Schematic diagram comparing relationship between an all-electron (*Ψ*, blue) and pseudo wavefunction *(Ψ*$_{pseudo}$*, red)* along with their potentials. The real and the pseudo wavefunction and potentials match above the cutoff radius *r*$_{cut}$.

Specially constructed non-singular electron-ion potential (*pseudopotential*) is used in place of all electron potential. This *pseudopotential* replaces the core electrons and the nucleus with an effective potential which mimics how the valence electrons experience the potential of the nucleus (Figure 2.2). Effective *pseudopotential* is constructed by considering a cutoff radius (r_{cut}), the boundary separating the core and valence regions (Figure 2.2) [33, 34]

$$\Psi^{AE}(\vec{r}) = \Psi^{PS}(\vec{r}), r > r_{cut}, \qquad 2.22$$

where the actual wavefunctions (all electron, Ψ^{AE}) and pseudo wavefunctions (Ψ^{PS}) are the same beyond r_{cut} [35]. The transferability of the *pseudopotential* i.e. ability to describe an atom in different chemical environments, is crucial [36]. With increasing r_{cut}, the number of plane waves required to represent a pseudo wavefunction generally decreases but compromising its transferability. Hence, an optimal value of r_{cut} is required to be estimated.

The *pseudopotentials* eigenvalues should also be conserved

$$\epsilon_i^{AE} = \epsilon_i^{PS}. \qquad 2.23$$

The *pseudopotentials* should also follow the Norm-conservation criteria (total charge of each pseudo wave function should equal the charge of the all-electron wave function) [35] such that

$$\int_0^{r_{cut}} \left|\Psi_i^{AE}(\vec{r})\right|^2 d\vec{r} = \int_0^{r_{cut}} \left|\Psi_i^{PS}(\vec{r})\right|^2 d\vec{r}. \qquad 2.24$$

Norm conservation criteria states that the valence electrons are not affected by the replacement of smoother charge distribution for the core electrons as long as the total charge remains same.

With justified relaxation in the norm conserving *pseudopotential*s, ultrasoft *pseudopotentials* was proposed by Vanderbilt [37] to obtain smoother (mathematically less expensive, softer) pseudo wavefunctions. This was done through splitting the pseudo wave functions into two parts. The first part being ultrasoft valence wave functions

$$\Psi_i^{US}(\vec{r}), \qquad 2.25$$

that don't fulfill the norm conservation criteria, and the second part being core augmentation charge to account for the charge deficit in the core region

$$Q_{nm}(\vec{r}) = \Psi^{AE^*}{}_n(\vec{r})\Psi^{AE}{}_m(\vec{r}) - \Psi^{US^*}{}_n(\vec{r})\Psi^{US}{}_m(\vec{r}). \qquad 2.26$$

The ultrasoft potential takes the form:

$$V_{US} = V_{loc}(\vec{r}) + \sum_{nmI} D^0_{nm}|\beta^I_n\rangle\langle\beta^I_m| \;, \qquad 2.27$$

where the β-projector are strictly localized inside the cut-off region and is defined through:

$$|\beta_n\rangle = \sum_m \frac{|\chi_m\rangle}{\langle\chi_m|\Psi_n\rangle}. \qquad 2.28$$

The χ-functions are defined through:

$$|\chi_n\rangle = \left(\epsilon_n - \hat{T} - V_{loc}\right)|\Psi_n\rangle, \qquad 2.29$$

and D is defined as

$$D^0_{nm} = \langle\Psi_n|\chi_m\rangle + \epsilon_m q_{nm}. \qquad 2.30$$

where

$$q_{nm} = \int_0^{r_{cut}} Q_{nm}(\vec{r})d\vec{r}\,. \qquad 2.31$$

Therefore the ultrasoft *pseudopotential* is determined by $V_{loc}(\vec{r})$, D^0_{nm}, $Q_{nm}(\vec{r})$ and $\beta_n(\vec{r})$. The advantage with this *pseudopotential* is the requirement of less plane waves. In the present study ultrasoft *pseudopotentials* are used that are tuned to use the basis set with a very low energy cut-off without compromising the accuracy of the calculations.

2.5 Computational details

Quantum Espresso package [38] has been used to carry out first-principles DFT-based calculations with a plane wave basis and *pseudopotentials*. Plane wave basis truncated with an energy cutoff of 25 Ry is used to represent the wave functions and that of 200 Ry for density (convergence has been ensured for the above cut-off parameters). Ultrasoft *pseudopotentials* [37] are used to model ionic cores along with a generalized gradient approximation for the electron correlation and exchange energy with the Perdew-Burke-Ernzerhof functional [32]. Brillouin Zone integrations are sampled with suitable meshes for calculation with periodic supercell after checking the convergence with k-points. Hellman-Feynman forces on atoms and stresses are used to determine optimal crystal structures through minimization of total energy with the Broyden-Fletcher-Goldfarb-Shanno scheme. Convergence to minimum energy is achieved until either the difference in total energy between successive self-consistent cycles is less than 10^{-5} eV or the average force in the system is less than 0.02 eV/Å.

Chapter 3

Energetics of Substitutional Alloying and its Tendency to Cluster in Ni Solid Solution*

At higher operating temperature, the strength of Ni-based superalloys is primarily determined by its microstructure [40]. The microstructure essentially consists of ordered γ′ precipitates (based on Ni_3Al) with $L1_2$ crystal structure in a solid solution of γ matrix having FCC structure (Figure 1.1). For optimum strength to be achieved for the superalloys, Ni_3Al should be in complete coherence with the matrix in cube on cube orientation. It has been shown that one of the critical factors that control the morphology of coherent γ′ precipitates is the magnitude and sign of the stress-free lattice misfit (δ) between γ and γ′ [1]. δ is defined as

$$\delta = 2 \times 100 \times [{}^{(a_{\gamma'} - a_{\gamma})}\!\big/_{(a_{\gamma'} + a_{\gamma})}], \qquad 3.1$$

where a_{γ} and $a_{\gamma'}$ are the equilibrium lattice parameters of the γ and γ′ phases respectively. The composition of the solutes in these two primary phases along with the coefficient of thermal expansion determine the magnitude of δ. δ can be tailored based on the requirement by suitably alloying with elements, which partition preferentially to either γ or γ′ phase or into both phases, and contributing to the overall straining of the

---

* This work has been published in part in Comp. Mat. Sci [39]. Copyright (2018).

corresponding phase lattice. High values of δ increase the misfit stress leading to semi-coherent or incoherent interface resulting in loss of coherency and its related strength [1]. The misfit stress arising due to δ along with the applied stresses could be important driving force for dislocation motion during high-temperature low-stress creep. It is reported that in single crystal alloys, under tensile loading, negative misfit stimulates the formation of rafts perpendicular to the tensile force direction, which aids in reducing the creep rate [1]. Hence, one of the ways of controlling the lattice mismatch is to add prescribed quantities of solutes into the system. In order to achieve this, prior knowledge of volume changes associated with the addition of solutes is important.

In dilute alloys (wherein the solute concentration is low), the spacing between the individual solute atoms (in a disordered alloy) can be generally very large and the solutes can generally be considered to be isolated. However, it is essential to know whether the solutes prefer to have a tendency for segregation (clustering). From atomistic point of view, even with two solute atoms, several configurations need to be analyzed to discern this behavior. This can, in principle, be identified from the configuration that has minimum energy among the several possible configurations. An equivalent approach is based on the binding energy (BE) between the solute atoms. The magnitude and sign of BE would describe the preference for neighbouring bonds for an atom and hence is correlated to the preference for clustering [41].

In this chapter, we evaluate the changes in volume and calculate the lattice parameters of the alloyed systems and hence estimate the Vegard's coefficient for different solutes in Ni. We also estimate the BE between solutes when they are separated as 1st, 2nd, 3rd and 4th nearest neighbour (NN).

3.1 Computational details

In the present study, we estimate the change in lattice parameter with substitution of solutes from 3d, 4d and 5d series transition metals. In order to simulate system with different alloy composition (up to 6.7 at.% of solute), three different supercells with 32, 96 and 144 atoms of Ni have been considered. To estimate the BE, 96 atoms supercell of

γ phase have been generated with three orthogonal vectors along X, Y and Z directions as [$\bar{1}01$], [$\bar{1}2\bar{1}$] and [111] respectively with an arrangement of six layers with stacking sequence ABCABC along the <111> corresponding to close-packed FCC structure (Figure 3.1). The effect of solute substitution has been studied by substituting for either a single Ni atom (Figure 3.1) or two Ni atoms (Figure 3.2a-d) corresponding to ~1 at.% and ~2 at.% respectively. When two solute atoms are substituted they are placed such that they form 1st to 4th nearest neighbour configuration. All the systems have been relaxed completely (i.e. the atomic positions as well as the volume) to obtain minimum energy configuration to estimate the volume. Elements from 3d (Ti, V, Cr and Co), 4d (Zr, Nb, Mo, Ru and Pd) and 5d (Ta, W, Re and Ir) transition metal series have been considered as substitutional solutes.

3.2 Lattice parameter of Ni

Typical variation in the energy of the systems, after normalizing by subtracting with the minimum energy corresponding to the equilibrium lattice parameters (a_0), with the lattice parameter is shown in Figure 3.3. Our estimates of the a_0 of pure Ni are 3.52 and 3.51 Å for the ferromagnetic and the non-magnetic states respectively. This is in excellent agreement with the experimental value of 3.52 Å [1].

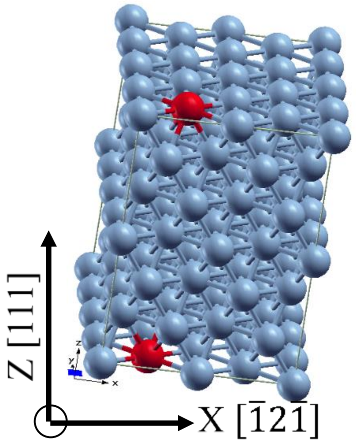

Figure 3.1: 96 atoms supercell of Ni with single solute substitution.

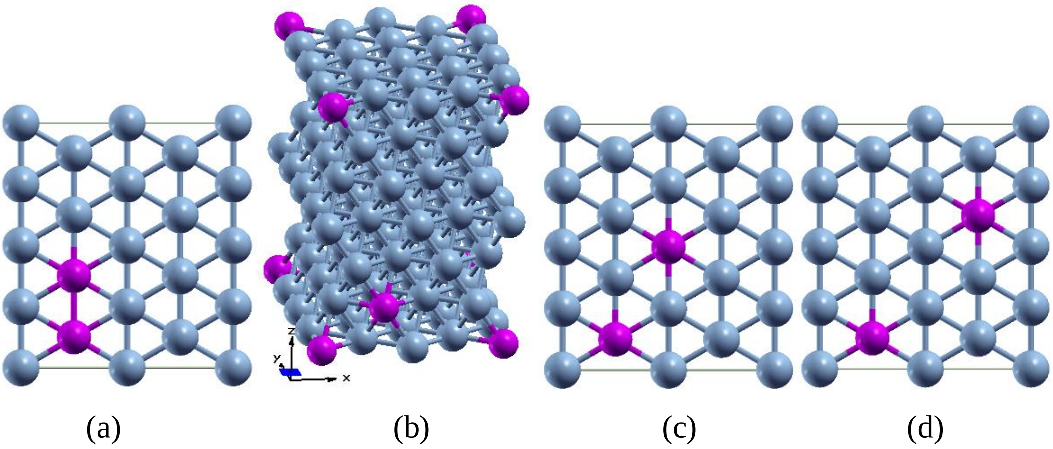

Figure 3.2: Two solutes with 1st to 4th nearest neighbour separation (a)-(d) respectively.

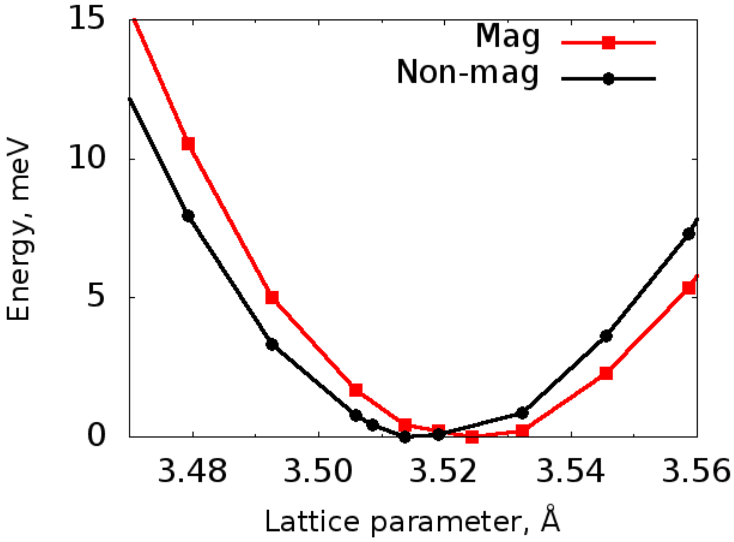

Figure 3.3: Variation of energy as a function of lattice parameter for bulk Ni in magnetic and non-magnetic states. Copyright (2018) by Comp. Mat. Sci [39].

Solute substitution, owing to differences in the atomic size, changes the lattice parameter of the system. Vegard's law describes an approximate empirical rule and states that a linear relation exists between the lattice constant of an alloyed system and the concentrations of the solutes [42,43]. Hence, lattice parameter of alloyed Ni system (a_γ) is given as

$$a_{\gamma} \sim a_{Ni} + \sum_{i} V_{i}^{\gamma} X_{i}^{\gamma}, \qquad 3.2$$

where a_{Ni} is the lattice parameter of pure Ni, V_i^{γ} and X_i^{γ} is the Vegard's coefficients and the atomic fractions of element *i* in Ni. Though empirical relation does not assume ternary and higher order interactions, it is observed to be a quite accurate description. We calculate the coefficients of elements that are most commonly used as alloying elements in Ni-based superalloy. The changes in lattice parameter of the system, for solute concentration variation from 0.7 to 6.7 at.%, are represented in Figure 3.4. Both magnetic and non-magnetic states have been considered here. It is clear that linear relations between the change in lattice parameter with solute concentration, as described by Vegard's relation, is being maintained. Table 3.1 lists the Vegard's coefficients of solutes estimated from the present study as well as reported values from experiments [44 - 46] and first-principles calculations [47]. While our studies suggest that substitution by Co and Cr would lead to contraction of the lattice, experimental results show the other way. This deviation may be attributed to the temperature effect, as the experimental measurements have been done at room temperature while our estimates are at 0K. Deviation in results from the first-principles study by Goswami [47] may be attributed to their smaller system of 32 atom supercell leading to the interaction between the images of the solutes because of periodic boundary condition. To understand the interaction between solutes a bigger supercell of Ni with 144 atoms was considered. Two solutes were substituted with variable spacing (d) between them and the energy of the completely relaxed system was calculated (Table 3.2). It is clearly observed that marginal change in energy is observed in the fourth decimal place for Al as well as Ru when d is greater than 5.56 Å. Therefore, in the present study, whenever two solutes are substituted it is ensured that the spacing between them is higher than 7 Å. Consideration of a bigger supercell (up to 144 atoms) in the present study would potentially minimize these interactions.

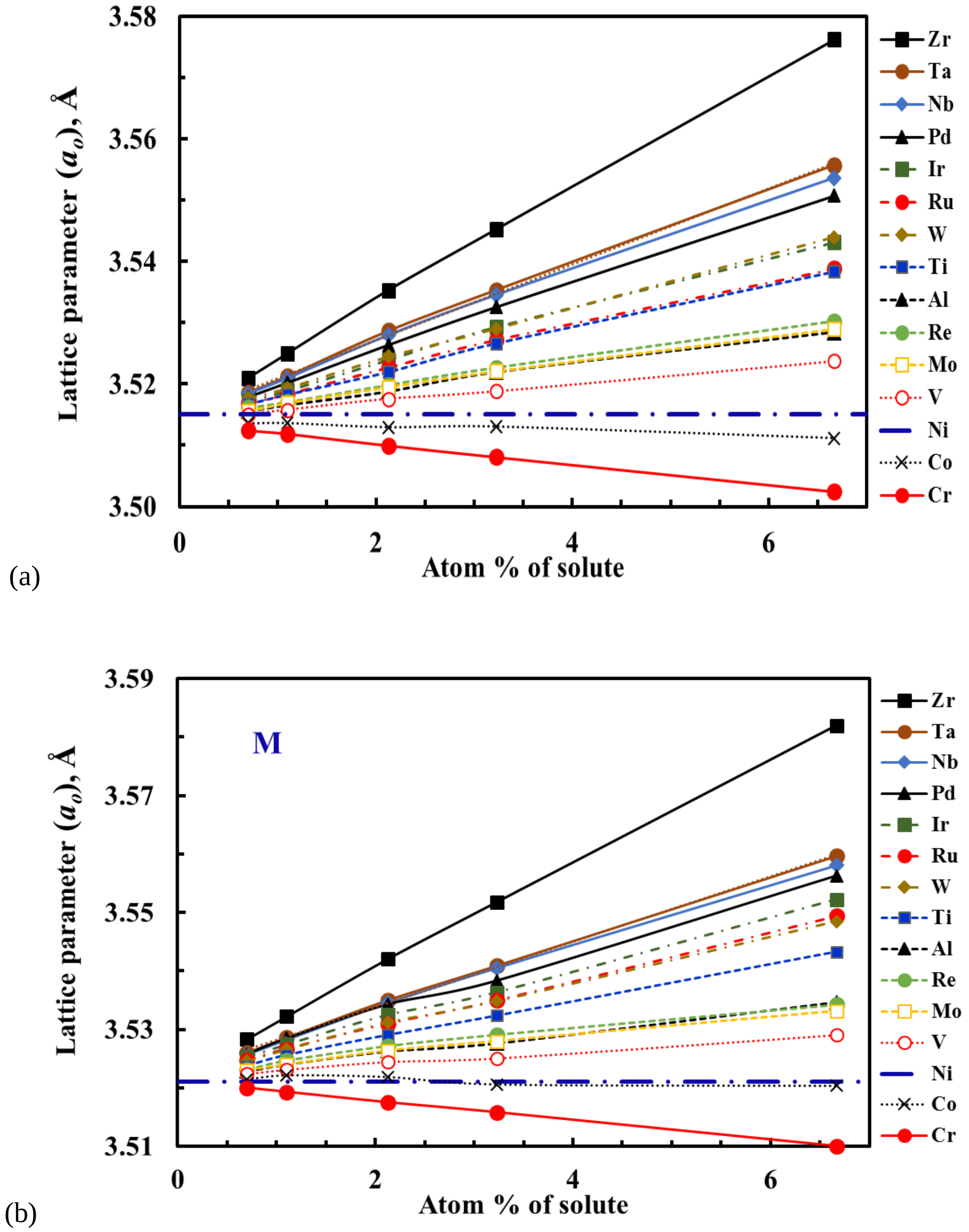

Figure 3.4: Changes in lattice parameter of the system as a function of solute at.% for (a) non-magnetic and (b) ferromagnetic state of Ni.

Table 3.1: Vegard's law coefficients of solutes for lattice constant of alloys with ferromagnetic and non-magnetic states of Ni.

	Present study		**Reported**	
	Ferromagnetic Ni	**Non-mag Ni**	**Experimental**	**First-principles** [47]
Zr	0.90	0.92		
Ta	0.56	0.62	0.7 [44]	
Nb	0.54	0.59	0.7 [44]	0.654
Pd	0.50	0.55		
Ir	0.45	0.44		
Ru	0.40	0.37	0.3125 [46]	0.408
W	0.39	0.44	0.444 [44]	0.443
Ti	0.32	0.36	0.422 [44]	0.38
Al	0.19	0.22	0.179 [44]	0.188
Re	0.18	0.24	0.441 [45]	0.368
Mo	0.17	0.22	0.478 [44]	0.451
V	0.11	0.14		
Co	-0.03	-0.04	0.0196 [44]	
Cr	-0.17	-0.17	0.11 [44]	

Table 3.2: Energy of the relaxed systems with different configurations of solutes.

Spacing between solutes (Å)	Energy (Ry)	
	Al	Ru
2.49	-12205.14570	-12297.05937
3.52	-12205.16417	-12297.06160
4.31	-12205.16504	-12297.06315
5.56	-12205.16660	-12297.06394
6.1	-12205.16657	-12297.06374
6.59	-12205.16660	-12297.06382

3.2.1 Volume change (ΔV) with solute substitution (~1 at.%)

The volume change associated with alloying not only provides solid solution strengthening but also affects the lattice mismatch between γ and γ', which has a bearing on the precipitation strengthening [1]. The fractional change in atomic volume of Ni with alloying by different solutes is presented in Figures 3.5 (a) and (b), for the non-magnetic and ferromagnetic cases, respectively, in terms of number of d-orbital valence electrons of the solutes, in their respective atomic ground states. Except Cr (and Co in the non-magnetic case) all the other solutes increase the volume of the system. The volume change (increase) associated with solute substitution is marginally less for the ferromagnetic Ni than for the non-magnetic Ni. This difference can be attributed to the fact that the lattice parameter of magnetic Ni, itself is roughly 0.3 % higher than the non-magnetic one indicating that magnetic Ni would be able to accommodate larger atoms with lesser strain in the lattice. However, the general variation and trend are quite similar in the two magnetic states of the system. With increase in the number of valence electrons, the percentage change in volume reduces until a valency of 5 (corresponding to half-filled d-orbital) is reached. Beyond this minimum, it increases with further increase in valency.

3.2.2 Volume change (ΔV) with substitution of solutes (~2 at.%)

The volume change associated with solutes substitution for four different configurations wherein the solutes are placed as 1st, 2nd, 3rd and 4th nearest neighbours are considered (Figure 3.2). The corresponding volume changes are shown as tabular form in Table 3.3 and 3.4 for non-magnetic Ni and ferromagnetic state of Ni respectively. In these tables, δ indicates the compensatory volume to be added because of the interactions between the solutes and is computed using

$$\delta = \Delta V_{2X} - 2 \times \Delta V_{1X}, \qquad 3.3$$

where ΔV_{2X} and ΔV_{1X} are volume changes associated with ~ 2 at.% and ~1 at.% solutes respectively. In comparison to ~1 at.% solute substitution, the volume change is not exactly double with ~2 at.% solutes substitution. It is either slightly less or more than two times depending on the spacing and interaction between the solute atoms (Table 3.3 and 3.4). The compensatory volume is maximum positive for Ta in non-magnetic and W in magnetic Ni, when the solutes are 1st nearest neighbour. It is maximum negative with Re as solute atom in the 2nd nearest neighbour position in the magnetic Ni. However, it would be worth looking at whether the solutes prefer to occupy themselves as neighbours which can be accomplished using the concept of binding energy (BE).

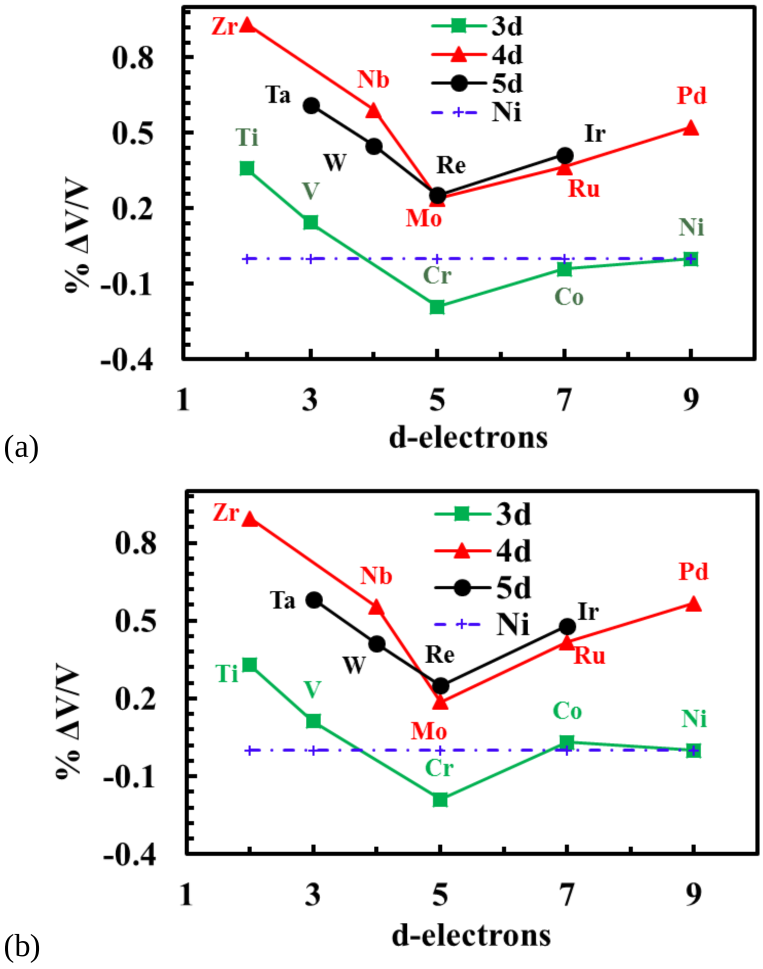

Figure 3.5: Fractional change in volume associated with solute substitution for (a) non-magnetic and (b) ferromagnetic Ni with the number of d-orbital valence electrons of substitutional TM atoms in their respective ground states. The horizontal dotted line at %ΔV/V=0 indicates the base line for pure Ni. Copyright (2018) by Comp. Mat. Sci [39].

Table 3.3: *ΔV* associated with solute substitution for Ni in non-magnetic state.

Atomic No.		**1X**	**2X (1st NN)**		**2X (2nd NN)**		**2X (3rd NN)**		**2X (4th NN)**	
	X	$\%\Delta V_{1X}$	$\%\Delta V_{2X}$	δ	$\%\Delta V_{2X}$	δ	$\%\Delta V_{2X}$	δ	$\%\Delta V_{2X}$	δ
13	Al	0.21	0.42	-0.01	0.39	**-0.03**	0.40	-0.03	0.40	-0.03
22	Ti	0.36	0.74	0.02	0.67	**-0.05**	0.67	**-0.05**	0.67	**-0.05**
23	V	0.14	0.34	**0.05**	0.28	**0.00**	0.29	0.01	0.30	0.01
24	Cr	-0.19	-0.35	0.03	-0.36	0.02	-0.38	**0.00**	-0.35	0.03
27	Co	-0.04	-0.11	-0.03	-0.10	-0.02	-0.10	-0.02	-0.10	-0.02
40	Zr	0.93	1.89	0.02	1.83	-0.03	1.84	-0.02	1.82	**-0.04**
41	Nb	0.59	1.25	**0.07**	1.17	**-0.01**	1.18	0.00	1.19	0.01
42	Mo	0.24	0.49	0.01	0.43	**-0.05**	0.43	**-0.05**	0.46	-0.01
44	Ru	0.36	0.76	0.03	0.71	**-0.02**	0.71	-0.02	0.74	0.01
46	Pd	0.52	1.04	0.00	1.04	-0.01	1.05	0.00	1.05	0.01
73	Ta	0.61	1.32	**0.09**	1.24	**0.01**	1.24	0.02	1.25	0.03
74	W	0.45	0.98	**0.08**	0.86	**-0.03**	0.90	0.00	0.89	-0.01
75	Re	0.25	0.54	0.03	0.45	**-0.05**	0.47	-0.03	0.49	-0.01
77	Ir	0.41	0.87	**0.05**	0.83	**0.00**	0.83	0.00	0.85	0.02

Table 3.4: *ΔV* associated with solute substitution Ni in ferromagnetic state.

Atomic No.		**1X**	**2X (1st NN)**		**2X (2nd NN)**		**2X (3rd NN)**		**2X (4th NN)**	
	X	$\%\Delta V_{1X}$	$\%\Delta V_{2X}$	δ	$\%\Delta V_{2X}$	δ	$\%\Delta V_{2X}$	δ	$\%\Delta V_{2X}$	δ
13	Al	0.19	0.41	0.03	0.37	-0.01	0.38	0.00	0.38	0.00
22	Ti	0.33	0.69	0.03	0.63	-0.03	0.62	-0.04	0.62	-0.04
23	V	0.11	0.29	**0.07**	0.22	-0.01	0.20	-0.03	0.23	0.00
24	Cr	-0.19	-0.38	0.00	-0.25	0.00	-0.40	-0.02	-0.40	-0.02
27	Co	0.03	0.00	-0.06	0.00	-0.06	0.01	-0.05	0.01	-0.05
40	Zr	0.89	1.81	0.02	1.76	-0.03	1.76	-0.03	1.74	-0.05
41	Nb	0.55	1.16	0.05	1.08	**-0.03**	1.09	-0.02	1.09	-0.02
42	Mo	0.19	0.41	0.04	0.37	**-0.01**	0.37	0.00	0.39	0.02
44	Ru	0.42	0.80	-0.03	0.80	-0.03	0.79	-0.04	0.79	-0.04
46	Pd	0.57	1.08	-0.06	1.06	-0.08	1.06	-0.07	1.07	-0.07
73	Ta	0.58	1.22	**0.05**	1.12	**-0.05**	1.12	-0.04	1.14	-0.02
74	W	0.41	0.91	**0.08**	0.80	-0.02	0.79	**-0.03**	0.81	-0.01
75	Re	0.25	0.52	0.02	0.39	**-0.11**	0.42	-0.08	0.46	-0.04
77	Ir	0.48	0.92	-0.04	0.92	-0.04	0.89	**-0.07**	0.92	-0.05

3.3 Binding energy (BE)

In order to describe what nearest neighbour bonds an atom prefers and hence correlate with their preference towards forming clusters, we have calculated the BE. BE describes the preference towards neighbouring bonds for an atom [41]. The BE between two solute atoms (X) in a system with N lattice sites, $E_{bind}(X-X)$, in the host lattice of Ni atoms is given by

$$E_{bind}(X-X) = 2.E(Ni_{N-1}X_1) - E(Ni_{N-2}X_2) - E(Ni_N), \qquad 3.4$$

where $E(Ni_{N-1}X_1)$ and $E(Ni_{N-2}X_2)$ are the total energies of the supercell with one and two X atoms respectively in the desired configuration and $E(Ni_N)$ is the total energy of a perfect supercell consisting of only Ni atoms. The tendency of the alloying elements to form a cluster is based on the magnitude of the BE of the system. A negative BE indicates repulsive force between the two solute atoms. The first term in the RHS of equation 3.4 describes energy of a system wherein the solutes are essentially infinitely separated. Since, we work with finite systems (96 atoms), the separation in the present case corresponds to sixth nearest neighbour due to periodic boundary conditions (based on the interaction analysis in section 3.2. This can be considered as a good approximation for simulating infinite separation as generally the influence of one solute is not expected to be felt for such separation in a real system [48].

In the present chapter BE with different solute atoms have been calculated for four different configurations (Figure 3.2) with and without spin-polarization for Ni (Table 3.5). In the non-magnetic case, Co has a positive BE with another Co at the first nearest neighbour configuration indicating its preference to form cluster (marked as bold in the table) whereas other elements do not show clustering behavior. In fact, in the magnetic case too, Co has zero BE for 1st and 2nd neighbour configurations indicating its relative insensitiveness for the presence of other Co atom. Irrespective of the magnetic state of Ni, except for Co and to some extent Ru and Pd, BE is maximum (negative) for 1st NN configuration and hence suggesting maximum repulsion for this configuration. Repulsive energy is substantially reduced with increasing separation between the solutes.

Table 3.5: Binding energy associated with solute substitution in Ni. The configuration with highest BE is marked bold.

	Non- magnetic				Magnetic			
	BE_{1NN}	BE_{2NN}	BE_{3NN}	BE_{4NN}	BE_{1NN}	BE_{2NN}	BE_{3NN}	BE_{4NN}
Al	-0.28	-0.03	-0.02	**0.01**	-0.22	0.01	0.00	0.05
Ti	-0.46	**0.00**	-0.02	-0.05	-0.37	**0.12**	0.02	0.02
V	-0.37	**-0.01**	-0.03	-0.13	-0.23	**0.16**	0.03	-0.05
Cr	-0.24	**-0.02**	-0.03	-0.17	0.10	**0.31**	0.32	0.32
Co	**0.03**	0.00	0.00	-0.01	0.00	0.00		-0.03
Zr	-0.67	**0.10**	0.01	-0.03	-0.59	**0.22**	0.05	0.05
Nb	-0.64	**0.04**	0.00	-0.13	-0.48	**0.24**	0.07	-0.03
Mo	-0.57	**-0.02**	-0.04	-0.24	-0.24	**0.24**	0.06	-0.12
Ru	-0.06	-0.03	**-0.01**	-0.10	0.00	-0.04	**0.04**	-0.05
Pd	-0.01	**0.05**	0.00	-0.03	-0.01	**0.05**	-0.01	-0.03
Ta	-0.69 (-0.68*)	**0.05** **(0.06*)**	-0.01 (-0.01*)	-0.12 (-0.03*)	-0.52	**0.24**	0.06	-0.02
W	-0.62 (-0.60*)	**-0.02** **(-0.01*)**	-0.02 (-0.29*)	-0.21 (-0.07*)	-0.33	**0.27**	0.09	-0.07
Re	-0.45 (-0.43*)	-0.09 (-0.09*)	**-0.05** **(-0.05*)**	-0.27 (-0.11*)	0.05	**0.20**	0.07	-0.10
Ir	-0.11	-0.05	**-0.01**	-0.04	-0.07	-0.06	0.03	-0.02

* A. Mottura *et al.* [49]

In both magnetic as well as non-magnetic cases, Zr, Nb, Pd and Ta show preference to have 2nd neighbour coordination whereas Al shows preference for 4th neighbour coordination. In addition, elements such as Ti, V, Mo, W and Re show preference for 2nd and Cr, Ru and Ir show preference for 3rd neighbour coordination in the magnetic state, whereas in the non-magnetic state they tend to stay far apart. Mottura *et al.* [49] have reported little effect of magnetism on the BE, however we observe that there is an appreciable change in the BE for some solutes with the state of Ni atom. The values reported by Mottura *et al.* [49] for the non-magnetic Ni are in very good agreement with our calculation for Ta, W and Re. While for other elements, the magnitudes vary with the state of magnetization, for Cr and Re there is a complete reversal from repulsive to attractive force between the solutes.

3.4 Conclusion

Lattice parameter change associated with solute substitution follow linear relationship and hence Vegard's law can be considered to be applicable for finding the variation of the lattice parameter with their concentration. The coefficients estimated in the present study are in agreement with the experimentally reported [44 - 46] as well as other first-principles calculation [47]. With these coefficients we can find the variation of lattice expansion/contraction with the composition of solute element and estimate the lattice parameter as a function of alloy composition (equation 3.2). Such a relation has practical significance though it would be based on the assumption that Vegard's law is applicable and that there is no cross-correlation effect due to different solutes, which needs further verification. It is known that the lattice misfit between the γ and γ' phases affects the coherency between the phases and hence the extent of precipitation hardening. Ni and Ni_3Al are considered as prototypes for the γ and γ' phases and a relation for estimating the lattice parameter of γ' phase can also be obtained by substitution of alloying elements in Ni_3Al. Using such relations along with the partitioning information of alloying elements from other calculations (say thermodynamic calculations), the optimal compositions can be arrived at while designing a new alloy (so as to keep the coherency strain at a minimum level). Further, from the estimated lattice misfit, it would be possible to calculate the strain energy using micromechanics principles. Therefore, the extent of precipitation hardening can be estimated if the elastic moduli are known/computed. The strain energy can also serve as useful input for mesoscale simulations such as phase field simulations and hence realistic microstructural evolution can also be simulated. BE associated with the relative positioning between the solutes predict their preference of the neighbouring bonds with positive value associated with attraction. On this basis except Co no other solutes prefer clustering. Repulsive energy is substantially reduced with increasing separation between the solutes.

Chapter 4

Influence of Dilute Solute Substitution in Ni on Generalized Stacking Fault Energies*

The crystal structure of Ni, being face center cubic (FCC), makes it inherently ductile as it fulfills the von Mises (1928) criteria of having the necessary five independent active slip systems. Slip system describes the set of symmetrically identical slip planes and the associated family of slip directions for which dislocation motion can easily occur leading to plastic deformation. An independent slip system is defined as one producing a crystal shape change that cannot be reproduced by any combination of other slip systems. FCC crystal has 12 possible slip systems ({111} <110>, out of which five are independent) and hence the movement of dislocation, causing plastic deformation, is very much favorable leading to higher ductility as compared to other crystal structures.

4.1 Dislocation

The importance of understanding dislocations and their interaction is vital for improving the material's behavior under stress. The permanent deformation which materials retain even after the removal of external loading is achieved through slip, a technical term referring to plastic deformation caused by dislocations. Plastic

---

* This work has been published in part in Comp. Mat. Sci [39]. Copyright (2018).

deformation by shear can be visualized as a plane of atoms sliding past another plane (Figure 4.1). This movement requires a stress, τ_m, which is proportional to the shear modulus (*G*) and is given by $\tau_m \approx {G}/{2\pi}$, is of the order of GPa. However, the crystals typically yield at stress levels of the order of 300 MPa. Taylor, Orowan and Polyani independently postulated in 1930s and later got confirmed by another TEM observations in 1950s, that the agent responsible for this weakening is the presence of a crystallographic defect caused by irregularity within the crystals called dislocation.

4.1.1 Slip by dislocation glide

Glide of many dislocations, in single crystals, leads to slip which is manifested as weakening of the system leading to plastic deformation at much lower load than predicted by theoretical calculation for perfect materials. Glide requires relatively little atomic motion compared to full shifting of the perfect (i.e., defect free) crystals. Hence the stress to move a dislocation is much smaller (at least 100 times), as only few bonds are to be broken at any instant. In 1940 Peierls [50] defined a concept, later refined by others [51 - 53], that for individual dislocation movement, a lattice frictional force called Peierls-Nabarro force must be overcome. This force depends on the force-distance relation between atoms. If the dislocation has to move, for example an edge dislocation represented with red colored sheet of atoms (Figure 4.2), it has to press against the neighbouring atoms on one side and move away from the atoms on the other side by passing through a higher energy configuration. Peierls and Nabarro arrived at the energy ($E_{P\text{-}N}$) of the dislocation per unit length as a function of dislocation movement (Figure 4.2, also referred as Peierls potential).

$$E_{P-N} = \frac{G|\vec{b}|^2}{\pi(1-\nu)} exp\left(\frac{-2\pi W}{|\vec{b}|}\right), \qquad 4.1$$

where *W* is the width of the dislocation. The Peierls-Nabarro stress is the shear stress required to move an individual dislocation on its slip plane and is given as

$$\tau_{P-N} = \frac{2\pi}{|\vec{b}|^2} E_{P-N} \approx \frac{2G}{(1-\nu)} exp\left(\frac{-2\pi d}{(1-\nu)|\vec{b}|}\right), \qquad 4.2$$

where d is the distance between slip planes and Burgers vector $\vec{b}$ is distance between the nearest neighbouring atoms along the slip direction. Hence slip is most preferred on planes with highest planar density (maximum d i.e. {111} for FCC) and direction along highest linear density (i.e. <110> minimum $\vec{b}$). However, the movement of dislocation in FCC materials is favored with the dissociation of perfect dislocation to partials due to energy considerations.

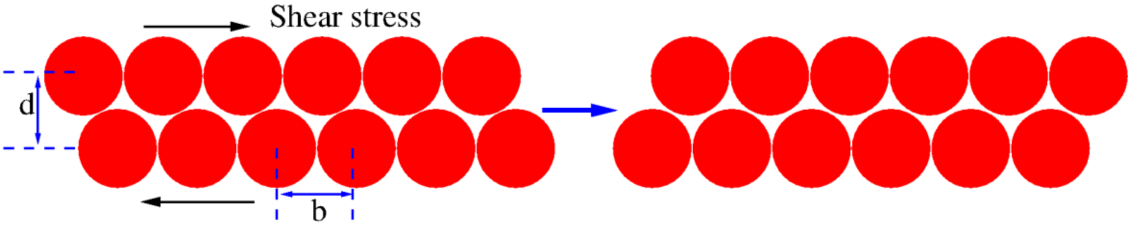

Figure 4.1: Shearing of one plane over the other on the application of stress leading to plastic deformation.

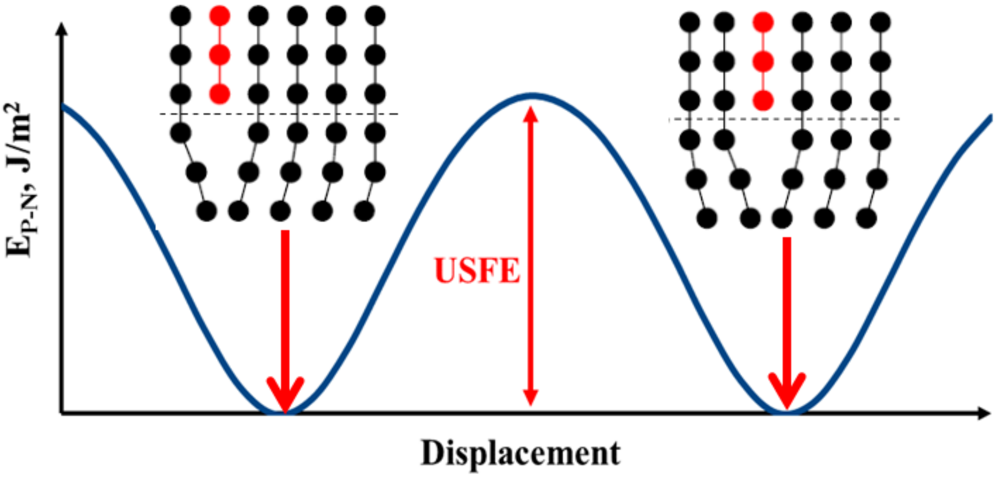

Figure 4.2: Peierls-Nabarro energy as a function of dislocation movement from one plane to another (marked with atoms in red color).

4.1.2 Dislocation dissociation

Glide of a dislocation, in FCC crystals, by 1/2<110> (the shortest translation vector known as Burgers vector, $\vec{b}$) leaves behind a perfect lattice and therefore the dislocation is called a perfect dislocation [54]. However, it is also well known that the dislocation movement is favored when the perfect dislocation $\vec{b}$, dissociates into Shockley partials, $\overrightarrow{b_1}$ and $\overrightarrow{b_2}$ as

$$\frac{1}{2}[\bar{1}10] \rightarrow \frac{1}{6}[\bar{2}11] + \frac{1}{6}[\bar{1}2\bar{1}] + SF, \qquad 4.3$$

where SF, the stacking fault, is the region encompassing the partial dislocations (Figure 4.3). The driving force for this dislocation dissociation is the minimization of the total energy of the system. Energy of a dislocation is proportional to $\left|\vec{b}\right|^2$ and according to Frank [54] the dissociation is favorable only if $\left|\vec{b}\right|^2 > \left|\vec{b}_1\right|^2 + \left|\vec{b}_2\right|^2$. Frank only considered energy associated with the dislocation, however increase in energy on account of the stacking faults has also to be considered. Thus, it is the overall energy of the crystal that should decrease to favor the dissociation. It is important to note that dislocation splits into Shockley partials which are still able to glide on the same plane as the perfect dislocation, wherein the leading partial creates a stacking fault while trailing one eliminates it.

Hence the movement of dislocation is governed by firstly the generation of stacking fault and the fault energy associated with it and secondly overcoming the energy barrier, also known as Peierls potential, required to move the dislocation. The Peierls potential is greatly reduced in the case of partials compared to that of a perfect dislocation. For example, the energy barrier for the dislocation to move along <211> and <110> are reported to be 254 mJ/m^2 and 777 mJ/m^2 by Yu and Wang [55] for Ni_3Al. Estimation of these two parameters and their response to different solutes and their composition will be essential to design materials with desired property.

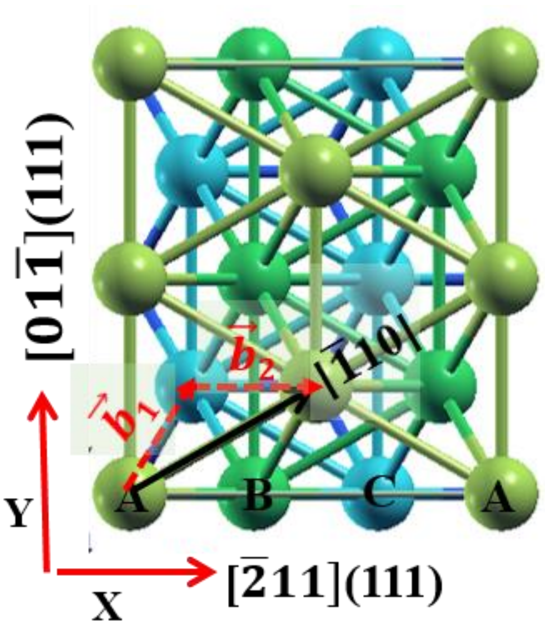

Figure 4.3: Schematic two-dimensional presentation of {111} plane with different color of atoms representing the stacking sequence of FCC and dissociation of Burgers vector of a perfect dislocation $\vec{b} = {}^{1}/_{2}\,[\bar{1}10]$ into two Shockley partials $\overrightarrow{b_1} = {}^{1}/_{6}\,[\bar{1}2\bar{1}]$ and $\overrightarrow{b_2} = {}^{1}/_{6}\,[\bar{2}11]$. Copyright (2018) by Comp. Mat. Sci [39].

4.1.3 Stacking fault

A stacking fault (SF) is a planar defect in a crystal, representing an interruption in the perfect stacking sequence of the atomic layers. The normal (111) stacking sequence with minimum energy for FCC crystals is …ABCABCABC... Any local disturbances to this sequence generates a region with fault in the stacking patterns and hence increases the energy. The associated energy cost due to the presence of this planar fault is known as the stacking fault energy (SFE).

In FCC crystals the most common stacking fault is the intrinsic stacking fault (ISF) and is generated because of the shearing of the lattice by ${}^{1}/_{6}\,[\bar{2}11]$. This movement changes the stacking sequence of the FCC lattice from ….ABCA**BCAB**CABCABC…. to ….ABCA**BCBC**ABCABCA….. generating an ISF with one mirror plane with energy penalty known as intrinsic stacking fault energy (ISFE, γ_{is}).

The spacing between the partial dislocations is an important parameter governing the cross slip i.e. the ability of dislocations to glide on the intersecting slip planes and hence is directly correlated with the strengthening of the materials. While a perfect dislocation can easily move from one plane to another, the movement of partials has to be coordinated and is dependent on the spacing between them [54]. Spacing between partials is an interplay of balance between

1. Repulsive force acting between the two partial dislocations
2. Attractive force due to energy cost of generating stacking fault

It is well established that the faulted region between the partials is an intrinsic stacking fault and its energy, γ_{is}, is inversely related to the spacing between the partials, d (γ_{is} α 1/d) [54]. Lower γ_{is} (wider spacing between the partials) retards the possibility of cross slip and reduces the steady-state creep rate $\dot{\varepsilon}$ with a widely used empirical relation [56, 57],

$$\dot{\varepsilon} \approx \Gamma_{\mathrm{SF}}^{\mathrm{n}}. \qquad 4.4$$

Here, $\Gamma_{\mathrm{SF}} \left(= {}^{\gamma_{is}}\!/_{G|\vec{b}|} \right)$ is the normalized SFE, with G being the shear modulus and $\vec{b}$ the burgers vectors, and n is an empirical parameter around 3-4 [58]. Cross-slip can be reduced by alloying with elements that lower the SFE of Ni resulting in wider stacking faults [59].

4.1.4 Estimation of stacking fault energies

There is no direct way of measuring the SFE, and hence several indirect experimental methods have been used to determine it. The most widely used method is the back calculation of SFE by measuring the spacing between the partials observed in the transmission electron microscopy (TEM). For example Reed and Schramm [60] report average value of SFE for Ni to be 220 mJ/m^2 and in the range of 160 – 300 mJ/m^2. However, the wide range for SFE for Ni emphasizes that experimental determination of

SFE is quite complicated due to various parameters (grain size, homogeneity, impurity etc,) involved including the sample quality and the accuracy with which the width of the partials can be determined. The difficulty level would further be exacerbated for accurate measurement of the SFE as a function of composition. A systematic study based on the theoretical methods would lead to a fundamental understanding of the topic, which is of great importance for designing new materials.

Numerous studies, theoretical as well as experimental, have been carried out to gain better understanding of the effects of solute substitution on various properties, such as lattice parameter, SFE and USFE of Ni. For example, Siegel [61] calculated the GSF of Ni alloyed with Nb, W, Mn, Fe and Cu and evaluated a measure of twinnability of the above alloys. Datta *et al*. addressed the surface effects on the stacking fault by analysing nanofilms of Al, Cu and Ni [62]. Shang *et al*. explored the effects of alloying elements on the SFE of dilute Ni-base superalloys and their temperature dependence [63]. Mishin [64] carried out comprehensive study on the atomistic modeling of pure γ and γ' phases using molecular dynamics. However, to the best of our knowledge, a systematic study of effect of alloying on the γ_{is} and γ_{us} of Ni is lacking. In this work an attempt has been made to gain an understanding of the effect of substitutional solute (~1 at.% and ~2 at.%) elements belonging to 3d, 4d and 5d transition metals substituted for Ni on the above mentioned properties using first-principles based DFT. For the first time, particular emphasis has been given to the spacing between the solutes and its effect on the above mentioned properties. A comprehensive study has been carried out by considering nickel in both ferromagnetic (spin-polarized) and non-magnetic (non-spin-polarized) states.

4.2 Computational details

A supercell was constructed with three orthogonal directions along $[\bar{1}01]$, $[\bar{1}2\bar{1}]$ and [111] direction having six (111) layers (i.e., with the stacking sequence ABCABC along the <111> corresponding to close-packed FCC structure). This system with 96 Ni-atoms (consisting of 16 atoms in each layer) was completely relaxed, with the flexibility to change its cell size also, to obtain the equilibrium volume corresponding to the minimum energy structure. In order to calculate the fault energies, shear deformation along <112>{111} is simulated by suitably displacing the image of the supercell along the $[\bar{2}11]$ direction, and allowing the positions of the atoms in the outer planes to relax along directions only perpendicular to the fault plane. The corresponding energy penalty γ_{fs} is estimated as

$$\gamma_{fs} = \frac{E_f - E_o}{A}, \tag{4.5}$$

where E_f and E_o are the energies of the faulted and perfect structures, and A is the area of the slip plane in the supercell on which fault has been generated.

In order to find out the effect of the solutes on the energy penalty, two different configurations have been considered. For the first case, one of the Ni atom on the shearing plane while in the second case two Ni atoms were substituted with an alloying element from the 3d, 4d and 5d transition element series and the procedure of calculating equilibrium volume and the defect energies was repeated for each substitution. With two solute atoms, again three different configurations have been considered while substituting Ni, namely first, third and fourth nearest neighbour as 1NN, 3NN and 4NN on the same (111) plane (Figure 3.2). 2NN have not been considered for estimation of the stacking fault as the two alloying elements will have to be on two different (111) planes and hence comparison of the properties may be difficult.

4.3 Estimation of fault vectors from GSF energy surface

1D representation of the gamma surface gives us the energy required to slide one half of the crystal against another along a specific direction (here $[1\bar{1}0]$ and $[\bar{2}11]$) on any specific plane (here octahedral (111) for Ni) and is represented in Figure 4.4. The minima and maxima in energy represents the stable and unstable stacking fault configurations. This minimum energy known as stable stacking fault is the intrinsic stacking fault energy (γ_{is}), and maximum with the $E_{P\text{-}N}$ corresponding to the energy barrier for dislocation to move from one minima to another for Ni. It is important to note that translation of dislocation by ${}^{1}\!/_{2}\,[1\bar{1}0]$ on (111) (point 1 to 3 for Figure 4.4a) leaves the crystal unchanged and hence there should be no energy difference. Hence, no stacking fault is generated if dislocation movement is along <110>. Here, the movement of ${}^{1}\!/_{2}\,[1\bar{1}0]$ corresponds to movement of perfect dislocation by $\vec{b}$. However, to undergo this slip it has to cross the energy barrier of point 2 which is estimated to be 711 mJ/m^2 for pure Ni in the present study

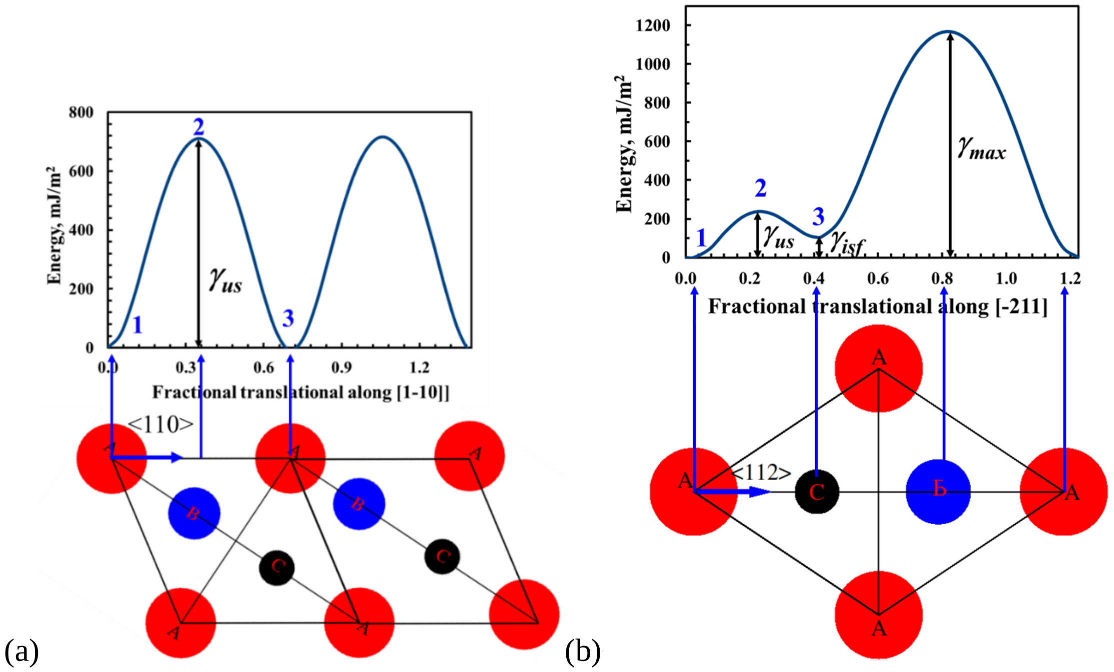

Figure 4.4: Energy profile of sliding one half of the Ni supercell against another along (a) $[1\bar{1}0]$ and (b) $[\bar{2}11]$ on (111).

However, when similar analysis is performed along <112> a local minima at point 3 (point 1 to 3 for Figure 4.4b) is obtained corresponding to a translation of Burgers vector $\overrightarrow{b_p} = {}^{1}\!/_{6}\,[\bar{2}11]$, resulting in the generation of an γ_{is}. Point 2 of Figure 4.4b corresponds to the energy barrier for dislocation to move to the stacking fault configuration and after a series of refined calculations, the first maximum of the GSFE was found at the slip corresponding to the translation of 0.56 $\overrightarrow{b_p}$ (Appendix A). The lowest energy barriers among the family of various paths on a given plane (in the present case {111}) is obtained for translation along $\langle 11\bar{2}\rangle$ and hence is defined as the USFE (γ_{us}) and estimated to be 237 mJ/m^2. Hence, it is clear that the dissociation of dislocation into partials reduces the energy required for movement of dislocation from 711 mJ/m^2 along <110> to 237 mJ/m^2 along <112> (~almost 1/3).

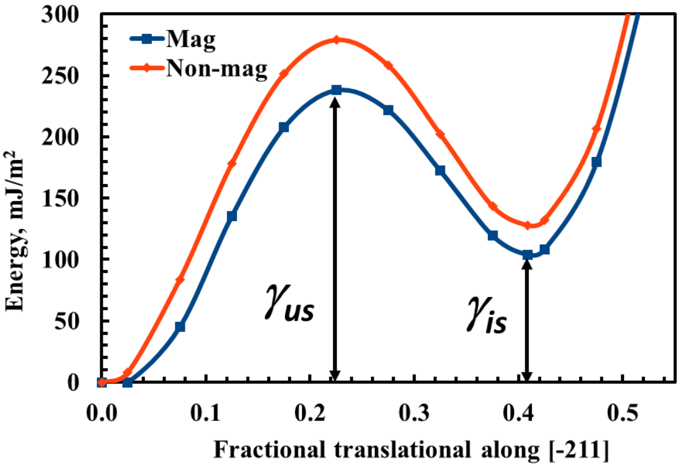

Figure 4.5: Energy cost associated with slip along $[\bar{2}11]$ for non-magnetic and ferromagnetic Ni

4.4 Results

4.4.1 Intrinsic stacking fault energy (γ_{is}) of bulk Ni

Figure 4.5 plots the energy associated with sliding one half of the crystal against the other along $[11\bar{2}]$ for ferromagnetic and non-magnetic state of Ni. The maximum and minimum are the γ_{us} and γ_{is}. γ_{is} for magnetic Ni is estimated to be 128 mJ/m^2 which is in very good agreement with other simulated values such as (121 [23], 132 [63] mJ/m^2, 134 [64], 125 [65]). γ_{is} for non-magnetic Ni is estimated to be 104 which is 24% lower in comparison to the magnetic state. Hence magnetic state of Ni has pronounced effect on the γ_{is} and hence the spin polarization cannot be neglected in its estimation. This result has other ramification that at service temperatures, which are often higher than the Curie temperature of Ni (355°C), the stacking fault energy of pure non-magnetic system is lower than that of the low temperature ferromagnetic system (with the disclaimer that presently computed energies are at zero K) which is beneficial for mechanical properties.

4.4.2 γ_{is} with solute substitution

Substitution of solutes to the system is bound to have an effect on the γ_{is}. The variation in γ_{is} for the solute (~1 at.%) substituted systems is shown in Figure 4.6 as a function of the d-orbital valence electrons of the solutes (ground state valence of pure solutes). All solutes, except Pd (in the non-magnetic case), lowers the γ_{is} of Ni up to a maximum of 15%, with Ti, V, Nb, Mo, Ru, Ta, W and Re decreasing it by more than 10%. These results support the fact that Nb, Re, Ru, Ta, Ti and W are added to improve the creep resistance of Ni-based single crystal alloy [66], because of their lower stacking fault energies (equation 4.4). While the substitution by 3d series elements leads to almost a monotonic increase in γ_{is} as a function of valence electrons, those by 4d and 5d series show a different behavior, in which a maximum reduction of up to 15% is observed for solutes having d-valency of 4 (Nb for 4d and W for 5d) and 5 (Re for 5d and Mo for 4d) depending on the magnetic state of Ni.

Table 4.1 summarises of the effect of substituting ~1 at.% as well as ~2 at.% solute atoms from the 3d, 4d and 5d series of transition metals on γ_{is} of dilute solid solution of Ni. Our calculated γ_{is} for ~1 at.% solute substitution, in ferromagnetic Ni, is in very good agreement with Shang *et al.* [63]. With ~2 at.% substitution, except for Al, Co in non-magnetic state and Pd, the γ_{is} decreases further in excess of 20% compared to pure Ni. For most of solutes, except for Al, Cr, Co, Zr, Pd and Ir, % decrease in γ_{is} compared to that of pure Ni are more than doubled with doubling the solute concentration. For example ~1 at.% Re substitution decreases γ_{is} of Ni by 13 % while ~2 at.% Re atoms decrease it by 30 % in the non-magnetic system.

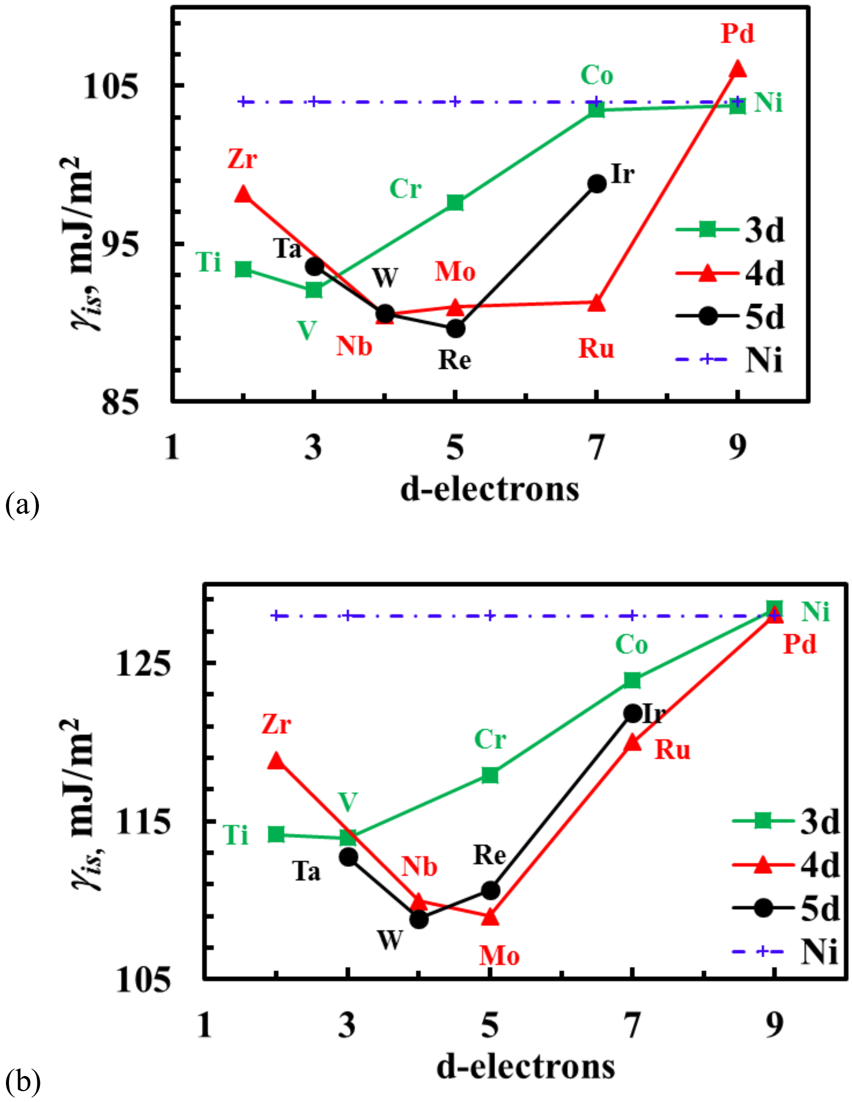

Figure 4.6: Variation in γ_{is} of Ni with solute substitution with respect to their number of d-valence electrons in (a) non-magnetic and (b) magnetic states. The dotted lines indicate the γ_{is} of pure Ni. Copyright (2018) by Comp. Mat. Sci [39].

Table 4.1: ISFE of Ni alloy associated with solute substitution.

Intrinsic stacking fault energy (mJ/m^2)									
	Non- magnetic				**Magnetic**				
	~1 at.%	**~2 at.%**			**~1 at.%**		**~2 at.%**		
Ni-X	**1X**	**1NN**	**3NN**	**4NN**	**1X**	**Reported**	**1NN**	**3NN**	**4NN**
Pure	104	104	104	104	128	121 [23], 134 [64], 137 [67] , 125 [65], 132 [63]	128	128	128
Al	102	101	101	103	124	124 [63]	117	117	119
Ti	93	83	81	84	114	113 [63]	100	98	102
V	92	83	80	81	114	113 [63]	99	97	97
Cr	98	91	92	92	118	119 [63]	100	123	127
Co	103	104	104	103	124	127 [63]	120	119	119
Zr	98	87	89	98	119	102 [63]	104	107	116
Nb	90	76	74	78	110	59 [61], 104 [63]	90	89	93
Mo	91	74	75	75	109	109	85	83	83
Ru	91	82	81	76	120	116 [63]	112	113	113
Pd	106	104	107	107	128	127 [63]	124	127	128
Ta	94	82	80	84	113	108 [63]	97	95	99
W	91	76	75	75	109	38 [61], 105 [63]	90	87	88
Re	90	73	75	71	111	103 [63]	93	89	86
Ir	99	95	95	90	122	122	119	117	115

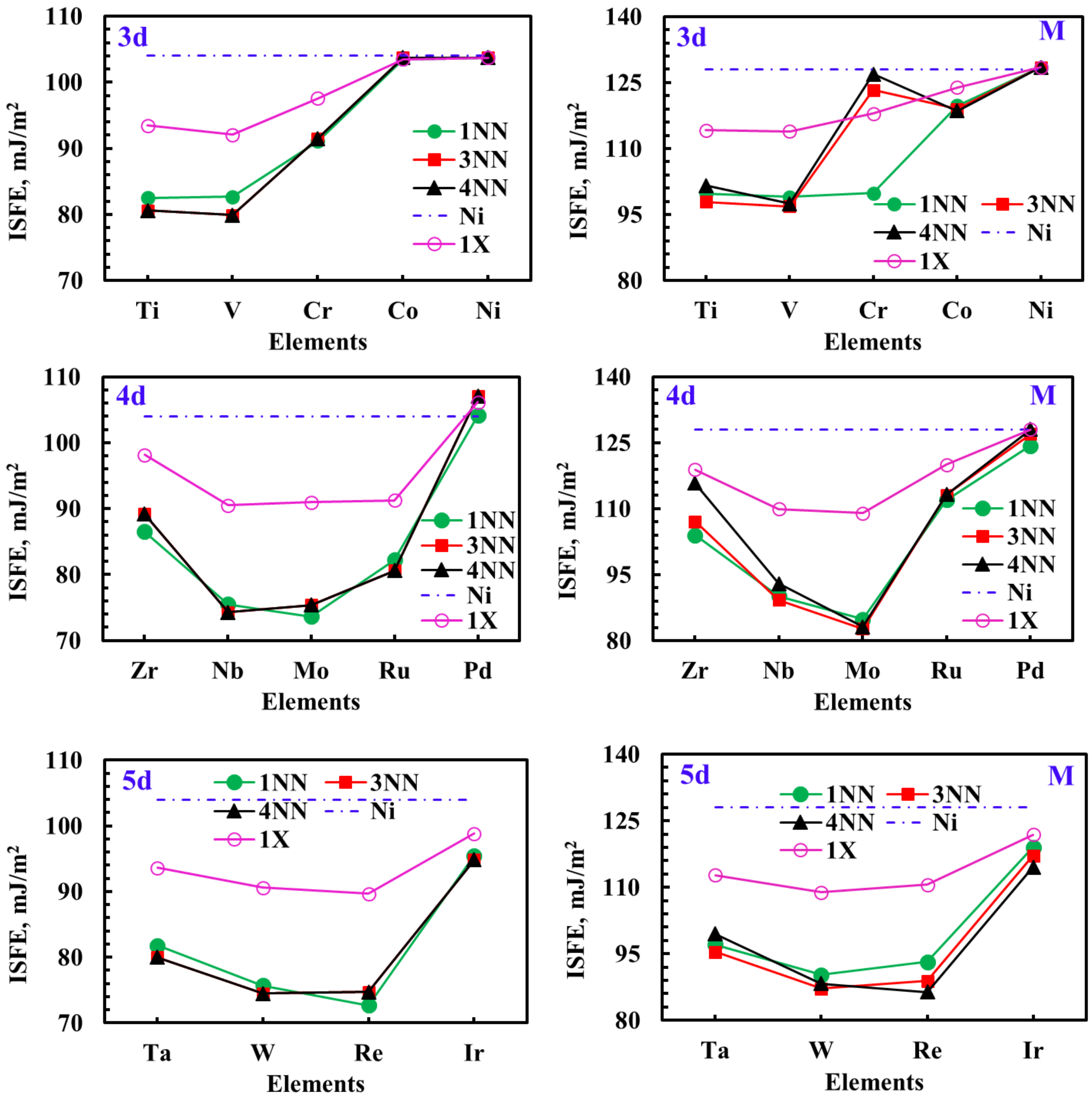

(a) (b)

Figure 4.7: Dependence of ISFE (γ_{is}) for TM substituted Ni on the relative spacing between solute atoms in (a) non-magnetic and (b) ferromagnetic state of Ni.

The variation of γ_{is} for various elemental substitutions for different configurations are presented in terms of transition metal series-wise in Figure 4.7. It may be observed that the γ_{is} is sensitive to the spacing between the solutes for some of the elements. For example in the non-magnetic system with Zr at 1NN configuration the decrease in γ_{is} (compared to that of pure Ni) is 16% which becomes 14% and 6% for 3NN and 4NN configurations, respectively. When the magnetization is turned on, the reduction in γ_{is} is 19%, 16% and 9%, respectively for the 1NN, 3NN and 4NN configurations. It is very interesting to note that when the substitution of Cr is doubled, in the non-magnetic case the decrease in ISFE is doubled irrespective of the spacing between the Cr atoms. However, when the calculations are performed with spin-polarization, the reduction in ISFE is 22% and 4% for the 1NN and 3NN configurations respectively, while for the 4NN configuration, the ISFE is almost equal to that of pure Ni. In other words, whatever reduction of fault energy achieved by substituting ~1 at.% Cr atom can be nullified if its concentration is increased and keeping the atoms far apart. This result is quite counter-intuitive.

4.4.3 Unstable stacking fault energy (γ_{us})

From our calculations (Figure 4.5) we estimate γ_{us} for non-magnetic Ni to be 237 mJ/m^2 which is in very good agreement with another DFT calculation of 230 mJ/m^2 [23]. Our estimation of 281 mJ/m^2 for ferromagnetic Ni also compares very well with other reported values of 281 mJ/m^2 [68], 273 mJ/m^2 [61] and 298 mJ/m^2 [64]. Similar to γ_{is}, the γ_{us} for the magnetic state of Ni is about 19 % higher than that of the non-magnetic Ni. Hence it can be concluded that magnetic state of Ni also has a significant influence on the γ_{us} and hence on the Peierls stress of the system. The USFE for (100) surface is very high (1080 mJ/m^2 and 1120 mJ/m^2) for the non-magnetic and magnetic system [48]. This calculation provides a quantitative picture for the absence of dislocations on the cubic planes of FCC.

4.4.4 γ_{us} with solute substitution

γ_{us} can be affected because of the presence of solutes in Ni-based solid solution and different solutes may influence it differently. Table 4.2 summerises this influence on γ_{us} when solutes concentration and the spacing between the solutes are varied. Figure 4.8 graphically represents the variation of γ_{us} with solute substituted (~1 at.%) in Ni. With solute substitution, γ_{us} is 10-20 % higher for the magnetic Ni compared to its non-magnetic counterpart. In the non-magnetic case, Zr, Nb and Pd decrease γ_{us}, whereas in the magnetic case, except Cr, Co, Ru and Ir all the other substitutions considered here reduce the fault energy. For solute substitution using 3d, 4d and 5d series of transition metals maximum increases in γ_{us} results from solutes having half-filled d-valence electrons i.e. Cr, Re and Mo respectively for the non-magnetic Ni system.

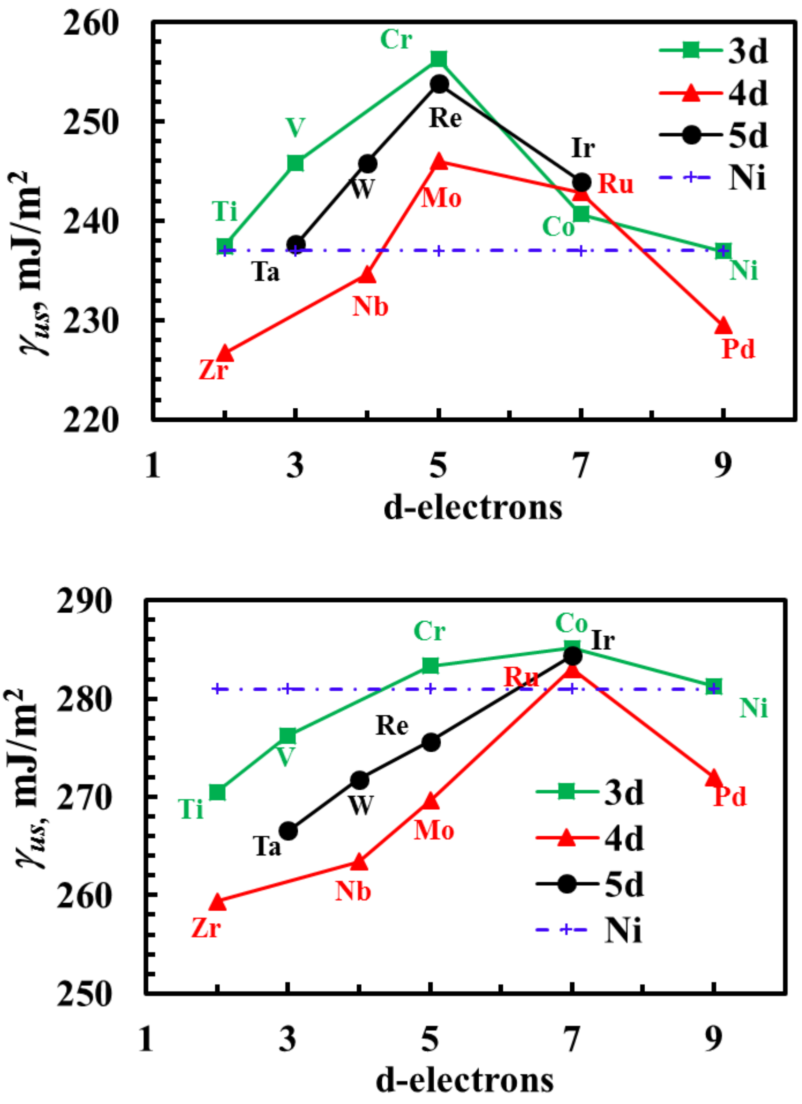

(a)

(b)

Figure 4.8: Variation in γ_{us} of Ni in (a) non-magnetic and (b) ferromagnetic state with solute substitution (~1 at.%) as a function of their number of valence electrons. γ_{us} of pure Ni is represented with the dotted lines. Copyright (2018) by Comp. Mat. Sci [39].

In the magnetic state, substitution of solutes with fewer d-valence electrons yield the lowest γ_{us} in each of the TM series, and it steadily increases with number of d-valence electrons until a valency of 7 corresponding to a maximum in γ_{us} is reached. However, these γ_{us} at these maxima are marginally higher than the γ_{us} of Ni.

With two solutes substitution, irrespective of the magnetic state of Ni, and the spacing between the solute atoms, except Al, V and Co, all the other alloying elements do affect the magnitude of γ_{us} (Figure 4.9 and Table 4.2). For example, in non-magnetic state, ~1 at.% substitution of Re increases γ_{us} by 7% (237 to 254 mJ/m^2) while with ~2 at.% Re atoms there is no change in γ_{us} for 1NN; but it increases to 13% (268 mJ/m^2) for 3NN configuration. Similarly, Cr also increases the USFE from 8 % for ~1 at.% to 14% for 1NN and 17% for 3NN as well as 4NN configurations corresponding to ~2 at.%. For Ti the γ_{us} decreases for 1NN configuration compared to single substitution but improvement in the magnitude is observed if they are spaced as 3NN or 4NN. For Ti, Nb, Mo, Ta, Re and W, 4NN configuration gives the highest value and improves γ_{us} by 5-16%. Only the substitutions using Ru and Ir result in highest γ_{us} for 1NN configuration.

In magnetic state, substitution with Zr and Nb with ~1 at.% Ni reduces USFE by 8% and 6% respectively and with two solutes at 1NN reduces it further to 16% and 13% while it improves to 12% and 11% for energetically favorable 4NN configuration.

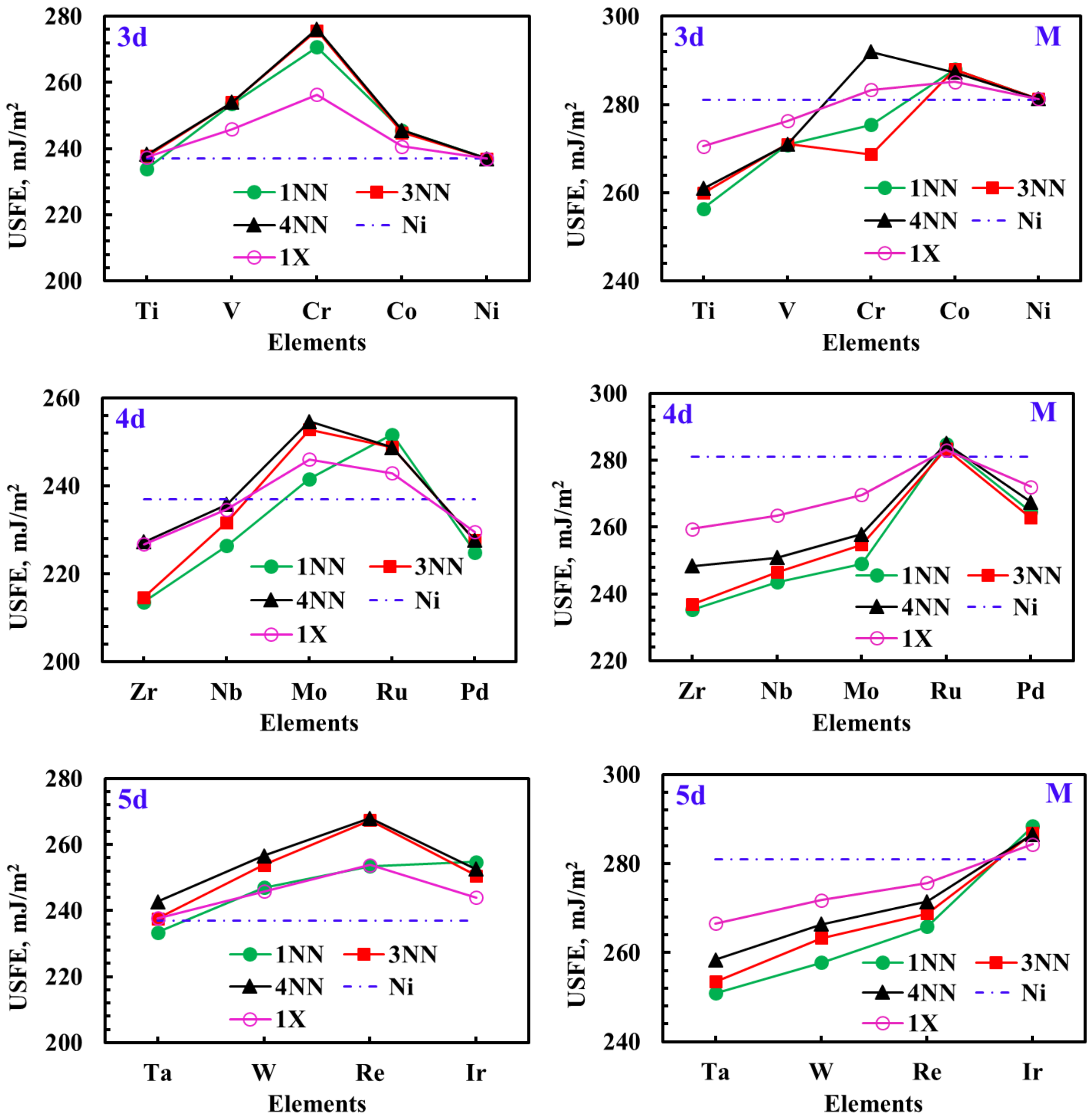

(a) (b)

Figure 4.9: Dependence of USFE (γ_{us}) on the spacing between solute atoms treated as (a) non-magnetic and (b) ferromagnetic state of Ni.

Table 4.2: Effects of solute's concentration and its relative position on γ_{us} of Ni alloy.

	Non- magnetic				Magnetic				
	~1 at.%	~2 at.%			~1 at.%		~2 at.%		
Element	**1X**	**1NN**	**3NN**	**4NN**	**1X**	**Reported**	**1NN**	**3NN**	**4NN**
Pure	237 (230 [23])	237	237	237	281	273 [61], 298 [64], 281 [68]	281	281	281
Al	241	246	246	245	275		270	270	269
Ti	237	234	238	238	271		256	260	261
V	246	254	254	254	276		271	271	271
Cr	256	271	276	276	283		275	269	292
Co	241	245	245	246	285		288	287	287
Zr	227	214	215	227	259		235	237	248
Nb	235	226	232	236	263	223 [61]	244	247	251
Mo	246	242	253	255	270		249	255	258
Ru	243	252	249	249	283		285	283	285
Pd	230	225	228	228	272		265	263	267
Ta	238	233	238	243	267		251	253	258
W	246	247	254	257	272	257 [61]	258	263	266
Re	254	254	267	268	276		266	269	271
Ir	244	255	251	252	284		288	287	287

4.5 Electronic structure analysis

To obtain a microscopic picture the individual electronic density of states as a function of energy for bulk Ni as well as Ni-based solid solution (Ir, Re and Ta) in its ferromagnetic and non-magnetic states have been examined. As d-d bonding is important in these systems [69], the partial density of states (PDOS) of the d-orbitals of the elements have been analysed.

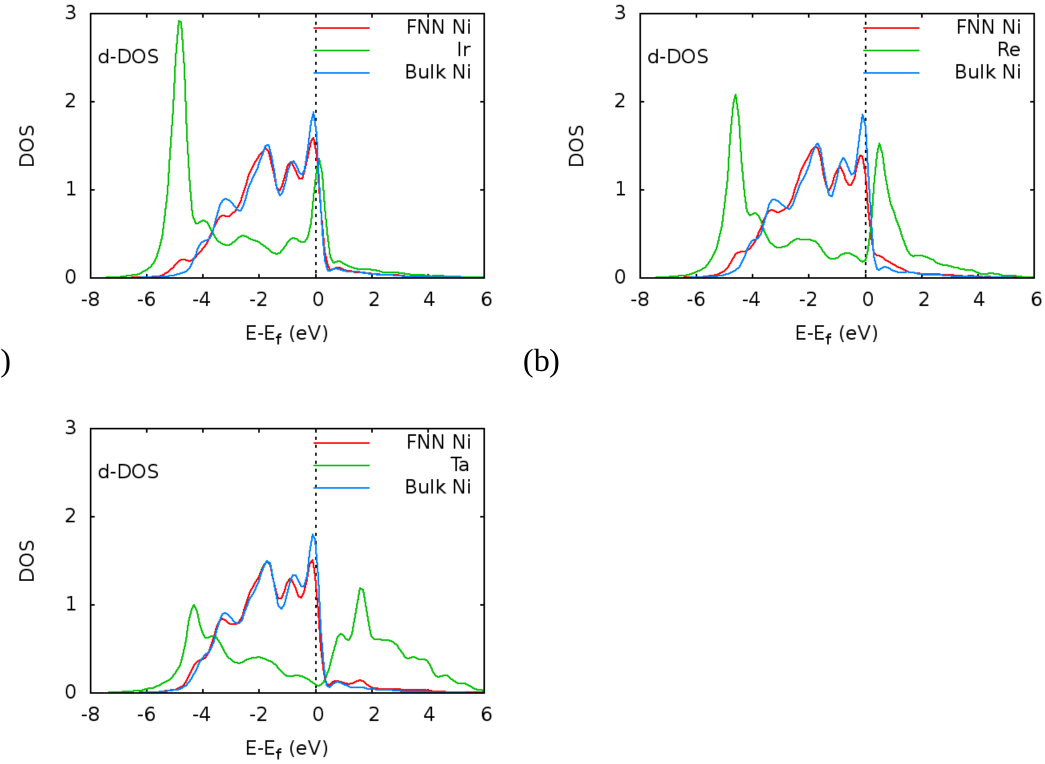

(a)

(b)

(c)

Figure 4.10: Partial density of states of d-orbitals of different atoms in (a) Ni-Ir (b) Ni-Re and (c) Ni-Ta systems in the non-magnetic calculations. Cyan, green and red lines are PDOS of bulk Ni, substituted atoms and their FNN Ni atom, respectively. Because of the symmetry of the spin, only spin-up states are shown. Copyright (2018) by Comp. Mat. Sci [39].

PDOS of d-orbital of bulk Ni, those of impurity atom and its first nearest neighbour (FNN) Ni with non-spin polarized calculations are represented in Figure 4.10. The number of states at the Fermi level (N_F) for Ni in the pure system is calculated to be 1.63, while the corresponding values for the FNN Ni atoms in Ni-Ta, Ni-Re and Ni-Ir alloyed system are calculated to be 1.27, 1.16 and 1.44, respectively. The change in γ_{is} upon alloying is observed to be in the same order as with the magnitude of N_F i.e. Ni > Ni-Ir > Ni-Ta > Ni-Re. Similar observation is also made for the magnetic case for the DOS of minority spin states at the Fermi level (Figure 4.11). The N_F for pure Ni and FNN Ni atoms of Ni-Ta, Ni-Re and Ni-Ir are 1.61, 1.36, 1.32 and 1.46, respectively, whereas the γ_{is} of the corresponding systems are 128, 113, 111 and 122 mJ/m^2. Similar empirical observation has been made for Co-based alloy based on the peak values of total DOS of faulted systems and their stacking fault energies [70]. The present results show similar correlation even when the stacking faults are not introduced in the structures. However, the majority spin states (spin-up) show the opposite trend with respective N_F values being 0.110, 0.116, 0.215 and 0.111 (i.e., the order is Ni < Ni-Ir < Ni-Ta < Ni-Re, which is exactly opposite to that of the spin-down state). Further, it is observed that the differences in γ_{is} can be related to magnetic signature at the Fermi level. The differences between up and down spin states at E_F for the FNN Ni atoms for Ni, Ni-Ir, Ni-Ta and Ni-Re system are 1.50, 1.35, 1.24 and 1.10, respectively, which follow the same decreasing trend of γ_{is} of the alloy systems.

Yu and Wang [69] have related the changes in the SFE to the bonding behavior through an analysis charge density differences of the Ni-X alloys on the close packed plane. Their results show considerable electron accumulation around Re, Mo and W in comparison to that around Cr and Ru, with least accumulation around Co. Accordingly, there is appreciable decrease in the γ_{is} of Ni, when alloyed with Re, Mo, W; moderate decrease when alloyed with Cr and Ru; and insignificant change with Co substitution, which is in accordance with the present study (see Figure 4.6b).

A semi-qualitative correlation can be observed between the PDOS in the anti-bonding region and the γ_{us}. In the non-magnetic calculations with Ta and Ir substitutions, the DOS corresponding to the FNN Ni atoms are largely unaffected in the anti-bonding region near the Fermi level (when compared with those of bulk Ni atom) (Figure 4.10). Accordingly, these substitutions change the γ_{us} of Ni very little. A similar behavior can be observed for Ir substitution in the magnetic case (Figure 4.11c), wherein again the γ_{us} is very close to that of Ni.

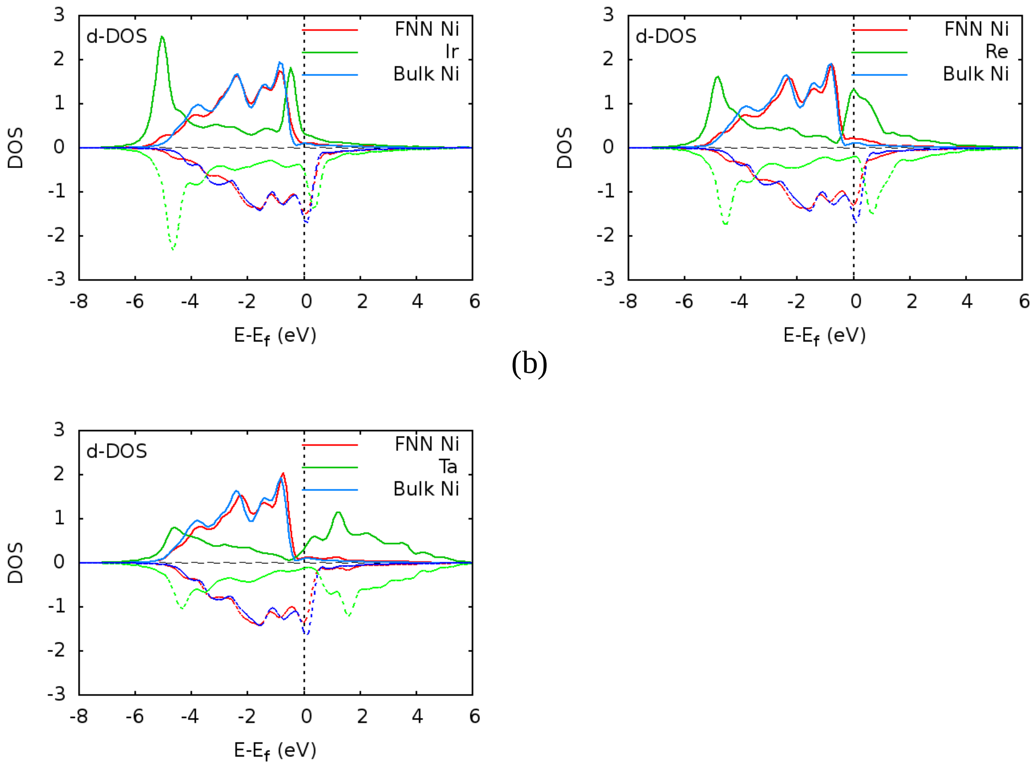

(a)

(b)

(c)

Figure 4.11: PDOS of d-orbitals of different atoms in (a) Ni-Ir (b) Ni-Re and (c) Ni-Ta systems in the magnetic calculations. Cyan, green and red lines are PDOS of bulk Ni, substituted atoms and their FNN Ni atom, respectively. Majority and minority spin states are shown using solid and dashed lines, respectively. Copyright (2018) by Comp. Mat. Sci [39].

4.6 Discussion and conclusions

Using electron microscopic techniques Carter and Holmes [71] estimated the stacking-fault energy of Ni to be 120-130 mJ/m^2. Our estimated γ_{is} of magnetic state of Ni is in this range. Reduction in γ_{is} of Ni on Co substitution has been experimentally reported in [72], which is in agreement with our results especially when the calculations are performed considering spin polarization. Except Pd, substitution with considered alloying elements, reduces the γ_{is} of Ni which indicates that the width of stacking fault will increase with these additions. Hence, these solutes can be expected to provide additional creep strength as the constriction of partials in the narrow channels would become difficult and hence the cross slip will be unfavorable. Increasing the composition of solutes by two times reduces the γ_{is} further. The decrease is in the range of 6-15 % for ~1 at.% solute substitution while in the range of 12-30 % for ~2 at.% solute. Except Zr, Ru and Ir the relative position between the solutes do not change the ISF of the system by more than 2%.

Our estimates of γ_{us} of Ni with Nb and W substitution are 263 and 272 mJ/m^2, while in another study using VASP, Seigel [61] estimated these values to be 223 and 257 mJ/m^2. This difference may be associated with the fact that 40 atoms supercell was used by him in contrast to 96 atoms in the present study and hence atomic concentration of the solutes is more than double in his work [61] as compared to ours. However, γ_{us} estimated in the present study for two solutes is pretty close to that of Seigel [61]. The γ_{us} defines the energy barrier for the nucleation of dislocation. The results indicate that in spin-polarized system all the alloying elements, except Cr, Co, Ru and Ir, weaken this barrier. However, when the spins are turned off, except Zr, Nb and Pd (all belonging to 4d series), the other alloying elements strengthen this barrier. Ta and Ti have no influence on the γ_{us}.

When the solute concentration is doubled, γ_{us} of Ni shows dependence on the relative position between the solutes. However, for Al, Ti, V, Co, Ru, Pd and Ir the variation in γ_{us} is relatively unchanged or vary up to maximum of 2%. For others γ_{us} is highest for 3rd or 4th NN configurations. Consistent with our analysis with volume change and binding energy, γ_{us} is found to be maximum for the position which is defined to be the stable configuration. For example, Cr, Mo, W and Re are added as solutes, the system is more stable when they are either 3NN or 4NN compared to be as 1NN. Accordingly, γ_{us} are maximal for the systems where the solutes are farther separated. With Co and Ru, which shows a tendency towards clustering, γ_{us} is relatively unaffected or marginal decrease is observed with increasing spacing.

In summary, we have performed first-principles calculations to understand the effect of solute substitution from 3d, 4d and 5d series of transition metals on Ni in terms of γ_{is} and γ_{us}. In the present study Ni has been considered in both non-magnetic and ferromagnetic states. The major inferences from the present results can be summarized as follows:

- γ_{is}, irrespective of the magnetic state of Ni, decreases with solute substitution. Increasing solute concentration further reduces it. Also 4d and 5d solutes decreases γ_{is} more as compared to 3d elements.
- Spacing between Zr, Ru and Ir do affect the γ_{is}. γ_{is} increases by 13% for Zr and decreases by 7% for Ru if the solute are spaced from 1NN to 4NN.
- γ_{us} is around 19% higher when Ni is ferromagnetic and very nominal increase in this value is observed with solute addition. 3d elements have higher influence on the γ_{us} as compared to 4d and 5d elements. However, for non-magnetic Ni, except for Zr, Nb and Pd (all from 4d), all solute increases the γ_{us} and maximum value is observed for Cr, Mo and Re from 3d, 4d and 5d series all with valency 5 respectively.
- Spacing between solutes affects the γ_{us} of the system. γ_{us} improvement in the range of 3-7 % is observed if separation between the solute is increased to 3NN or 4NN from 1NN for Cr, Zr, Nb, Mo, Ta, W and Re.

Chapter 5

Tuning Planar Fault Energies of Ni_3Al Dilute Solid Solution*

5.1 Introduction

Nickel-based superalloys used for high-temperature applications are designed as precipitation hardened alloys wherein the precipitate phase is based on Ni_3Al. It is an ordered compound with $L1_2$ crystal structure, which is a superlattice based on a FCC structure where the minority atom Al occupies the corner position and the Ni atoms occupy the face centres. As a result of the cubic symmetry, the compounds in the $L1_2$ structure possess the maximum number of slip systems and hence exhibit ductile behavior. However, the movement of dislocation in Ni_3Al, because of its ordered structure, is far more complex compared to that in a solid solution. In fact, it is this ordered structure that is responsible for the formation of various planar defects that finally results in exhibiting anomalous yield effect (rise in the yield strength with increasing temperature ~800°C) [5]. The anomalous yield effect is a phenomenon originating from the structure and properties of *superdislocation* and is associated with its dissociation on both {111} and {100} planes. This is mainly due to thermally activated

---

* This work has been published in part in Scripta Materialia [73]. Copyright (2017).

cross slip from the (octahedral) primary slip plane to the cubic plane leading to dislocation movement locking (Kear-Wilsdorf lock). The difference in the APB energy on $\{111\}$ and $\{100\}$ is one of the key factors controlling the activation enthalpy of cross slip of a $a\langle 1\bar{1}0\rangle\{111\}$ dislocation [74, 75]. Further, a dislocation travelling in the matrix phase cannot enter the Ni_3Al (precipitate) phase without generating an APB which results in substantial order strengthening [1].

5.2 Dislocation movement in ordered Ni_3Al

Superior high-temperature strength of Ni-based superalloys is attributed to the anomalous flow stress behavior which is associated with a complex movement and interaction of the dislocations in the ordered γ' phase. Because of the ordered occupancy of the Ni and Al atoms, the basis vector on the $\{111\}$ becomes $\langle 110\rangle$ and not the $^1/_2\langle 110\rangle$, which is the basis vector in FCC structures . Hence, a perfect dislocation in Ni_3Al has Burgers vector, $\langle 110\rangle$, that is twice the length of that in FCC crystals; accordingly, this perfect dislocations are called *superdislocations*. In a coherent system, wherein the ordered lattice of the intermetallic phase is in registry with that of the surrounding matrix phase, the lattice vector $\langle 1\bar{1}0\rangle\{111\}$ of a perfect dislocation dissociates into two partial dislocations, also known as *superpartials*, $^a/_2\langle 1\bar{1}0\rangle\{111\}$ encompassing a planar defect. Translating half of the crystal by $^1/_2\langle 110\rangle$ relative to other half would replace Al atoms on Ni sites, leading to the generation of a planar defect called anti-phase boundary (APB) [76].

5.3 Anti-phase boundary (APB)

In Ni_3Al, under equilibrium conditions, all the twelve first nearest neighbours (NNs) for Al are Ni, and, for Ni, eight of them are Ni and the rest four are Al. The six second NNs for Al (Ni) are Al (Ni). Any change in this neighbouring configuration leads to the formation of a planar defect with an interface called anti-phase boundary (APB). Hence, APBs in the ordered phases (e.g. γ') appear as a result of dislocation motion and are characterized by the crystallographic plane that forms the boundary between the slipped and unslipped regions.

The process of APB generation is associated with breaking of certain bonds and formation of certain other bonds. Hence, the magnitude of APB energy (APBE) depends upon the crystallographic plane on which the APB resides. For example dislocation movement in Ni_3Al by ${}^{a}/_{2}\langle 1\bar{1}0\rangle\{111\}$ (vector linking neighbouring Ni and Al) leads to the formation of forbidden Ni-Ni and Al-Al bonds as first nearest neighbours. This interface generation requires substantial energy penalty and is reported to be in the order of ~100 mJ/m^2 [1] and is estimated to be 182 mJ/m^2 in the present study. However, in the case of $\{100\}$ planes, a translation of ${}^{1}/_{2}\langle 110\rangle$ does not change the first neighbour configuration and accordingly its magnitude is significantly lower (90 mJ/m^2 [48]) compared to the $\{111\}$ APBs.

High energy penalty required to generate APB requires dislocation to move in pairs, the former generating while the latter eliminating it and can be represented as

$$[1\bar{1}0] \rightarrow {}^{1}/_{2}[1\bar{1}0] + APB + {}^{1}/_{2}[1\bar{1}0]\,,$$

where $[1\bar{1}0]$ is the Burgers vector of a perfect *superdislocation* dissociating into two ${}^{1}/_{2}[1\bar{1}0]$ partial superdisloactions. Hence, the extent of strengthening of Ni-based alloys depends on the energy associated with its APB as it governs the stress required by the dislocation to shear through the γ'.

5.4 Superlattice intrinsic stacking fault (SISF)

There are other ways that the *superdislocations* can dissociate into multiple partials dislocations connected by faults of various kinds. [5] Most commonly observed stacking faults are superlattice intrinsic stacking fault (SISF) and complex stacking fault (CSF), both causing an intrinsic stacking fault in the underlying FCC lattice. SISF conserves the first nearest neighbour of all the atoms while CSF alters some configuration. Movement of dislocation by ${}^{a}\!/_{3}\langle\bar{2}11\rangle\{111\}$, changes the stacking sequence from ABCABCABC…. to AB**CACA**BC…resulting in the formation of a superlattice intrinsic stacking fault (SISF). The SISF energy (SISFE) is a key parameter that is relevant to the spacing (R) between *superpartials* (SISFE $\propto$ 1/R) [1]. A lower SISFE reduces the possibility of cross slip and reduces the steady-state creep rate [56, 57].

Hence, the mechanical properties of ordered Ni_3Al are affected by the existence of *superdislocations* and by the formation of extended *superdislocations (or superpartials),* which consist of partial dislocations bounding stacking faults SISFE or antiphase boundaries (APB). The energies involved in the formation of APB, CSF and SISF are instrumental in determining the deformation behavior of this ordered intermetallic [77].The strengthening behavior of γ' also depends on the ease of being sheared by the dislocation coming from γ matrix. Hence it would be of fundamental interest to study the effect of solute substitution on the magnitude of the planar fault energies such as APBE and SISFE along with the unstable stacking fault energy (USFE).

Numerous studies, both theoretical and experimental, have been reported addressing the effect of alloying elements on the fault energies of γ' [78-80]. Using DFT Chandran and Sondhi [81] calculated the APB energy (APBE) in Ni-based binary and ternary alloys for APBs on (111) as well as (100) planes. In another study, Yu and Wang [55] estimated the effects of single elemental substitution of Al with Re, Ta, W, Ru and Ti on the stacking fault energies such as complex stacking fault energy, APBE and SISFE and the strength of γ' (Ni_3Al). Mishin [64] carried out comprehensive study on the atomistic modeling of pure γ and γ'phases using molecular dynamics. However, to the best of our knowledge, a comprehensive analysis of the effect of solute substitution for Ni, Al, and simultaneously for Ni and Al atoms separated as first NN on the fault plane {111} of Ni_3Al (which is the basis system for γ') on the USFE, the SISFE and the APBE is lacking. In the present chapter, we present a systematic analysis of the influence of substitution of Ni atom, Al atom and Ni and Al atoms simultaneously with 3d, 4d and 5d transition metals on (111) fault plane of Ni_3Al on energies of these faults.

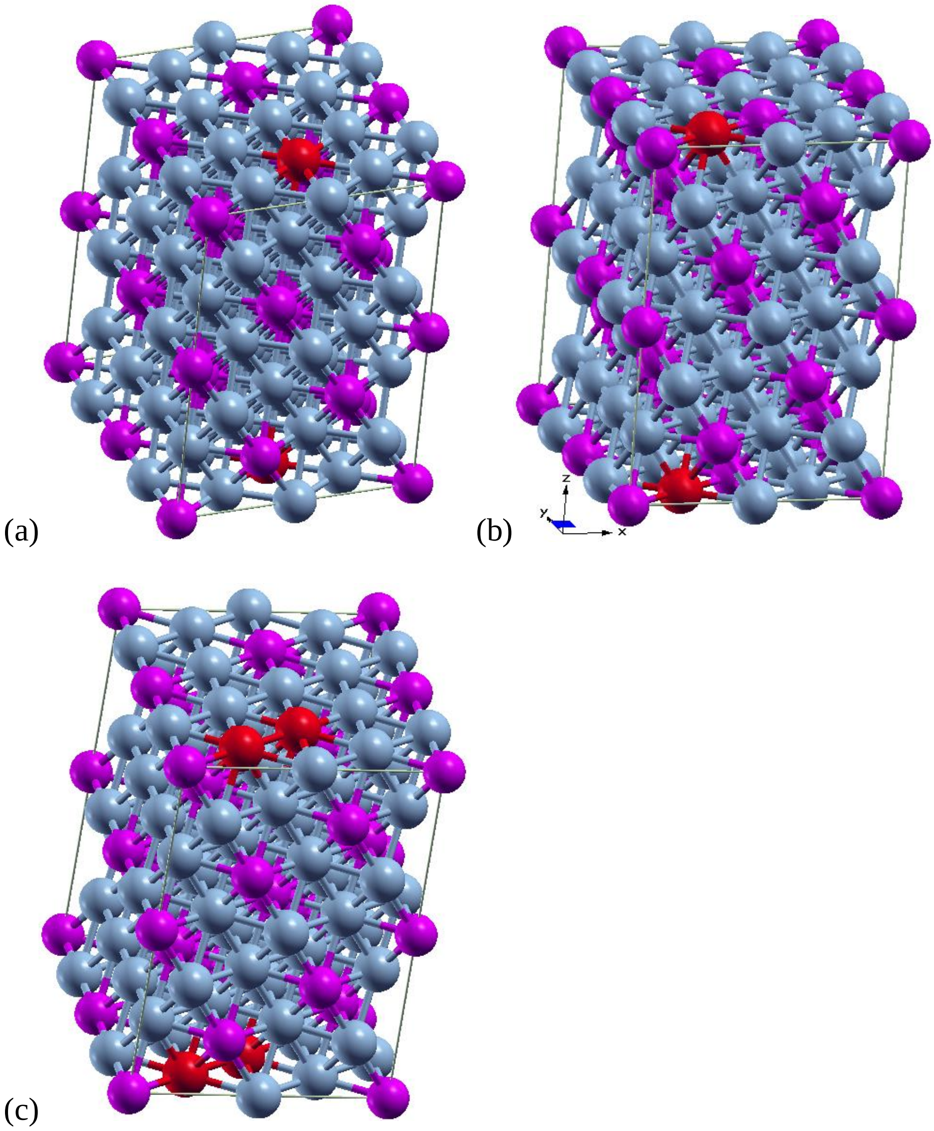

Figure 5.1. Schematic representation of solute substitution for (a) Al (b) Ni and (c) Al and Ni atoms simultaneously on the fault plane {111} in Ni_3Al.

5.5 Computational details

To simulate substitutionally alloyed γ' phase, we used a supercell containing 96 atoms by stacking six (111) atomic layers (two successive stacking sequences ABCABC), with 16 atoms in each layer (Figure 5.1). The supercell having L1$_2$ ordered structure with Ni$_3$Al composition was constructed using three orthogonal vectors parallel to $[1\bar{1}0]$, $[11\bar{2}]$ and [111] (Figure 5.2a). This periodic system was used to model alloys with a single Ni or Al atom or Ni and Al atom on the shearing plane (i.e. (111)) substituted with the alloying element/elements Ti, V, Cr, Mn, Fe, Co and Ni (Ni on Al-site) (3d), Zr, Nb, Mo and Ru (4d) and Hf, Ta, W, Re and Ir (5d). This is an exhaustive list of alloying elements used in single crystal superalloys [1].

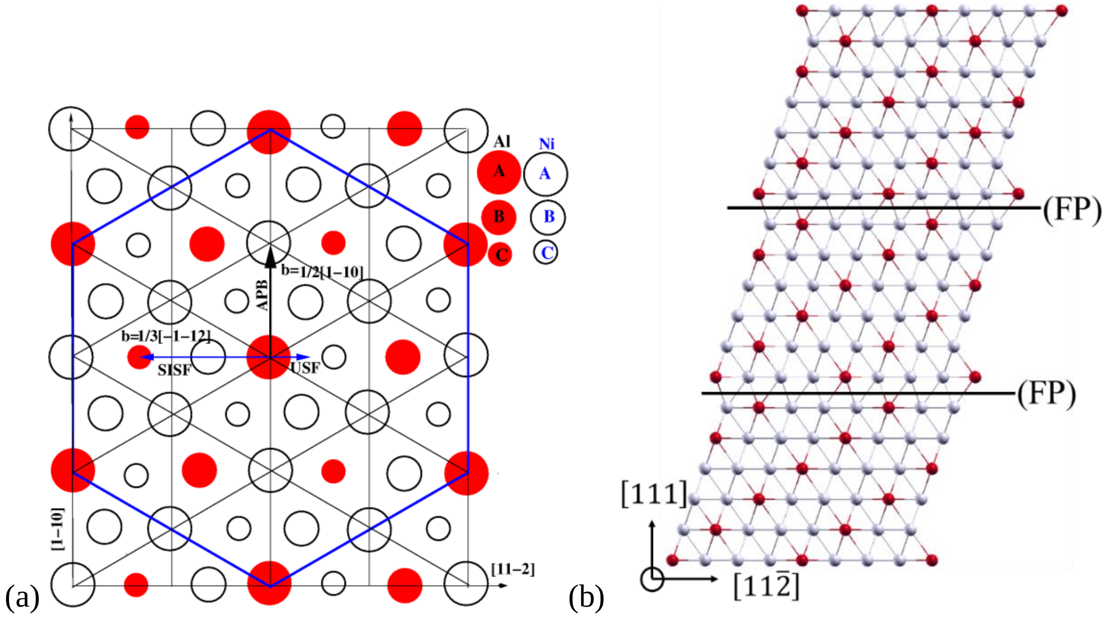

Figure 5.2. (a) Geometrical representation of stacking of (111) planes in L1$_2$ crystal structure. Arrows give the translations required for generating the APB, SISF and the USF. (b) Projection of atomic planes along y-axis ($[1\bar{1}0]$ direction) showing periodic images shifted by a fault vector. The positions of the fault planes (FP) have been marked with dark lines. Copyright (2017) by Acta Materialia Inc [73].

The system was allowed to relax completely to obtain the minimum energy configuration. The relaxed configuration of each substitutional alloy was used in subsequent analysis and calculation of various planar fault energies as shown in equation 4.5. The faults were generated by providing suitable displacements to the periodic images along $[1\bar{1}0]$ and $[\bar{1}\bar{1}2]$ respectively (Figure 5.2b). After introducing a fault, the structure was relaxed completely, except the top and bottom layers which was allowed only to relax with respect to atomic displacement in the direction perpendicular to the fault plane. The fault energies, as explained in the previous chapter, were determined as the difference between the energies of the faulted and the corresponding unfaulted configuration, normalized with respect to the area of the unit cell containing the substituted atom. In the calculations of APBE and SISFE of Ni_3Al, the periodic image of the supercell was displaced by $1/2\,[1\bar{1}0]$ and$1/3[\bar{1}\bar{1}2]$ respectively, on the (111) plane (as represented in Figure 5.2).

Table 5.1: Comparison of theoretical estimates and experimental values of lattice parameters and fault energies of γ' phase. Copyright (2017) by Acta Materialia Inc [73].

Property	Present study	First-principles	Experimental
a_o(Å)	3.58	3.573 [90], 3.58 [91]	3.572 [92]
APBE (mJ/m^2)	182	181 [81], 152 [83], 188 [84], 210 [85]	180 [86], 175 [87], 195 [88]
SISFE (mJ/m^2)	29	39 [83], 80 [85], 68 [93]	10 [1], 6 [87], 35 [89]
USFE (mJ/m^2)	227	254 [55]	

5.6 Results:

5.6.1 Validation of stacking fault energy for bulk Ni_3Al

The equilibrium lattice parameter (a_o) of Ni_3Al was obtained from the variation in energy with cell size. APBE and SISFE for pure Ni_3Al were estimated to benchmark the quality of *pseudopotentials* used in DFT calculation and its comparison with reported experimental and other first-principles calculations are reported in Table 5.1. The estimated lattice parameter is 3.58 Å is in very good agreement. The APBE estimated in the present study for pure Ni_3Al is 182 mJ/m^2 which is in good agreement with the published results from first-principles 181 [81], 172 [82], 152 [83], 188 [84], 210 [85] and experimental values of 180 [86], 175 [87], 195 [88]. It may be noted that our estimation of APBE for system sizes of 48 atoms (6 layers), 96 atoms (6 layers) and 192 atoms (12 layers) are 179.0, 182.2 and 182.2 mJ/m^2, respectively. Thus a system size of 96 atoms (6 layers) is reasonably adequate to overcome the image force effects arising due to periodic images, and hence has been chosen for all the studies reported in this thesis (Figure 5.2b). Our estimate of SISFE (29 mJ/m^2) falls between the experimental measurements (10 [1], 6 [87], 35 [89]) and other first-principles calculations. In general, SISFE is expected to be small as it does not generate any first nearest neighbour disturbances. Our estimate of the USFE of pure γ' phase (227 mJ/m^2) is slightly lower than that calculated by Yu and Wang [55], and this difference may be attributed to the differences in the way simulations were carried out. While Yu and Wang [55] used a slab model and kept the positions of the two surface layers of atoms fixed to avoid surface reconstruction (due to a 12 Å thick vacuum region), our calculations did not have such constraints as there are no surfaces or vacuum in our set-up (Figure 5.2).

5.6.2 Effect of solutes on APBE

The solute substitution in Ni_3Al is bound to have its effect on the APB energy. The variations in APBE with number of d-orbital valence electrons of the alloying element (substituted for Al atom, Ni atoms and both Al and Ni atoms) are shown in Figure 5.3. For solute substitution at Al site, within each period of the periodic table, APBE increases marginally to reach a maximum for elements having half-filled d-orbitals, and reduces considerably after that (Figure 5.3 a). Excepting Fe, Co, Ni and Ir, the substitution with other elements leads to an increase in the APBE compared to that of pure Ni_3Al. It is evident that the maximal in APBE with substitution across a transition metal period increases from the 3d to 5d series. However, solutes from 4d and 5d series of transition metals have comparable APBs for same number of d-orbital valence electrons. The results of the present study show similar qualitative trend when compared with an earlier DFT calculations on ternary systems [55] which showed increase in APBE with addition of Re, W, Ta, Ti and a decrease upon addition of Ru. When a Ni atom is substituted at an Al site, there is a significant reduction of 41% in APBE, as the configuration in the defect plane leads to a situation with a reduced number of the energetically expensive and thus thermodynamically unstable Ni-Ni and Al-Al bonds (which is a characteristic of the APB), compared to an APB in pure Ni_3Al.

The effects of substitution for Ni atom with different alloying elements on APBE is depicted in Figure 5.3b. Substitution at Ni sublattice site with Fe, Co, Ru and Ir reduces the APBE whereas an increase is observed for alloying with the rest of 3d, 4d and 5d series TMs. While APBE generally decreases monotonically with increase in the number of d-orbital valence electrons, V ($3d^3$), Zr ($4d^2$) and Hf ($5d^2$) provide maximum increase in APBE within a period. An important observation is that excess Ni present at the anti-sites at the fault plane tends to reduce the values of APBE by 41%, whereas the presence of excess Al at anti-sites increases the respective energies by 43%.

With the creation of an APB, the number of first nearest neighbour (FNN) Al-Al and Ni-Ni violations are respectively 0.5 per Al atom and 0.16 per Ni atom, where the referred Al and Ni atoms are on the planes adjacent to (on either sides of) the fault plane. With the introduction of a Ni anti-site, these numbers become 3/7 (~0.43) and 3/25 (~0.12) i.e., there is decrease in both Al-Al and Ni-Ni violations, which might seem to suggest a decrease in fault energy compared to system without antisites. However, similar argument cannot be extended to system containing Al antisite, wherein the normalized number of Al-Al and Ni-Ni FNN violations are, respectively 3/9 (~0.33) and 3/23 (~0.13). If the argument is based on FNN violations only, one would expect a decrease in APB energy compared to the system without any antisite defects. The concentration of Ni in the adjacent planes about the fault plane are 0.78 and 0.72 in the systems with Ni-antisite and Al-antisite respectively. Hence, the asymmetry may be attributed to compositional effect (segregation of alloying elements at the defect area). This has been found in experimental studies too (163±21 mJ/m^2 for Ni-24.2Al and 190±26 mJ/m^2 for Ni-25.9Al [94] and in other simulation works [95].

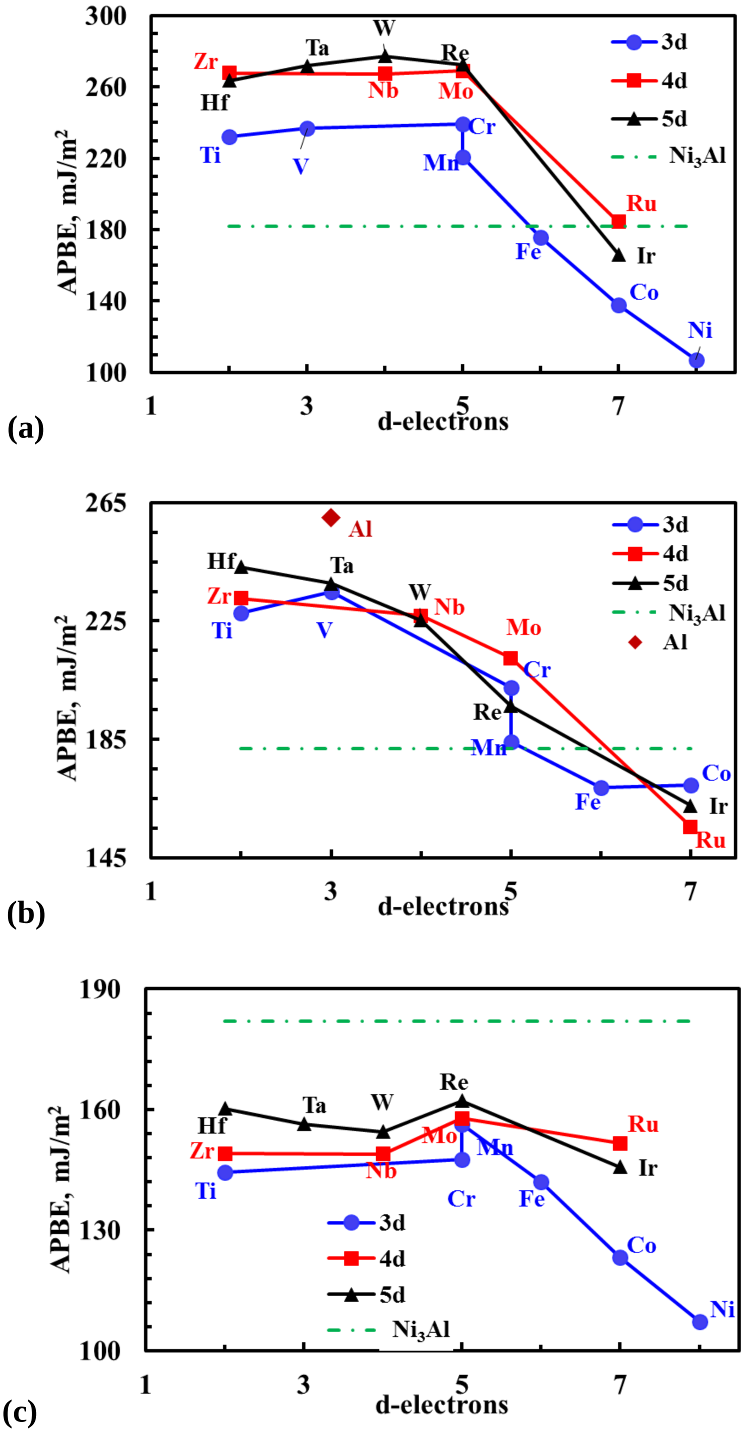

Figure 5.3. Effects on APBE associated with solute substitution at (a) Al (b) Ni and (c) Al and Ni sublattice site. The fault energies of pure Ni_3Al are represented by the horizontal dashed lines. Figure 5.3 a-b copyright (2017) by Acta Materialia Inc [73].

When two solutes are substituted for Ni and Al that are separated as first nearest neighbour on the {111} fault plane, the trend (or the form of variation with d-orbital valence electrons) observed is almost similar to the behavior of ~1 at.% solute substituted for an Al atom. However, the APBE is substantially reduced in comparison to that of pure Ni_3Al. This is interesting because while most of the substitutions for either an Al or a Ni atom lead to increase in the APBE, the synergetic effect is not seen when the two atoms are simultaneously substituted. Hence it can be inferred that the magnitude of APBE is greatly dependent on the % of Al and Ni atoms which directly links to the formation of the forbidden bonds such as Ni-Ni and Al-Al.

5.6.3 Effect of solutes on SISFE

In this section an attempt has been made to understand and find any correlation on the effect of solute substitution, similar to APBE, on SISFE for Ni_3Al. The variations in SISFE with number of d-orbital valence electrons of the alloying element (substituted for Al atom, Ni atoms and both Al and Ni atoms separated as 1NN on the fault plane) are represented in the form of graph (Figure 5.4).

For elemental Al substituted by the solute, within each period of the periodic table, variation in the SISFE with alloying shows a similar trend (as in APBE) for 3d TMs (Figure 5.4a). However, it monotonically decreases with increase in the number of d-orbital valence electrons for 4d and 5d series of TMs. Substitution of Cr, Zr and Hf belonging to 3d, 4d and 5d series of TMs respectively, results in maximal increase in the SISFE. Substitution with Ni reduces the SISFE by 40 % while that with Co or Ir leads to a marginally higher value of SISFE compared to that of pure Ni_3Al. Substitutions with other elements increase the SISFE by 100 to 350 % with maximal effect for Zr as solute. Earlier DFT calculations on ternary systems [55] showed increase in SISFE with addition of Re, W, Ta, Ti and a decrease upon addition of Ru, which are qualitatively similar to our results.

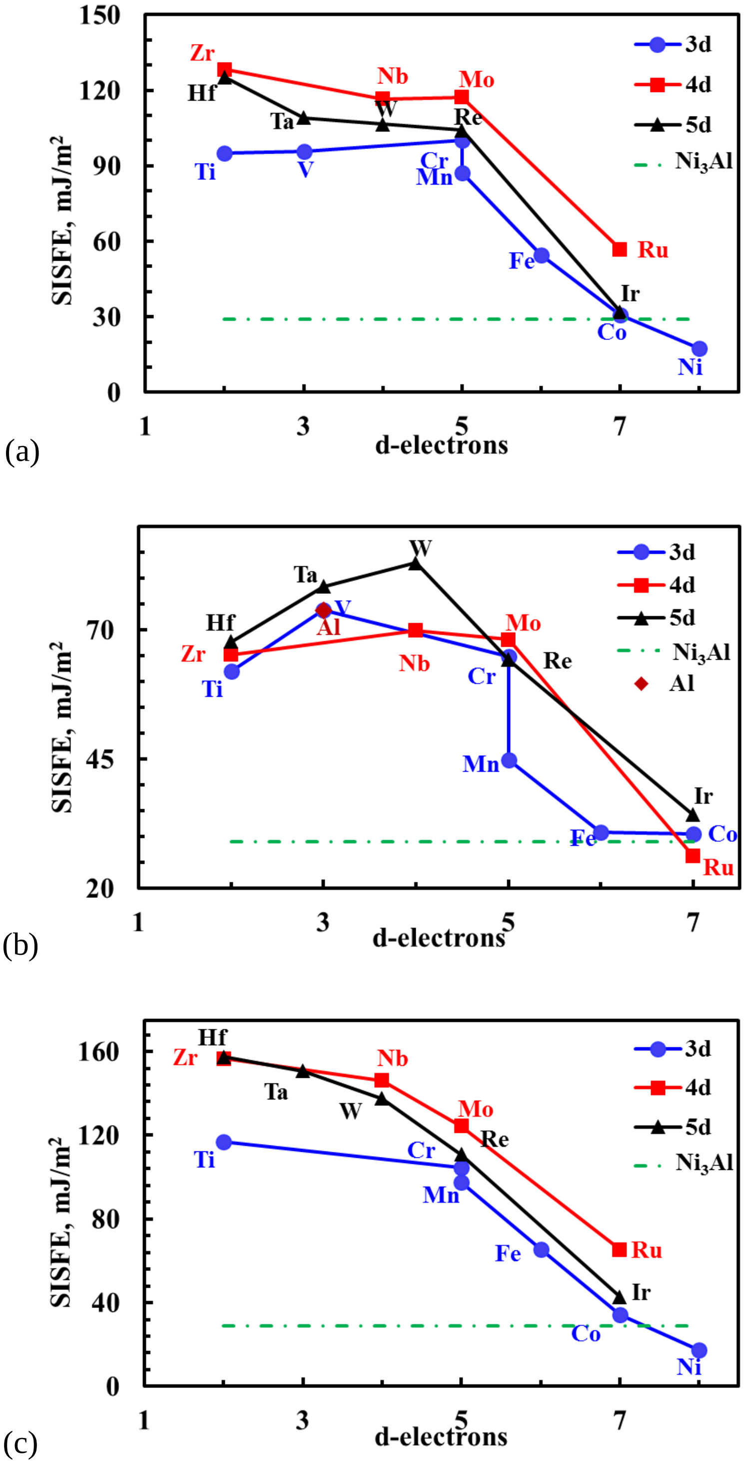

Figure 5.4. Effects on SISFE associated with solute substitution at (a) Al (b) Ni and (c) Al and Ni sublattice site. The fault energies of pure Ni_3Al are represented by the horizontal dashed lines. Figure 5.4 a-b copyright (2017) by Acta Materialia Inc [73].

The effects of substitution for Ni atom with different alloying elements on SISFE are represented in Figure 5.4b. SISFE first increases, reaching a maximum and thereafter it decreases. With respect to pure Ni_3Al, SISFE decreases with substitutional alloying with Ru. An important observation is that excess Ni present at the anti-sites at the fault plane tends to reduce the values of SISFE by 40 %, whereas the presence of excess Al at anti-sites increases the respective energies by 152%. This increase in SISFE due to incorporation of Al anti-sites may have similar chemical origin as described for APBE. For same solute, elemental substitution of Al results in sufficiently higher SISFE in comparison to Ni substitution.

Also the SISFE increases more for solutes with fewer number of d-orbital valence electrons. Hence, it can be inferred that solutes with higher number of d-electron substituted for Ni will result in minimum increase in SISFE and hence providing better creep properties.

For simultaneous substitution of Al and Ni atoms separated as first nearest neighbour with solutes, SISFE monotonically decreases with increasing d-orbital valence electrons of the solutes. The rate of decrease is gradual for solutes upto half-filled d-orbital and thereafter there is steep decrease. The values of SISFE for 5d elements lies in between the 3d and 4d solutes. Contrary to APBE, the magnitude of SISFE is highest for simultaneous substitutions of solutes at Ni and Al sublattice. This implies that the SISFE is critical to solute concentration.

5.6.4 *Effects of solutes on USFE*

In the present study effect of solute substitution on USFE is systematically analysed. The variations in USFE with number of d-orbital valence electrons of the alloying element substituted for Al atom, Ni atoms and simultaneous substitution for Al and Ni atoms (as 1 NN on the fault plane) are shown in Figure 5.5 a-c respectively.

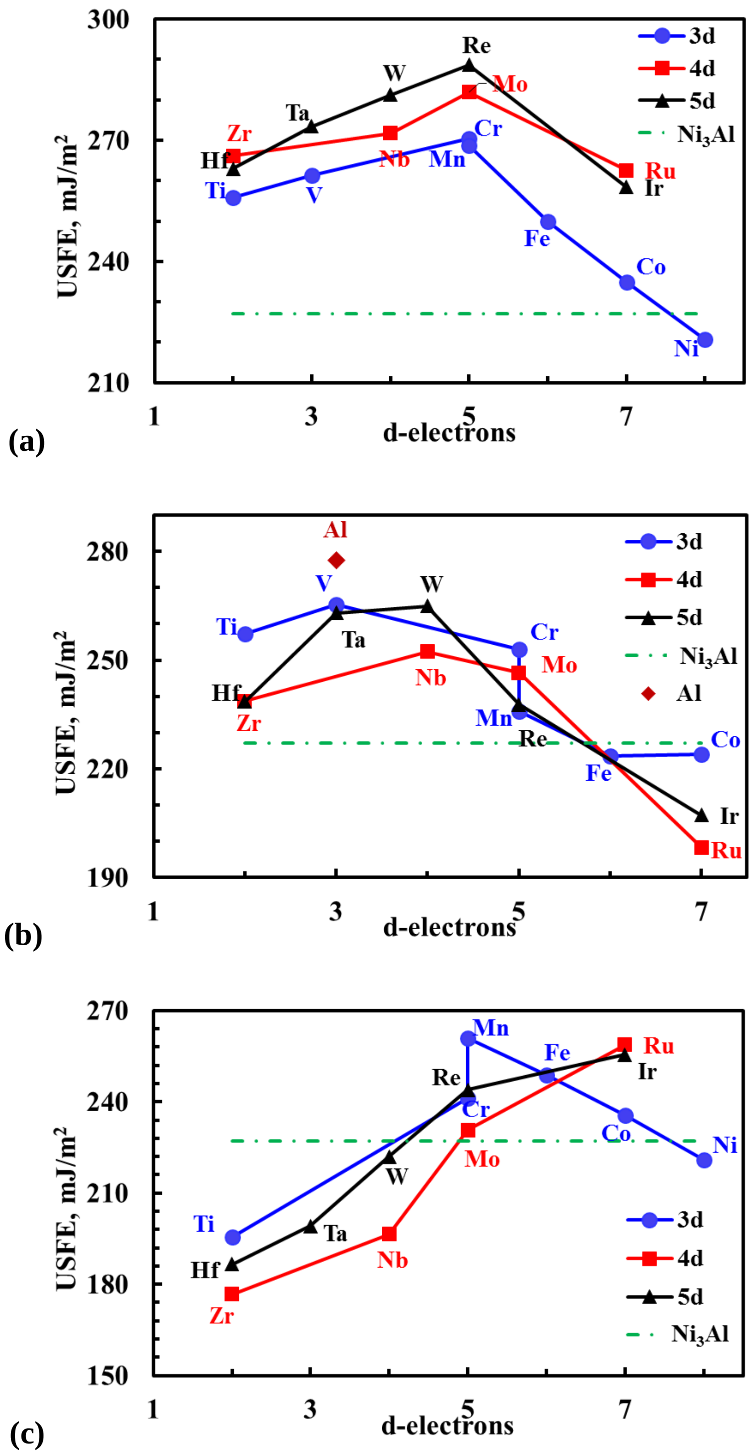

Figure 5.5. Effects on USFE associated with solute substitution at (a) Al (b) Ni and (c) Al and Ni sublattice site. The fault energies of pure Ni_3Al are represented by the horizontal dashed lines. Figure 5.5 a-b copyright (2017) by Acta Materialia Inc [73].

For solute substituted with TMs within each period at Al sublattice the variation of USFE (Figure 5.5a) shows a somewhat similar trend than that of APBE (Figure 5.3a). However, as compared to variation of APBE the USFE shows an improvement of about 6 - 11% increase before reaching a maximum for elements belonging to half-filled *d*-orbitals, viz., Cr, Mn ($3d^5$), Mo ($4d^5$) and Re ($5d^5$) with in each period. Excepting Ni, all other substitutions lead to increase in the USFE compared to that of pure Ni_3Al. This trend is exactly opposite to that seen in the changes in volume (Figure 3.5) suggesting a possible correlation between volume changes associated with the solute atoms and the shear strength. One possible explanation for this is that the associated strength of the strain field is larger for substitutional elements causing large volume change, which is reflected as changes in USFE.

For solute substitution for Ni atom, similar to substitution at Al sublattice, USFE first increases, reaching a maximum and decreases thereafter. While a maximum increase in USFE is seen for elements with half-filed d-orbital in the case of substitution for Al atom, no such definite behavior is found in effects of substitution for Ni atoms. Substitution with V ($3d^3$), Nb ($4d^4$) and W ($5d^4$) leads to maximum increase in USFE within the respective periods. It is important to note that Ni present at the anti-sites at the fault plane tends to reduce the values of USFE by 3%, whereas the presence of excess Al at anti-sites increases it by 22%. In fact, this is the highest USFE observed with solutes considered in the present study for substitution at Ni sublattice. However, solute substitution at Al sublattice provide much higher strengthening. Hence, it can be inferred that solutes that prefer Al sublattice substitution will provide resistance to dislocation movement.

Simultaneous solute substitution from 3d series of TMs at Al and Ni sublattice increases the USFE reaching maxima for half-filled d-orbitals. However, for 4d and 5d elements monotonically increases with d-electrons. Among the three cases considered USFE is minimum when solutes with less than 5 electrons are occupying the Al and sublattice position separated by 1NN on the fault plane.

5.7 Discussion

Baluc and Schaublin [96] estimated APBE from the dislocation widths in the TEM micrographs. They reported APBE of $Ni_3(Al,1\%Ta)$ to be 237±30 mJ/m^2, as compared to 195±13 mJ/m^2 for the binary Ni_3Al [88]. Our simulation results for the APBE of Ni_3Al is 182 mJ/m^2 which is within the range while 272 mJ/m^2 for $Ni_3(Al,Ta)$ is slightly higher than the experimental value. The difference may be attributed to the Ta composition which is 4% of total Al content as compared to 1% used for experimental technique. Substitution at Al sublattice provides highest APBE followed by those at Ni sublattice. Simultaneous substitution at Al and Ni sublattice drastically reduces the APBE. Presence of Ni at the anti-sites on the fault plane reduces the values of APBE by 41%, whereas for Al anti-sites it increases it by 43%. Hence, at higher temperatures where the prominent creep deformation mechanism is APB related shearing, solutes that prefer Al sublattice can be expected to provide more resistance to plastic deformation.

Baluc and Schaublin [96] have also reported an increase of 150% in the SISFE for $Ni_3(Al,1\%Ta)$ (15±5 mJ/m^2) compared to a value of 6 mJ/m^2 [87] for pure Ni_3Al. While our calculations show an increase of 270%, the fault energies themselves with and without Ta estimated here are 109 and 29 mJ/m^2, which are different from the above experimental findings. This extent of difference in energetics between computations and experiments is not very uncommon and the deviation can be attributed to various factors such as (a) considering atom of Ta in the fault plane only in the modeling work, (b) difference in the concentration of Ta in the two studies, (c) experimental difficulty in accurate determination of the spacing between partials, from which the defect energy is estimated and (d) finite temperature effects. Among the different configuration considered, SISFE is found to be lowest, and thus at intermediate temperatures where creep deformation is prominently governed by isolated stacking faults, solutes that prefer Ni sublattice can be expected to reduce the creep rates.

We found a correlation between APBE and SISFE (Figure 5.6), irrespective of whether the alloying element is in Ni-site or Al-site. A similar correlation can be seen for the data published by Vamsi and Karthikeyan [83]. It may be observed that these correlations have been obtained using limited amount of data. However, they may prove to be thumb rules in cases where the estimation of SISFE is difficult.

USFE was estimated and, similar to APBE, solute substituted at the Al sublattice provide highest value. For Al sublattice substitution by solutes from 3d, 4d and 5d series of transition metals USFE increases reaching a maximum for half-filled *d*-orbitals, viz., Cr, Mn ($3d^5$), Mo ($4d^5$) and Re ($5d^5$) followed by decrease in the value.

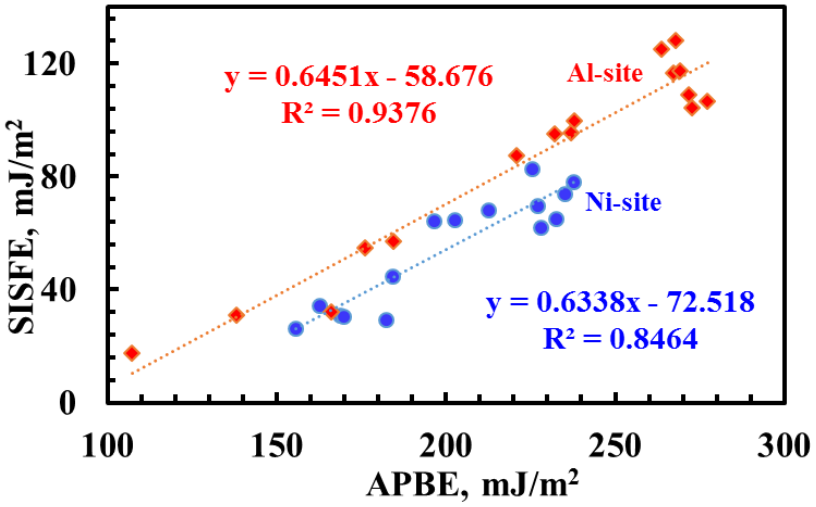

Figure 5.6: Correlation between APBE and SISFE for solute at Al and Ni sublattice sites in Ni_3Al. Copyright (2017) by Acta Materialia Inc [73].

5.8 Conclusion

We have determined the APBE, SISFE and USFE for solutes substituted at Al or Ni or both sites in Ni_3Al on the (111). Our results indicate that substitution of elements, considered in the present study, at the Al-site and at Ni-site, barring Fe, Co, Ru and Ir, leads to an increase in USFE. Since USFE is related to the energy release rate during dislocation nucleation [97], most alloying elements seem to provide strengthening by increasing the barrier energy. This is in line with the experimental findings of Shah and Duhl [98] that the stress required to achieve minimum creep rate of best multicomponent alloys is about four times that of the binary compound Ni_3Al.

In summary, there is a clear trend in the variation of USFE, APBE and SISFE for 3d, 4d and 5d transition metals substitution (~1 at.%) at Al site, with the numbers of electrons in the d-orbitals with five half-filled d-orbitals being at the cusps. As compared to substitution at Ni site, substitution at Al site provides better strengthening as is reflected in higher values of USFE and APBE. However, detailed density of states calculations would be able to explain this behavior, we surmise that this could be due to *d-d* interaction (between the solute and Ni) in the alloyed systems as compared to *p-d* interaction in Ni_3Al. We do not find extrema at the half-filled d-shell (d=5) in the systems where Ni atom is substituted (as only the magnitude of *p-d* interaction changes in these systems). However, SISFE, which governs the spacing between the partials, is lower when the solute is added at the Ni sublattice.

Chapter 6

Influence of Solutes on Ductility in Ni-based Solid Solution*

Strength of materials can be estimated either through calculation of its cohesive energy or by calculating the work done to generate new surfaces. Cohesive strength is calculated as the energy required to break atomic bonds (Figure 6.1). Large elastic constant, high melting temperature and small coefficient of thermal expansion are all manifestation of the strong cohesive forces present in a material. The variation in the interatomic forces between two atoms as a function of separation between them (b_o+r, where b_o is the equilibrium interatomic distance and r is the deviation from equilibrium interatomic distance), is represented as Figure 6.1 This curve is the net result of the repulsive (F_r) and attractive forces (F_a) between the atoms as a function of their distance of separation. If the crystal is subjected to a uniaxial tensile loading, the separation in the loading direction between atoms increases. The F_r decreases more rapidly as compared to the F_a with increasing separation, such that the net attractive force balances the tensile load. Above some specific load, which is material dependent, the separation between atoms increases such that the F_r becomes negligible and the F_a starts reducing. This separation corresponds to the maximum value for the cohesive force between the atoms.

---

* This work has been published in part in Comp. Mat. Sci [39] Copyright (2018), Comp. Mat. Sci [48] Copyright (2014).

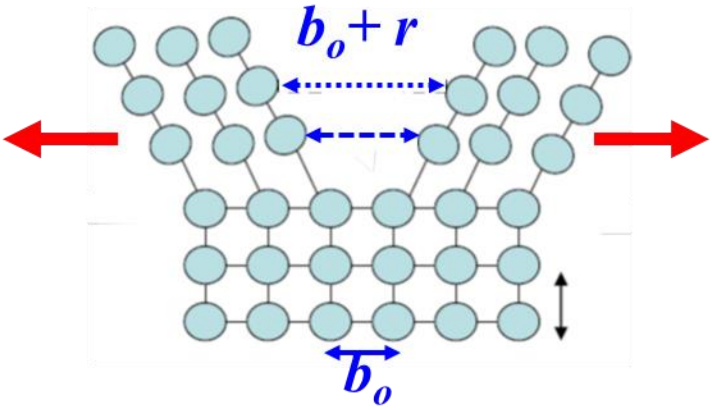

(a)

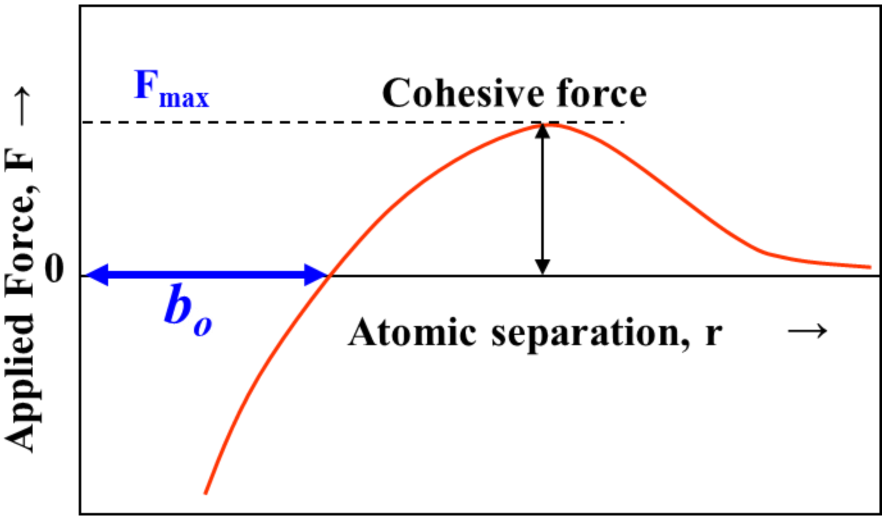

(b)

Figure 6.1: (a) Sketch of the cohesive zone in front of the tip relevant to the cohesive strength involving breaking of the bonds and (b) a sketch of the variation in the interatomic forces between two atoms as a function of separation between them, where b_o is the equilibrium interatomic distance.

This maximum cohesive force is defined as the theoretical cohesive strength of materials (σ_{th}). σ_{th} derived with theoretical models of force-displacement curves is around E/4-E/15, where E is the elastic modulus of the material. However, under practical conditions, this strength is calculated to be at least 10-1000 times lower than the theoretical value. The discrepancy is mainly attributed to the defects such as cracks, dislocations and voids which are inherently present in the materials.

Inglis [99] gave a theoretical model (local criterion), based on the stresses, for the growth of crack. He proposed that the stress felt at the crack tip is significantly higher than the stress applied to the materials. For example, for an external stress of σ_0 the stress at the tip of crack (σ_{tip}) of length *2c* and radius of curvature ρ is given as [99]:

$$\sigma_{tip} = \sigma_o \left(1 + 2\sqrt{c/\rho}\right) \qquad 6.1$$

Griffith [100] in 1920 proposed a global criterion for crack growth in terms of energetics. For a crack to propagate, the necessary global criterion (due to Griffith [100]) and the sufficient local criterion (due to Inglis [99]) have to be satisfied.

6.1 Griffith theory of brittle fracture

The first successful theoretical model explaining the discrepancy between the theoretical cohesive strength and observed fracture strength was given by Griffith [100]. He proposed that numerous fine cracks are inherently present in materials, which produce a stress concentration equivalent to the theoretical cohesive strength. A criterion for the crack propagation was established by Griffith [100]: *'A crack will propagate when the decrease in elastic strain energy is at least equal to the energy required to create the new crack surface'*. The condition for propagation of a crack was based on the competition between an excess elastic energy release *ΔG* of the solid for the movement of a crack and the surface energy of the crack C. Then, the critical equilibrium state is defined by

$$\frac{\partial(\Delta G - C)}{\partial a} \equiv G = 0 \qquad 6.2$$

The tendency of crack propagation is measured in terms of the energy release rate *G* (in units of energy per unit length) which is a function of specimen geometry and applied load. For a crack to propagate, the energy release rate must exceed a critical value G_c which is a material property, called critical energy release rate. For an ideal brittle material, crack propagates without any energy dissipation, i.e. no plastic deformation at the crack tip and hence,

$$G_c = 2\gamma_s \qquad 6.3$$

where, γ_s is the surface energy. Equation 6.3 represents the energy balance condition corresponding to the first law of thermodynamics, applied to a solid containing a crack.

6.2 Stress field near the crack tip

The propagation behavior of cracks or dislocations present in a material mainly depend on the displacements and the stress fields associated with them. A fracture is termed brittle when cracks propagate without any plastic deformation on application of load. Examples are LiF, MgO, CaF_2, BaF_2, $CaCO_3$, Zn. For such a solid, the work of fracture approaches the surface energy of the newly created surfaces. For these materials, the surface energies derived from fracture experiments agree quite well with those theoretically expected [101]. Furthermore, it provides important information for the models considering the brittle to ductile transition, which occurs in many of the technologically important structural materials, for example Fe, Al, or various intermetallic compounds.

6.3 Atomistic simulation of mode-I brittle fracture

Brittle fracture in metals is characterized by a rapid rate of crack propagation, with no gross plastic deformation and the tendency increases with decreasing temperature as well as increasing strain rate. A crucial issue in simulating actual crack propagation is that the stress field as a function of a crack distance, x, varies as $1/\sqrt{x}$, and thus involves long-range interaction. At the macroscopic level, simulation of crack propagation is described by the elasticity theory and hence making use of linear elastic solutions of the continuum theories for mechanical properties of solids. However, this approach neglects the atomistic structure and treats materials as a homogeneous, linearly elastic and isotropic medium.

The influence of atomic scale structure processes on brittle fracture can only be investigated with atomistic simulations. Molecular dynamics is one of the tools that can address the crack propagation because of its capability to address large number of atoms (of the order of 10^6). However, a major drawback is the limited availability of the interatomic potentials for a specific material. The requirement of large number of atoms impose restriction on the use of direct first-principles DFT modeling for crack propagation impossible. However, it is also understood that crack propagation under brittle fracture occurs through breaking of the interatomic bonds ahead of the crack tip (Figure 6.1). Horizontal lines represent bonds between individual atoms, and their elongation and rupture due to the opening of the crack. In the present thesis, the problem of brittle fracture is addressed using first-principles calculations of brittle cleavage decohesion, i.e. by calculating Griffith's work under mode I fracture.

6.3.1 DFT calculations of cleavage energy

The cleavage strength of Ni and its alloys is simulated by calculating the Griffith rupture work and is defined as the energy needed to cleave a crystal along a plane. Griffith work [102], within the DFT framework, is calculated using the simple model of ideal brittle cleavage decohesion between two semi-infinite planes of the crystal which are separated with a distance $b_o + x$ (Figure 6.2). Here b_o is the equilibrium interplanar separation and x is considered sufficiently large such that the interaction between the interfaces is negligible. Kumar *et.al.* [48] have shown that in the relaxed configuration up to x = 1.59 Å, the atoms between the two surfaces have appreciable interactions and hence are able to accommodate the applied separation as deformation (as strain). However, beyond a separation of 1.59 Å the interaction is extremely weak and thus the separation cannot be accommodated as elasto-plastic strain, and the configuration is similar to two fractured parts. It has also been shown by Kumar *et.al.* [48] that the change in the total energy beyond a separation of 5 Å between the interfaces is less than 0.01 eV suggesting the interactions are negligible beyond this separation. Griffith work (G_c) is

$$G_c = {}^{1}/_{A}\left[E_{tot}(x = \infty) - E_{tot}(x = 0)\right], \qquad 6.4$$

where A is the area of the cleaved surface, $E_{tot}(x=0)$ is the total energy of the system under equilibrium condition and $E_{tot}(x=\infty)$ is the total energy of the completely cleaved system.

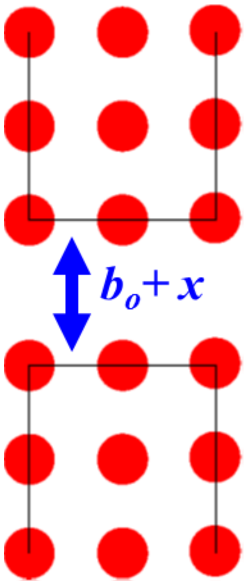

Figure 6.2: Model of the brittle cleavage with two adjacent planes separated by a distance x.

6.3.2 Computational details

To simulate substitutionally alloyed γ phase, we used a supercell containing 96 atoms by stacking six (111) layers (two successive stacking sequences ABCABC, Figure 3.1), with 16 atoms in each atomic plane. The supercell was constructed using three orthogonal vectors parallel to $[1\bar{1}0]$, $[11\bar{2}]$ and [111]. Single Ni atom on the plane to be cleaved was substituted by the alloying elements such as Ti, V, Cr and Co (3d), Zr, Nb, Mo and Ru (4d) and Hf, Ta, W, Re and Ir (5d) and was allowed to relax completely to obtain the minimum energy configuration. The relaxed configurations of each substitution was later used to evaluate the surface energy of (111). The computational details for calculating the cleavage energy for (100) have been described in details by Kumar *et al.* [48] and added as Appendix B for ready reference. In the present thesis, separation of x = 10 Å is considered between the cleaved planes.

ElaStic tool [103] has been used to calculate the full second-order elastic stiffness tensor from total energy calculated from first-principles based Quantum Espresso package [38]. Elastic stiffness constants C_{ij} of Ni-X dilute solid solutions have been calculated for supercell with 2 × 2 × 2 cubic unit cells constructed with 32 atoms (3.125 at.% of solute) along the [001] direction. By specifying the maximum strain value of η_{max}, 31 distorted structures between strain values of $-\eta_{max}$ and η_{max} have been created and the energies are obtained by performing first-principles calculations. A polynomial fit is done to calculate the second derivative at equilibrium of the energy with respect to the strain. With these values, Voigt [104] approach assuming uniform strain and Reuss [105] approach assuming uniform stress are used for determining the bulk (B), shear (G) and Young modulus (E) of the material. Hill [106, 107] has shown that the Voigt and Reuss elastic moduli are the strict upper and lower bound respectively. Using Voigt's approximation [103] bulk and shear moduli are obtained by averaging first-principles elastic stiffness constants (C_{ij}) as

$$B_V = {[(c_{11} + c_{22} + c_{33}) + 2(c_{12} + c_{13} + c_{23})]}\Big/_{9}, \qquad 6.5$$

$$G_V = {\begin{bmatrix} (c_{11} + c_{22} + c_{33}) - (c_{12} + c_{13} + c_{23}) + \\ 3(c_{44} + c_{55} + c_{66}) \end{bmatrix}}\Big/_{15}, \qquad 6.6$$

Similarly, with Reuss procedure [103] with single-crystal elastic constants, the related elastic properties of a polycrystalline alloy are as follows

$$B_R = [(s_{11} + s_{22} + s_{33}) + 2(s_{12} + s_{13} + s_{23})]^{-1}, \qquad 6.7$$

$$G_R = 15\begin{bmatrix} 4(s_{11} + s_{22} + s_{33}) - (s_{12} + s_{13} + s_{23}) \\ +3(s_{44} + s_{55} + s_{66}) \end{bmatrix}^{-1}, \qquad 6.8$$

S_{ij} are the compliance tensor coefficients. The Young's modulus from bulk and shear moduli is calculated as

$$E = {}^{9BG}\!/_{(3B + G)}, \qquad 6.9$$

6.3.3 *Benchmarking*

Our estimate for G_c in magnetic and non-magnetic states of Ni for the (111) surface are 3.62 J/m^2 and 3.78 J/m^2 respectively. Unlike the γ_{us} and γ_{is}, the G_c of ferromagnetic Ni is 4 % lower as compared to that of non-magnetic Ni. Similarly, the cleavage strength for the (100) surface is also found to be lower for ferromagnetic Ni (4.18 J/m^2) compared to the non-magnetic case (4.29 J/m^2) [48]. G_c for Ni ((111) plane) using the EAM potential by Mishin [64] was estimated to be 3.518 J/m^2. In another work using VASP with GGA *pseudopotentials*, Siegel [61] has estimated it to be 3.895 J/m^2, respectively. Hence, our estimated values for the pure system are in reasonable agreement with the reported values.

6.4 Effect of alloying elements on cleavage energy in γ

In this thesis, cleavage energy has been estimated with single Ni atom substituted with solute atoms from 3d, 4d and 5d series of transition metals. The variations with d-orbital valence electrons are shown in Figure 6.3a and 6.3b, respectively for the non-magnetic and the magnetic states. All the elements except Zr and Pd tend to increase the cleavage energy of Ni, irrespective of its magnetic state. In the magnetic case, systems doped with Nb and W have cleavage energies of 3.67 and 3.74 J/m^2 respectively, while in another work using VASP with GGA *pseudopotentials*, Siegel [61] has estimated these values to be 3.895 and 3.906 J/m^2, respectively. Thus the trends in variation in G_c obtained here are in good agreement with those reported in the literature. In both the studies with Nb substitution, the magnitude of G_c is relatively unchanged with respect to the pure system while W substitution enhances it.

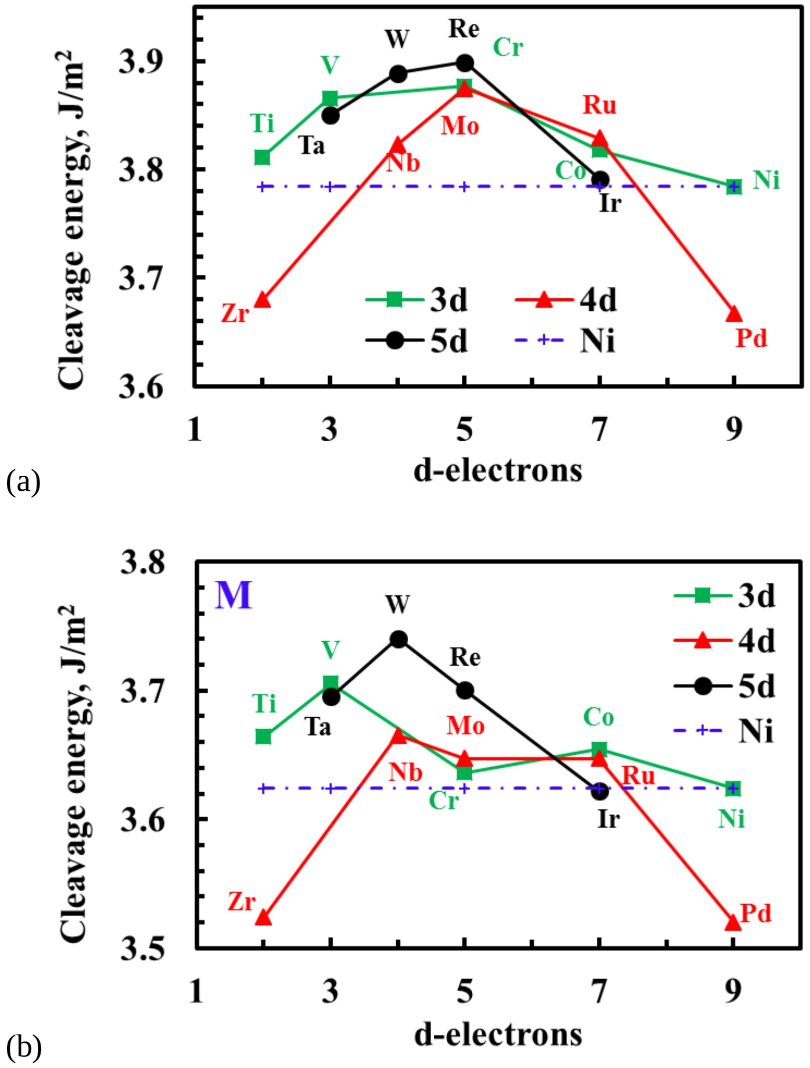

Figure 6.3: Change in the cleavage energy (G_c) of Ni with solute substitution as a function of their valency in (a) non-magnetic and (b) magnetic state. Dotted lines represents G_c of pure Ni. Copyright (2018) by Comp. Mat. Sci [39].

In non-magnetic state of Ni, the trend in variation of the G_c is similar to that of the γ_{us} i.e., it increases with the number of d-valence electrons of the solute with maxima occurring for solutes with d-valence of 5 (Cr, Mo and Re respectively of 3d, 4d and 5d series). This indicates that there is correlation between the γ_{us} and the G_c. This is interesting because the γ_{us} is related to the dislocation nucleation whereas G_c is related to the complete breaking of bonds. There is, however, no such clear correlation in estimates of γ_{us} and G_c obtained for magnetic state of Ni. The reasons for the presence and absence of the correlations will be investigated in future.

6.5 Ductility parameter using Griffith criteria

One of the ways of quantifying ductility of materials is through a parameter known as ductility parameter, D = $0.15G_c/\gamma_{us}$ [61, 97]. The influence of alloying elements on the ductility parameter estimated from the current study is listed in Table 6.1. It is clear that Al, V, Cr, Co, Mo, Ru, W, Re and Ir reduce D for the non-magnetic Ni. However, when Ni is in the magnetic state, all the solutes excepting Co and Ir enhance the ductility parameter. Nevertheless, the alloying elements considered here only weakly influence the ductility of Ni.

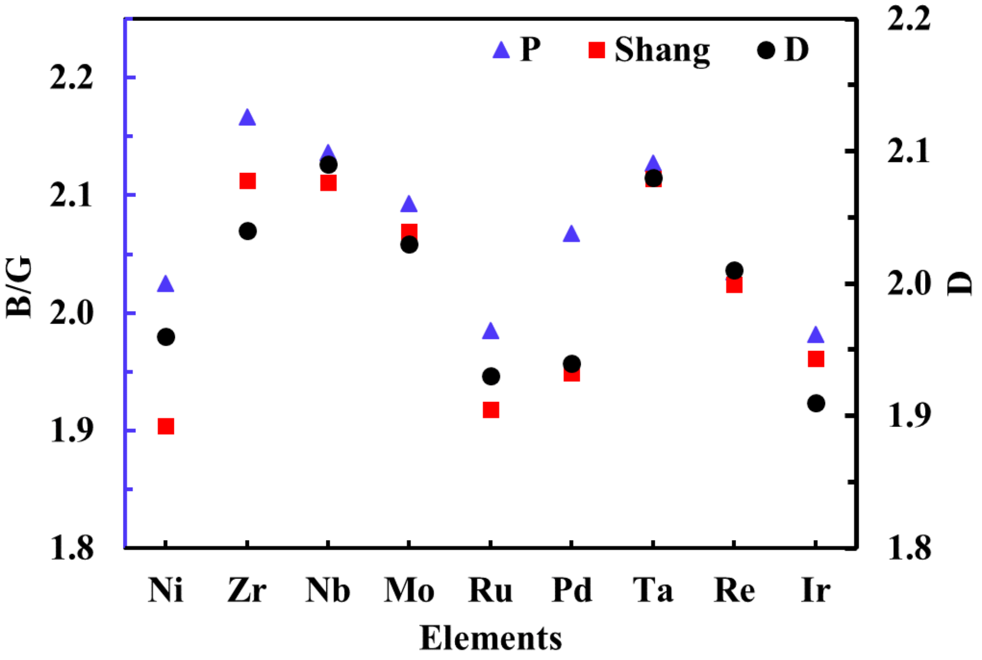

Figure 6.4: Comparison of the ductility parameters estimated from the Rice (D) and Pugh criterion (P) and comparison of P with Shang *et.al.* [112].

Table 6.1: Ductility parameter for substitution of different solutes for Ni in non-magnetic and ferromagnetic state.

	Al	Ti	V	Cr	Co	**Ni**	Zr	Nb	Mo	Ru	Pd	Ta	W	Re	Ir
D (NM)	2.33	2.41	2.36	2.27	2.38	**2.40**	2.44	2.44	2.36	2.36	2.40	2.43	2.37	2.30	2.33
D (M)	1.96	2.03	2.01	1.93	1.92	**1.93**	2.04	2.09	2.03	1.93	1.94	2.08	2.06	2.01	1.91

6.6 Ductility parameter using Pugh criteria

Elastic moduli of materials can be used to assess mechanical properties such as strength and ductility/brittleness. The shear modulus (*G*) of the material is linked to the resistance of the material to plastic deformation and the bulk modulus (*B*) represents the average resistance to bond breaking [110]. Also for FCC materials Gilman [111] showed that the yield stress is proportional to the Young’s modulus (*E*). Based on the B/G ratio, Pugh [110] proposed that materials with large B/G ratios (>1.75) behave in a ductile manner while low *B/G* ratios (<1.75) in a brittle manner. Hence, the effects of solutes on the elastic constants using computational tool will provide an understanding and will be helpful in identifying suitable alloying elements for the application. ElaStic tool [103] have been used in the present study to calculate the elastic stiffness constants C_{ij} of Ni-X dilute solid solutions.

The values of elastic constants for cubic system (C_{11}, C_{12} and C_{44}) and the bulk, shear and the Young moduli for bulk Ni and for solid solution (specific composition of 3.125 at.% of solute) are listed in Table 6.2. The *B*, *G* and Young’s modulus are obtained using the Voigt and Reuss approximations. For bulk Ni the values of elastic constants are in good agreement with the reported experimental values by Neighbours *et. al.* [108] and from first-principles by Kim *et. al.* [109]. All solute substitution increases the moduli of the system with maximum value for Ru and Ir from 4d and 5d series transition metals.

The value of ductility parameter (B/G) by Pugh [110] for Ni is calculated to be 2.03 which is higher than 1.75 and hence is in accordance with its higher ductility. B/G ratios estimated in the present study are in very good agreement with those of Shang et.al [112] (Figure 6.4). Similar to Rice criteria, shown earlier, all solute substitution increases the ductility of the solid solution. However, a one-to-one correlation between the numbers obtained using the two criteria is not expected as B/G is dependent on the elastic response of the material, whereas D (from Rice's criteria) is dependent on energies of fracture/surface (γ) and that of plastic deformation (γ_{us}).

Table 6.2: Calculated elastic properties, unit of GPa, for dilute solid solution of Ni (3.125 at. % of solute). P stands for present study and numbers in the parenthesis refers to the reference number in the bibiliography.

					Bulk modulus (B)		Shear modulus (G)		Young modulus		B/G
		C_{11}	C_{12}	C_{44}	Voigt	Reuss	Voigt	Reuss	Voigt	Reuss	Voigt
Ni	P	249	155	122	186	186	92	74	237	197	2.03
	[108]	253	152	124							
	[109]	281	157	131	198		104		265		1.90
Zr	P	265	170	123	201	201	93	75	242	201	2.17
	[109]	261	158	117	192		91		235		2.11
Nb	P	262	168	124	199	199	93	75	242	199	2.14
	[109]	268	162	120	197		93		242		2.12
Mo	P	256	167	127	197	197	94	73	243	194	2.09
	[109]	278	163	124	202		98		252		2.06
Ru	P	272	168	135	202	202	102	83	262	219	1.99
	[112]	280	157	131	198		103				1.92
Pd	P	267	164	126	199	199	96	80	248	211	2.07
	[112]	269	154	126	192		99				1.95
Ta	P	264	169	126	201	201	94	76	245	202	2.13
	[109]	270	163	121	199		94		243		2.12
Re	P	269	170	133	203	203	100	79	257	211	2.04
	[109]	281	162	126	199		99		256		2.01
Ir	P	277	168	136	204	204	103	85	265	224	1.98
	[112]	278	160	130	199		102				1.96

6.7 Summary

We have calculated the Griffith's work of rupture (cleavage energy) and elastic constants for solid solution of Ni with specific composition of ~1 and 3.125 at.% of solute. All solutes, except Zr and Ir, increases the cleavage energy of the system with maxima for half-filled or nearly half-filled (4 electrons) d-orbitals. Similarly, all solutes increase the elastic constants of the system with maximum increase for Ru and Ir from 4d and 5d-series of transition metals. A uniform increase of 6-8% for C_{11}, C_{12}, bulk modulus is observed. However, except for Ru, Re and Ir substitution there is nominal improvement in the C_{44} and Young's modulus. For magnetic state of Ni all solutes, except Ru and Ir, increase the ductility of the system based on the calculation of ductility parameter form Rice approach ($D = 0.15G_c/\gamma_{us}$) as well as Pugh approach (B/G).

Chapter 7

Summary

This thesis is an exploratory study of delving the role of alloying elements on various properties of γ and γ' phases of Ni-based superalloys. First-principles based density functional theory calculations have been performed using the computational tool, Quantum Espresso, to examine the effects of transition metals (TM) from 3d, 4d and 5d series on the lattice parameter, cleavage energy, binding energy and planar fault energies of the phases. As Ni undergoes a magnetic transition, calculations have been performed considering both non-magnetic (non-spin polarized) and ferromagnetic (spin polarized) states. Highlights of the important findings of this research are presented below:

Influence of alloying elements on the lattice parameter of Ni

- The equilibrium lattice parameters (a_o) of non-magnetic Ni and its solid solutions are lower than those of the ferromagnetic counterparts.
- From the linear variation of a_o with the percentage of solute substitution, Vegard's coefficients have been estimated and compared with those available in the literature.
- Barring Cr and Co, all other alloying element substitutions result in expanding the lattice parameter of Ni. Substitution by Zr leads to maximum expansion of the lattice with a Vegard's coefficient of around 0.9.

Energetics of substitutional alloying elements and their tendency to clustering in Ni-based solid solution

- Using the concept of binding energy between the solute atoms, it is seen that Co has the tendency to form clusters in Ni-based solid solution whereas other alloying atoms prefer to stay apart. In the ferromagnetic state, elements such as Ti, V, Mo, Pd, Nb, Ta, W and Re show preference to stay as second nearest neighbour, thus indicating the possibility of ordering.

Variation of generalized stacking fault energies of Ni with dilute alloying

- The influence of solutes on the intrinsic stacking fault energy (ISFE), an important parameter that affects cross-slip of dislocations formed due to the dissociation of perfect dislocation in the γ matrix phase has been investigated. The fault was created on the (111) plane by a displacement of $^1/_6\,[\bar{2}11]$ with the solute present on the fault plane, and the penalty in the planar energy density for incorporating the fault has been evaluated as ISFE.
- The ISFE of pure Ni is 24% higher in the ferromagnetic state compared to the magnetic state. When alloyed with solutes, except Pd, all the elements considered in the study reduce the ISFE of the system, with maximum reduction of about 15% when substituted by either of Nb, Mo, Ru, W or Re.
- Increasing the substitutional element concentration to two percent results in further reduction of ISFE.
- For the first time, the dependence of spacing between the solute atoms on the ISFE is being reported. While for most of the solutes this variation is very small, Cr shows an unusual behavior. When the substituted Cr atoms are first nearest neighbour on the fault plane, the ISFE decreases compared to a system substituted with single Cr atom. However, the fault energy increases when the Cr atoms remain far apart as third or fourth nearest neighbour.

- The barrier for the nucleation of dislocation can be estimated in terms of unstable stacking fault energy (USFE). Ferromagnetic Ni has 19% higher USFE compared to the "non-magnetic" one.
- There is marginal increase in USFE with the substitution of Cr, Co, Ir and Ru in the ferromagnetic system. However, in the non-magnetic system except Zr, Nb and Pd all other substitutions increase this energy with maximal increase for those TMs with half-filled d-orbitals (i.e. Cr, Mo and Re of 3d, 4d and 5d series transition metals respectively).
- For the first time, the dependence of spacing between the solutes on the USFE has been estimated. While Mo and Cr substitutions show some unusual behavior, the case of Cr is more interesting wherein in the USFE can be tuned to be either below or above that of pure (ferromagnetic) Ni just by changing the spacing between the Cr atoms.

Variation of planar fault energies of Ni_3Al with alloying

- With Ni_3Al as the basis for γ' phase, the energies due to antiphase boundary (APBE), superlattice intrinsic stacking fault (SISFE) and unstable stacking fault (USFE) have been systematically calculated for substitution with various alloying elements.
- It is inferred that solute substitutions at Al site could provide better strengthening as reflected by the higher values of USFE and APBE compared to pure Ni_3Al.
- APBE is significantly increased for solutes with 5 electrons or less in their d-orbitals with higher values for transition metals belonging to 4d and 5d series.
- The USFE of γ' phase increases with number of d-orbital electrons of the solute with maximal values for elements having half-filled d-orbitals, viz., Cr, Mn ($3d^5$), Mo ($4d^5$) and Re ($5d^5$), and reduces considerably thereafter.
- An important observation is that excess Ni present as anti-site on the fault plane tends to reduce the values of APBE, SISFE and USFE by 41, 40 and 3%, respectively, whereas excess Al as anti-site increases the respective energies by 43, 152 and 22%.

Influence of solutes on the ductility of Ni-based solid solution

- Cleavage strength of (100) plane for bulk Ni was estimated by calculating the G_c. and its values in ferromagnetic and non-magnetic states, respectively, are estimated to be 4.18 mJ/m^2 and 4.29 mJ/m^2.
- The ratio of Griffith work for formation of surfaces to that of USFE is an indicator of the ductility of a system. Based on the criterion given by Rice, it is found that solute substitutions lead to marginal improvement, with respect to pure Ni, in ductility of ferromagnetic Ni, except in the case Ir, where a marginal decrease is observed.
- In the case of non-magnetic system, except Ti, Zr, Nb and Pd, other solute substitutions lead to a decrease in the ductility parameter.
- Ductility parameter (B/G) higher than 1.75 based on Pugh for Ni is in accordance with its higher ductility. Based on Pugh criterion all solute substitution suggest further increases in the ductility of the alloy.

Thus, in this thesis, properties relevant to the design of Ni-based superalloys have been systematically estimated. The reasons for variation of many of the properties have been addressed from the point of view of atomic interaction along with their electronic structures. It is envisaged that the trends and estimated properties would be useful in the context of Integrated Computational Materials Engineering (ICME) framework for the rational design of superalloys with specific quantified properties.

References

1. R.C. Reed, The Superalloys: Fundamentals and Applications, Cambridge University Press, New York, 372 (2006).
2. C.T. Sims, N.S. Stoloff, W.C. Hagel, Superalloys II. High temperature Materials for Aerospace and Industrial Power, A Wiley-Interscience Publication John Wiley and Sons, New York, (1987).
3. K. Muraleedharan, R. Balamuralikrishnan, N. Das, J Mater. Sci. **44** 2218 (2009).
4. E. Nembach and G. Neite, Prog. Mater. Sci. **29 (3)** 177 (1985).
5. R.E. Voskoboinikov, Phys. Met. Metallogr. 114 (7) 545 (2013).
6. W. Zhao, Z. Sun, S. Gong, Acta Mater. **135** 25 (2017).
7. D. Raabe, The simulation of materials microstructures and properties, Wiley-VCH (1998).
8. M.J. Cawkwell, D. Nguyen-Manh, C. Woodward, D.G. Pettifor, V. Vitek, Science, **309** 1059 (2005).
9. P. Hohenberg and W. Kohn, Phys. Rev. B **136** 864B (1964).
10. W. Kohn and L. Sham, Phys. Rev. B **140** 1133 (1965).
11. A.J. Freeman and E. Wimmer, Annu. Rev. Mater. Sci. **25** 7 (1995).
12. I. Shin and E. A. Carter, Acta Mater. **64** 198 (2014).
13. J.B. Piochaud, T.P.C. Klaver, G. Adjanor, P. Olsson, C. Domain, C.S. Becquart, Physical Review B **89** 024101 (2014).
14. S.L. Shang, W.Y. Wang, B.C. Zhou, Y. Wang, K.A. Darling, L.J. Kecskes, S.N. Mathaudhu, Z.K. Liu, Acta Mater. **67** 168 (2014).

15. G.I. Barenblatt, The mathematical theory of equilibrium cracks in brittle fracture. Advances in Applied Mechanics 7 **55** (1962).
16. Z.H. Jin, C.T. Sun, International Journal of Solids and Structures **43** 1047 (2006).
17. G. Schock, Mat. Sci. Eng. A **400** 7 (2005).
18. J.R. Rice and G. E. Beltz, J. Mech. Phys. Solids **42** 333 (1994).
19. G.E. Beltz and J.R. Rice, Acta metall. mater. **40** S321 (1992).
20. V. Paidar and V. Vitek, Intermetallic Compounds – Principles and Practice, **3** (2002).
21. A.E. Smith, Materials Forum **31** (2007).
22. Y. Juan and E. Kaxiras, Phil. Mag. A **7**, 1367 (1996).
23. A. Datta, U.V. Waghmare, U. Ramamurty, Scripta Mater. **60** 124 (2009).
24. V. Vitek, Phil. Mag. **18** 773 (1968).
25. R.M. Martin, Electronic Structure, Cambridge University Press.
26. J.P. Perdew, J.A. Chevary, S.H. Vosko, K.A. Jackson, M.R. Pederson, D.J. Singh, C. Fiolhais, Phys. Rev. B **46**, 6671 (1992); **48**, 4978(E) (1993).
27. A.D. Becke, J. Chem. Phys. **96**, 2155 (1992).
28. E.I. Proynov, E. Ruiz, A. Vela, D.R. Salahub, Int. J. Quantum Chem. **S29**, 61 (1995).
29. D.R. Hamann, Phys. Rev. Lett. **76**, 660 (1996).
30. P.H.T. Philipsen, G. te Velde, E.J. Baerends, Chem. Phys. Lett. **226**, 583 (1994).
31. B. Hammer, K.W. Jacobsen, J.K. N∅rskov, Phys. Rev. Lett. **70** 3971 (1993).
32. J.P. Perdew, K. Burke, M. Ernzerhof, Phys. Rev. Lett. **77** 3865 (1996).
33. J.C. Phillips, Phys. Rev. **112 (3)** 685 (1958).
34. J.C. Phillips and L. Kleinman, Phys. Rev. **116 (2)** 287 (1959).
35. D.R, Hamann, M. Schlüter, C. Chang, Phys. Rev. Lett. **43** 1494 (1979).

36. S. Goedecker and K. Maschke, Phys. Rev. A **45** 88 (1992).
37. D. Vanderbilt, Phys. Rev. B. **41** 7892 (1990).
38. P. Giannozzi *et al.*, J. Phys.: Condens. Matter **21** 395502 (2009); URL http://www.quantum-espresso.org.
39. K. Kumar, R. Sankarasubramanian, U. V. Waghmare, Comput. Mater. Sci. **150** 424 (2018).
40. F.R.N. Nabarro, F. Villiers, The physics of creep. London: Taylor & Francis (1995).
41. C. Wolverton, Acta Mater. **55** (17) 5876 (2007).
42. L. Vegard, Z. Phys. **5** 17 (1921).
43. A.R. Denton, N.W. Ashcroft, Phys. Rev. A **43** No. 6 (1991).
44. Y. Mishima, S. Ochiai, T. Suzuki, Acta Metall. **33** 1161 (1985).
45. P. Caron, Superalloys 2000, ed. T. M. Pollock *et al.*, TMS 2000, pp. 737-746.
46. W. Pearson, A Handbook of Lattice Spacings and Structures of Metals and Alloys, Vol. **2** 1135 (Oxford, UK: Pergamon Press, 1967).
47. K.N. Goswami, ME Thesis, IISc Bangalore (2012).
48. K. Kumar, R. Sankarasubramanian, U.V. Waghmare, Comput. Mater. Sci. **97** 26 (2015).
49. A. Mottura, M.W. Finnis, R.C. Reed, Acta Mater. **60** 2866 (2012).
50. R. Peierls, Proc. Phys. Soc. **52** 34 (1940).
51. F.R.N. Nabarro, Proc. Phys. Soc. **59** 256 (1947).
52. G. Leibfried and K. Lücke, Z. Phys. **126** 450 (1949).
53. A.J. Foreman, M.A. Jawson, and J.K. Wood, Proc. Phys. Soc. **64** 156 (1951).
54. D. Hull and D.J. Bacon, Introduction to Dislocation, 5th Ed. Elsevier (2011).
55. X.X. Yu and C.Y. Wang, Mater. Sci. Eng. A **539** 38 (2012).
56. B. Burton, Acta Metall. **30** 905 (1982).
57. F.A. Mohamed and T.G. Langdon, Acta Metall. **22** 779 (1974).
58. X.S. Xie, G.L. Chen, P.J. McHugh, J.K Tien, Scr. Metall. **16** 483 (1982).

59. H. Rehman, K. Durst, S. Neumeier, A. Sato, R. Reed, M. Goken, Acta Mater. **137** 54 (2017).
60. R.P. Reed and R.E. Schramm, J, Appl. Phys., **45(11)** 4705 (1974).
61. D.J. Siegela, Appl. Phys. Lett. **87** 121901 (2005).
62. A. Datta, A. Srirangarajan, U.V. Waghmare, U. Ramamurty, A.C. To, Comput. Mater. Sci. **50** 3342 (2011).
63. S.L. Shang, C.L. Zacher, H.Z. Wang, Y. Du, Z.K. Liu, J. Phys. Condens. Matter **24** 505403 (2012).
64. Y. Mishin, Acta Mater. **52** 1451 (2004).
65. L.E. Murr, Interfacial phenomena in metals and alloys. Reading, MA: Addison-Wesley; (1975).
66. R.C. Reed, T. Tao, N. Warnken, Acta Mater. **57** 5898 (2009).
67. J. Mittra, U. V. Waghmare, A. Arya, G.K. Dey, Comput. Mater. Sci. **81** 249 (2014).
68. S. Zhao, G. Malcolm Stocks, Y. Zhang, Acta Matall. **134** 334 (2017).
69. X.X. Yu and C.Y. Wang, Acta Mater. **57** 5914 (2009).
70. T.L. Achmad, W. Fu, H. Chen, C. Zhang, Z. Yang, Comput. Mat. Sci. **143** 112 (2018).
71. C.B. Carter and S.M. Holmes, Phil Mag **35** 1161 (1977).
72. P. C. J. Gallagher, Metallurgical Transactions, **1** 2429 (1970).
73. K. Kumar, R. Sankarasubramanian, U.V. Waghmare, Scripta Mater. **142** 74 (2018).
74. V. Paidar and D.P. Pope, V. Vitek, Acta Metall. **32** 435 (1984).
75. Y. Umakoshi, D.P Pope, V. Vitek, Acta Metall. **32** 449 (1984).
76. S. Huang, W. Li, S. Lu, F. Tian, J. Shen, E. Holmstrom, L. Vitos, Scripta Mater. **108** 44 (2015).
77. P. Geng, W. Li, X. Zhang, Y. Deng, H. Kou, J. Ma, J. Shao, L. Chen, X. Wu, J. of Alloys and Compounds **706** 340 (2017).
78. Q. Wu and S. Li, Comput. Mater. Sci. **53** 436 (2012).
79. H. Xie, T. Yu, C. Tang, Modelling Simul. Mater. Sci. Eng. 21 055008 (2013).

80. A. Breidi, J. Allen, A. Mottura, Acta Mater. **145** 97 (2018).
81. M. Chandran, S.K. Sondhi, Modelling Simul. Mater. Sci. Eng. **19** 025008 (2011).
82. Y. Rao, T.M. Smith, M.J. Mills, M. Ghazisaeidi, Acta Mater. **148** 173 (2018).
83. K.V. Vamsi and S. Karthikeyan, Superalloys 2012: 12th International Symposium on Superalloys, Ed. E.S. Huron, R.C. Reed, M.C. Hardy, M.J. Mills, R.E. Montero, P.D. Portella and J. Telesman, TMS (The Minerals, Metals & Materials Society) 521 (2012).
84. A. Paxton, Y.G. Sun, Philos. Mag. A **78** 85 (1998).
85. O.N. Mryasov, Y.N. Gornostyrev, M. van Schilfgaarde, A.J. Freeman, Acta Mater. **50** 4545 (2002).
86. K. Hemker, M.J. Mills, Philos. Mag. A **68** 305 (1993).
87. H.P. Karnthaler, E.T. Muhlbacher, C. Rentenberger, Acta Mater. **44** 547 (1996).
88. T. Kruml, E. Conforto, B. Lo Piccolo, D. Caillard, J.L. Martin, Acta Mater. **50** 5091 (2002).
89. D.M. Knowles and Q.Z. Chen, Mat. Sci. Eng. A **340 (1)** 88 (2003).
90. T. Wang, L. Chen, Z. Liu, Mater. Sci. Eng. A **431** 196 (2006).
91. C. Woodward, A. van de Walle, M. Asta, D.R. Trinkle, Acta Mater. **75** 60 (2014).
92. M.H. Yoo, Acta Metall. **35** 1559 (1987).
93. N.C. Eurich, P.D. Bristowe, Scripta Mater. **102** 87 (2015).
94. D.M. Dimiduk, A.W. Thompson, J.C. Williams, Philos. Mag A **67(3)** 675 (1993).
95. O.I. Gorbatov et al., Phys. Rev. B **93** 224106 (2016).
96. N Baluc and R. Schaublin, Phil. Mag. A **74** 113 (1996).
97. J.R. Rice, J. Mech. Phys. Solids **40** 239 (1992).
98. D.M. Shah, D.N. Duhl, Ed. N.S. Stoloff, C.C. Koch, C.T. Liu, O. Izumi, MRS Symposium Proceedings, **81** 411 (1987).
99. C.E. Inglis. Trans. Inst. Naval Architects, **55** 219 (1913).

100. A.A. Griffith, Philos. Trans. R. Soc. London, **221A** 163 (1920).

101. J.J. Gilman. J. appl. Phys. **44** 2208 (1961).

102. X. Gong, G.X. Yang, Y.H. Fu, Y.Q. Xie, J. Zhuang, X. Ning, Comput. Mater. Sci. **47** 320 (2009).

103. R. Golesorkhtabar *et al.* / Computer Physics Communications **184** 1861 (2013).

104. W. Voigt, L. Kristallphysik, B.G. Teubner, Leipzig (1928).

105. A. Reuss, Z. Angew, Math. Mech. **9** 49 (1929).

106. R. Hill, Proc. Phys. Soc. A **65** 349 (1952).

107. R. Hill, J. Mech. Phys. Solids **11** 357 (1963).

108. J.R. Neighbours, F.W. Bratten, Charles S. Smith, J. of Applied Phys. **23** 389 (1952).

109. D.E. Kim, Shun-Li Shang, Zi-Kui Liu, Comput. Mater. Sci. **47** 254 (2009).

110. S.F. Pugh, Philos. Mag. **45** 823 (1954).

111. J.J. Gilman, Aust. J. Phys. **13** 327 (1960).

112. S.L. Shang, D. E. Kim, C.L. Zacherl, Y. Wang, Y. Du, Z.K. Liu, J. Appl. Phys. **112** 053515 (2012).

Appendix A

Precise determination of displacement for the creation of unstable stacking fault (USF) in Ni

96 Ni atoms supercell was constructed with three orthogonal directions along $[\bar{1}01]$, $[\bar{1}2\bar{1}]$ and [111] direction having six (111) layers. The faults were simulated by shear deformation along <112>{111} through displacing the image of the supercell by $x\overrightarrow{b_p}$, along the $[\bar{2}11]$ direction, and allowing the positions of the atoms in the outer planes to relax only along directions perpendicular to the fault plane. Here $\overrightarrow{b_p}$ corresponds to the Burgers vector $1/_6\,[\bar{2}11]$ and x was varied from 0.06 to 1.29 in increments of Δx=0.12. The corresponding energy penalty γ_{fs} is estimated as

$$\gamma_{fs} = \frac{E_f - E_o}{A},$$

where E_f and E_o are the energies of the faulted and perfect structures, and A is the area of the slip plane in the supercell on which fault has been generated. As a result, a rough estimate of generalized stacking fault energy curve was obtained (Figure A.1). For a more precise determination of the displacement corresponding to USF, a finer step of Δx=0.025 was used in the range between x=0.48 and 0.60. This led to the conclusion that USF can be created by a displacement vector of $0.56 \times 1/_6\,[\bar{2}11]$ on the (111) plane.

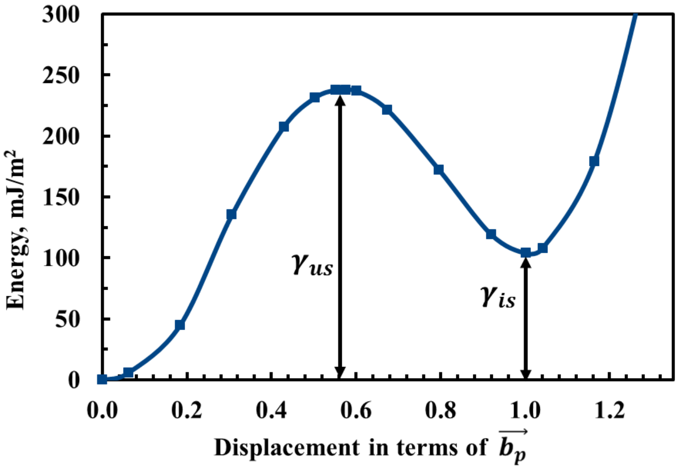

Figure A.1: Energy profile of sliding one half of the Ni supercell against another along $[\bar{2}11]$ on (111) for various displacements. The line joining the points is a guide to the eye.

Appendix B

Calculation of cleavage energy

The (001) planar interface of the composite γ/γ′ system is considered for the calculation of cleavage energy. A γ-γ′system is simulated using a supercell of 1×1×10 cubic unit cells (40 atoms corresponding to 20 layers with 2 atoms per layer) constructed along the [001] direction (Figure B.1). γ/γ′ interface is considered as (002)γ||(001)γ′ plane based on the fact that the {002} interface plane is coherent between the γ-Ni and γ′-Ni_3Al blocks [B.1]. The supercell is divided by the interface with one half consisting of consecutive layers of Ni atoms (corresponding to γ phase) and the other half with alternating layers of pure Ni and a mix of 50 % Ni + 50 % Al (corresponding to γ′- Ni_3Al phase) (Figure B.1).

The Griffith work of rupture (G_c) is used to determine the tensile cleavage strength of the bulk γ-γ′system and is defined as the energy needed to cleave a crystal about a plane [B.2]. Using DFT, G_c has been calculated using a simple model of ideal brittle cleavage between two planes of the crystal which are separated by a distance $x_d+ x$, where x_d is the equilibrium interplanar separation. To simulate a cleaved crystal, this separation should be sufficiently large such that the interaction between the interfaces vanishes (Figure B.2 (a)). The total energy of the system ($E_{tot}(x)$), with increasing separation x, is obtained by completely relaxing the system (Figure B.2 (b)). Infinite separation may be referred to as a separation x_m beyond which the increase in the total energy ($\Delta E = E_{tot}(x) - E_{tot}(x_m)$) of the system is below a small insignificant value (in the present case ΔE per atom has been taken to be 10^{-3} eV). From Figure B.2 (b) it can be observed that the change in total system energy beyond a separation of 5 Å is less than 0.001 eV suggesting that the interactions across the cleaved interface are too small beyond this separation. Thus, in the present study, x_m is taken to be equal to 10 Å.

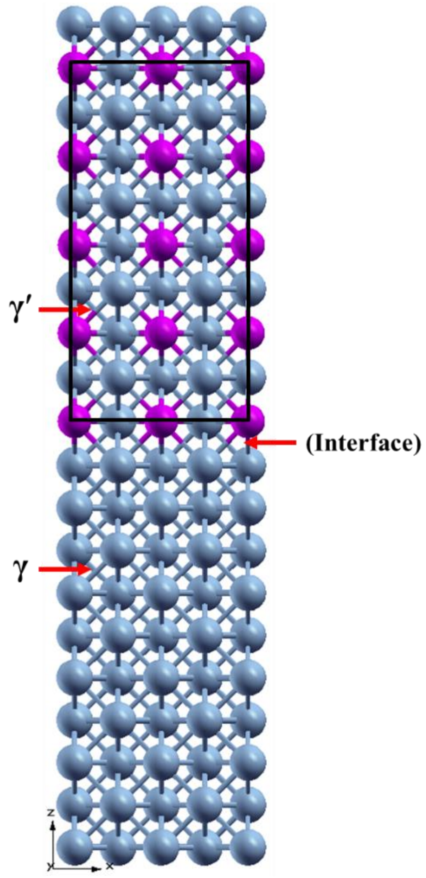

Figure B.1: **20 layers γ - γ′ supercell used for cleavage and GSF energy calculation.**

The cleavage energy, G_c is calculated using

$$G_c = {}^{1}\!/_{A}\,[E_{tot}(x_m) - E_{tot}(0)]$$

where, A is the area of the cleaved surface, $E_{tot}(0)$ and $E_{tot}(x_m)$ are, respectively, the total energy of the bulk and cleaved systems.

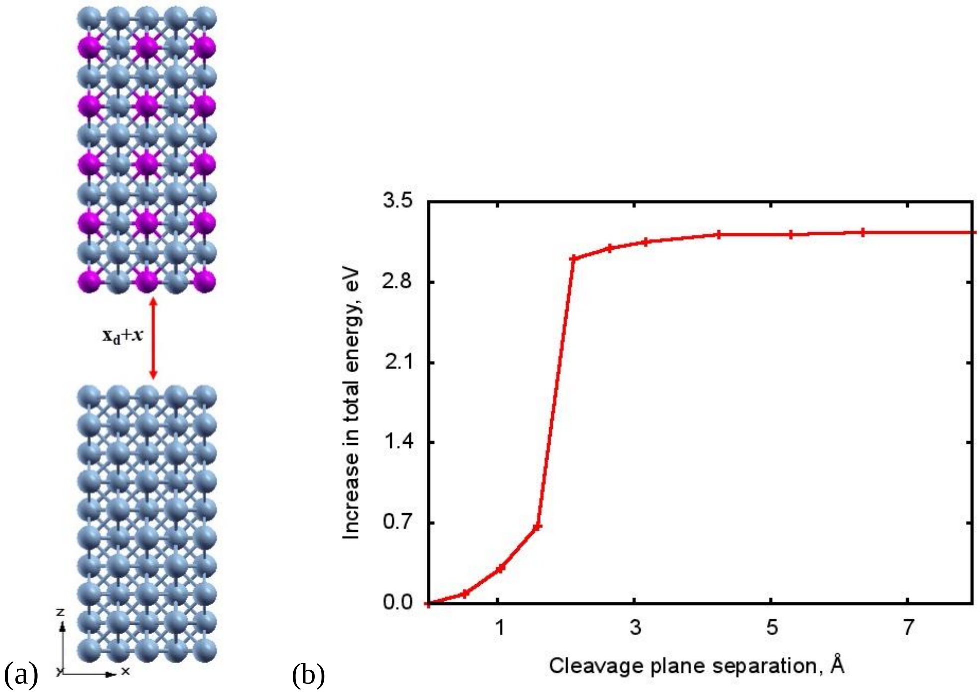

Figure B.2. (a) Brittle cleavage model with two adjacent planes separated by a distance $x_d + x$ and (b) increase in the total energy for the 20 layer γ-γ′ system as a function of $x_d + x$.

References:

B.1 R.C. Reed, The Superalloys: Fundamentals and Applications, Cambridge University Press, New York, 2006, 372.

B.2 X.-F. Gong, G.X. Yang, Y.H. Fu, Y.Q. Xie, J. Zhuang, X.-J. Ning, Comput. Mater. Sci. 2009, 47, 320-325.